Electrocatalytic and Photoelectrosynthetic Hydrogen Production using Metalloporphyrins and Molecular-modified Gallium Phosphide Photocathodes

by

Diana Khusnutdinova

A Dissertation Presented in Partial Fulfillment
of the Requirements for the Degree
Doctor of Philosophy

Approved March 2019 by the
Graduate Supervisory Committee:

Gary F. Moore, Chair
Ana L. Moore
William T. Petuskey

ARIZONA STATE UNIVERSITY

May 2019

ABSTRACT

Metalloporphyrins represent a class of molecular electrocatalysts for driving energy relevant half-reactions, including hydrogen evolution and carbon dioxide reduction. As electrocatalysts, they provide a strategy, and potential structural component, for linking renewable energy sources with the production of fuels and other value-added chemicals. In this work, porphyrins are used as structural motifs for exploring structure-function relationships in electrocatalysis and as molecular building blocks for assembling photoelectrochemical assemblies leveraging the light capture and conversion properties of a gallium phosphide (GaP) semiconductor. These concepts are further covered in Chapter 1. A direct one-step method to chemically graft metalloporphyrins to GaP surfaces is described in Chapter 2. Structural characterization of the hybrid assemblies is achieved using surface-sensitive spectroscopic methods, and functional performance for photoinduced hydrogen production is demonstrated via three-electrode electrochemical measurement combined with product analysis using gas chromatography. In Chapter 3, preparation of a novel cobalt porphyrin modified with 3-fluorophenyl groups at all four *meso*-positions of the porphyrin ring and a single 4-vinylphenyl surface attachment group at one of the β-positions is described. Electrochemical measurements show the 3-fluorophenyl groups perturb the reduction potentials of the complex to more positive values as compared to non-fluorinated analogs, illustrating synthetic control over the redox properties of the catalysts. The use of grazing angle attenuated total reflectance Fourier transform infrared spectroscopy to characterize chemically modified GaP surfaces containing grafted cobalt fluoro-porphyrins is presented in Chapter 4. In these hybrid constructs, porphyrin surface attachment is achieved using either a two-step method involving coordination of cobalt fluoro-porphyrin metal centers to nitrogen sites

on an initially applied thin-film polypyridyl surface coating, or via a direct modification strategy using a cobalt fluoro-porphyrin precursor bearing a covalently bonded 4- vinylphenyl surface attachment group. Finally, Chapter 5 describes binuclear copper porphyrins in which two copper porphyrin macrocycles are doubly fused at the *meso*-β positions are shown to be active electrocatalysts for the hydrogen evolution reaction. The enhancement in catalytic performance over analogous non-fused copper porphyrins indicates extended macrocycles provide an advantageous structural motif and design element for preparing electrocatalysts that activate small molecules of consequence to renewable energy.

DEDICATION

for my husband and my family

ACKNOWLEDGMENTS

The author of this work wishes to express sincere gratitude to Dr. Gary F. Moore for the opportunity to work in his laboratory, his constant support, encouragement, professional and academic guidance, help in designing experiments, interpreting results, and editing this dissertation.

Ana L. Moore and William T. Petuskey are greatly appreciated for their willingness to serve on my committee.

A special thank you is given to a former colleague, Dr. Anna Beiler, for her continuous support and help, and Brian Wadsworth for his strong support, contributions, and suggestions. The author also wishes to thank the colleagues, Edgar Reyes Cruz, Sam Jacob, Sylvia Nanyangwe, Jennifer Urbine, as well as the staff at Arizona State University, especially Dr. Marco Flores, Dr. Paul A. Liddell, Dr. Brian Cherry, Dr. Tim Karcher, Dr. Diana Convey, Dr. Gwyneth Gordon, Ziva Lackoff, and David Nutt.

The financial support of the National Science Foundation, Light Works, School of Molecular Sciences and Graduate College of Arizona State University is also gratefully acknowledged.

Finally, the author is deeply indebted to her husband and her family for their unrelenting support and continued demonstration of excessive patience and understanding.

TABLE OF CONTENTS

Page

LIST OF TABLES viii

LIST OF FIGURES ix

LIST OF ABBREVIATIONS xxi

CHAPTER

1 INTRODUCTION 1

1.1 Alternative Energy Storage 2

1.2 Metalloporphyrins 3

1.3 Catalysis 4

1.4 Homogeneous Catalysis 5

1.4.1 Fused Metalloporphyrins 6

1.5 Heterogeneous Catalysis 8

1.5.1 Metalloporphyrins for Heterogeneous Solar H_2 Evolution 11

1.5.2 Surface Characterization Methods 12

1.6 Outlook and Conclusions 14

1.7 References 14

2 COBALT AND IRON PORPHYRIN-MODIFIED GALLIUM PHOSPHIDE SURFACES FOR SOLAR HYDROGEN PRODUCTION 21

2.1 Introduction 22

2.2 Results and Disscussion 23

2.2.1 Materials Preparation 23

2.2.2 Surface Characterization via GATR-FTIR and XP Spectroscopies 25

2.2.3 Photoelectrochemical Measurements 31

CHAPTER Page

2.2.4 Turnover Frequency 38

2.3 Conclusions 39

2.4 References 40

3 SYNTHESIS AND CHARACTERIZATION OF A COBALT FLUORO-PORPHYRIN WITH A BUILT-IN SURFACE ATTACHMENT MOIETY 43

3.1 Introduction 44

3.2 Results and Disscusion 45

3.2.1 Materials and Preparation 45

3.2.2 Synthesis and Characterization 46

3.2.3 Electrochemical Studies 52

3.3 Conclusions 54

3.4 References 55

4 VIBRATIONAL STRUCTURAL ANALYSIS OF COBALT FLUORO-PORPHYRIN SURFACE COATINGS VIA GATR-FTIR 58

4.1 Introduction 59

4.2 Results and Disscusion 60

4.2.1 Materials Preparation 60

4.2.2 FTIR Characterization 63

4.2.3 GATR-FTIR Analysis 65

4.2.4 XP Spectroscopy Studies 70

4.3 Conclusions 71

4.4 References 72

CHAPTER Page

5 BINUCLEAR COPPER FUSED PORPHYRINS FOR ELECTROCATALYTIC HYDROGEN EVOLUTION REACTION 75

5.1 Introduction 76

5.2 Results and Disscusion 77

5.2.1 Materials Preparation 77

5.2.2 Structural Characterization 78

5.2.3 Electrochemical Studies 83

5.2.4 UV-Vis-NIR-SEC and IR-SEC Measurements 85

5.2.5 Electrocatalytic Activity for HER. 90

5.2.6 Hydrogen Detection via Rotating Ring-Disk. 99

5.2.7 Acid Stability. 101

5.3 Conclusions 102

5.4 References 103

6 EXPERIMENTAL PROCEDURES 106

6.1 General Experimental Methods 107

6.2 Experimental Procedures for Chapter 2 108

6.3 Experimental Procedures for Chapter 3 124

6.4 Experimental Procedures for Chapter 4 132

6.5 Experimental Procedures for Chapter 5 133

6.6 References 147

COMPLETE BIBLIOGRAPHY 149

APPENDIX

A ACKNOWLEDGEMENTS FOR PERMISSION 163

LIST OF TABLES

Table Page

Table 2.1 Midpoint Potentials for the Reduction of 3 and 4. 36

Table 2.2 PEC Characteristics of GaP, CoP|GaP, and FeP|GaP Photocathodes..... 37

Table 3.1 Midpoint Potentials for the Reduction, ^{nI}E, and Oxidation, ^{ni}E, of 9.. 54

Table 4.1 In-plane Cobalt Porphyrin Deformation Frequencies Measured Using Samples Composed of 10, 9, 3, or 1 in KBr. 65

Table 4.2 In-plane Cobalt Porphyrin Deformation Frequencies Measured on Surfaces of CoT3FPP|PVP|GaP, CoT3FPP|GaP, CoP|PVP|GaP, and CoP|GaP..... 69

Table 5.1 Parameters Used to Fit the EPR Spectra of CuP and Cu_2FP Complexes at Low Temperature. 81

Table 5.2 Midpoint Potentials for the Reduction and Oxidation of CuP and Cu_2FP Complexes as Determined by Cyclic Voltammetry in Dichloromethane. 83

LIST OF FIGURES

Figure Page

Figure 1.1. Schematic Depiction of a Core Porphyrin Unit Highlighting the Synthetic Versatility for Applications in Catalyzing the Hydrogen Evolution Reaction. 3

Figure 1.2. Molecular Structure of Binuclear Copper Fused Porphyrin. 7

Figure 1.3. Structural Representation of the Cobalt and / or Iron Porphyrin-functionalized Gallium Phosphide Surface. 11

Figure 1.4 Structural Representations Depicting the Architectures Resulting from Two Distinct Attachment Methods Used to Prepare Cobalt Fluoro-porphyrin Surface Coatings on Gallium Phosphide (where M = Co). 13

Figure 2.1. Schematic Representation of Chemically Modified Cobalt or Iron Porphyrin Complexes Directly Attached to the GaP Surface for Photoelectrosynthetic Hydrogen Production. 23

Figure 2.2. Schematic Representation of the Attachment Strategy Used to Assemble Metalloporphyrin Modified Gallium Phosphide Wafers (See Main Text for Further Details). 24

Figure 2.3. GATR-FTIR Absorption Spectra of Unmodified GaP(100) Before (Gray) and After (Black) Etching with HF Solution (6:1 HF/NH_4F in H_2O). 25

Figure 2.4. GATR-FTIR Absorption Spectra of CoP|GaP (Green), FeP|GaP (Dark Red), and Unmodified GaP (Black). 26

Figure 2.5. (Left) GATR-FTIR Absorption Spectrum of CoP|GaP (Green) and FTIR Transmission Spectrum of the Cobalt Porphyrin Precursor, Cobalt(II) 5,10,15,20-tetra-*p*-

tolyl-2-(4-vinylphenyl)porphyrin (black) in KBr. (Right) GATR-FTIR Absorption Spectrum of FeP|GaP (Dark Red) and FTIR Transmission Spectrum of the Iron Porphyrin Precursor, Iron(III) 5,10,15,20-tetra-*p*-tolyl-2-(4-vinylphenyl)porphyrin (Black) in KBr. 27

Figure 2.6. (Left) GATR-FTIR Absorption Spectrum Showing the $\nu_{Co–N}$, at the Surface of CoP|GaP (Green) and FTIR Transmission Spectrum Showing the $\nu_{Co–N}$ of the Non-surface Attached Cobalt Porphyrin (Black) in KBr. (Right) GATR-FTIR Absorption Spectrum Showing the $\nu_{Fe–N}$ at the Surface of FeP|GaP (Dark Red) and FTIR Transmission Spectrum Showing the $\nu_{Fe–N}$ of the Non-surface-attached Iron Porphyrin (Black) in KBr.....28

Figure 2.7. FTIR Transmission Spectra of 5,10,15,20-tetra-*p*-tolylporphyrin (Black), Cobalt(II) 5,10,15,20-tetra-*p*-tolyl-2-(4-vinylphenyl)porphyrin (Green), and Iron(III) 5,10,15,20-tetra-*p*-tolyl-2-(4-vinylphenyl)porphyrin Chloride (Dark Red) in KBr. 29

Figure 2.8. XP Survey Spectra of CoP|GaP (Green) and FeP|GaP (Dark Red). 30

Figure 2.9. Co 2p Core Level XP Spectrum of CoP|GaP (Green) and Fe 2p (Dark Red) Core Level XP Spectrum of FeP|GaP. 31

Figure 2.10. Chronoamperograms Using CoP|GaP (Green) or FeP|GaP (Dark Red) Working Electrodes Polarized at a Constant Potential of 0 V vs RHE and Under 1-sun Illumination (100 mW cm^{-2}). 32

Figure 2.11. Linear Sweep Voltammograms Recorded in the Dark (Dashed) or Under 1-sun Illumination (Solid) Using Unmodified GaP(100) (Black), CoP|GaP (Green), or

Figure Page

FeP|GaP (Dark Red) Working Electrodes Collected in a Three-electrode Electrochemical Cell in Phosphate Buffer (pH 7). 32

Figure 2.12. A Photograph of a CoP|GaP Photocathode (Insert) Under Photoelectrochemical Testing. 33

Figure 2.13. Gas Chromatograms Obtained Using Samples of Headspace Gas Collected from Sealed Photoelectrochemical Cells Containing Working Electrodes Polarized at a Constant Potential of 0 V vs RHE and Under 1-sun Illumination. The Amount of Hydrogen Produced in These Experiments Corresponds to a Faradaic Efficiency of 97% Following 30 min of Illumination Using CoP|GaP and 45% Following 6 min of Illumination Using FeP|GaP Sample. 34

Figure 2.14. Gas Chromatograms Obtained Using Gas Samples of the Headspace Collected from a Sealed Photoelectrochemical Cell Equipped with a CoP|GaP Working Electrode Polarized at 0 V vs RHE. The Samples Were Collected Before (Dash-Dotted) and After (Solid) 30 min of Illumination (100 mW cm^{-2}). 35

Figure 2.15. Cyclic Voltammograms Recorded Using Butyronitrile Solutions of Model Cobalt Porphyrin, 3, (Green) or Iron Porphyrin, 4, (Dark Red) Compounds. 36

Figure 2.16. Photocurrent Density Recorded at Increasing Illumination Intensity Using a CoP|GaP Working Electrode Polarized at 0 V vs RHE in Phosphate Buffer (pH 7). 38

Figure 3.1. Synthetic Scheme Used to Prepare Cobalt(II) 5,10,15,20-tetrakis(3-fluorophenyl)-2-(4-vinylphenyl)porphyrin Where (a) NBS, $CHCl_3$, Ar, Reflux; (b) 4-VPBA, K_2CO_3, $Pd(Ph_3)_4$, Reflux; (c) $Co(OAc)_2*4H_2O$, DMF, Reflux. 46

Figure Page

Figure 3.2. ^{1}H NMR Spectra Showing the Symmetry of β-pyrrolic Protons of Compound 6 (Top Left) and Compound 7 (Bottom Left). MALDI-TOF MS Data Showing the Isotopic Distribution Patterns of 6 (Top Center) and 7 (Bottom Center). Corresponding Molecular Structures of 6 (Top Right) and 7 (Bottom Right). 47

Figure 3.3. (Left) Molecular Structural Fragment of Compound 8 Depicting a Conformation in which the Fluorine of a 3-fluorophenyl Group is Exposed to the Ring Current of the Nearby 4-vinylphenyl Moiety; (Right) ^{1}H NMR Spectrum Showing the Vinylic Proton Region of 8 and the Overlaid gCOSY Spectrum. 49

Figure 3.4. ^{19}F NMR of Compound 8 Showing the Unique Magnetic Environments of the Four Fluoro Groups, Including a Significantly Upfield Resonance Centered at –117.86 ppm. 49

Figure 3.5. FTIR Transmission Spectrum of 9 Collected in KBr (Top) and an Expanded Plot of the 961–1039 cm^{-1} Region (Bottom), Showing the Transmission Spectrum of 9 (Solid) as Well as the Free-base Precursor 3 (Dashed).....51

Figure 3.6. Experimental (Top) and Simulated (Bottom) X-band (9.44 GHz) EPR Spectra of 9 Collected at 4 K in Dichloromethane. 52

Figure 3.7. Cyclic Voltammogram of 9 Recorded in 0.1 M Tetrabutylammonium Hexafluorophosphate in Butyronitrile Under Argon Using a Glassy Carbon Electrode and a Scan Rate of 500 mV s^{-1}.....53

Figure 4.1. Structural Representations of Cobalt Fluoro-porphyrin Surface Coatings on Gallium Phosphide.....59

Figure 4.2. Schematic Representation Depicting the Attachment Methods, Materials, and Reagents Used to Prepare Cobalt Fluoro-porphyrin Surface Coatings on Gallium Phosphide (See Main Text for Details).....62

Figure 4.3. Molecular Structures of the Fluorinated and Non-fluorinated Model Compounds and Precursors, Including Cobalt(II) 5,10,15,20-tetrakis(3-fluorophenyl)porphyrin (10), Cobalt(II) 5,10,15,20-tetrakis(3-fluorophenyl)-2-(4-vinylphenyl)porphyrin (9), Cobalt(II) 5,10,15,20-tetra-*p*-tolylporphyrin (3), and Cobalt(II) 5,10,15,20-tetra-*p*-tolyl-2-(4-vinylphenyl)porphyrin (1) Used to Assemble CoT3FPP|PVP|GaP, CoT3FPP|GaP, CoP|PVP|GaP, and CoP|GaP, Respectively. (Right Panel) FTIR Transmission Spectra of 10 (Dark Blue), 9 (Green), 3 (Black), and 1 (Red) Collected in KBr. 64

Figure 4.4. (a) FTIR Transmission Spectrum of 10 Collected in KBr, Included to Facilitate Comparisons, as Well as (b) GATR-FTIR Absorption Spectra Collected Using Samples of GaP (Black), PVP|GaP (Blue), CoT3FPP|PVP|GaP (Dark Blue), and CoT3FPP|GaP (Green). Surface Vibrational Modes Associated with Immobilized Cobalt Fluoro-porphyrin Species Are Labeled with *.....67

Figure 4.5. GATR-FTIR Absorption Spectra of CoT3FPP|GaP (Green) and CoT3FPP|PVP|GaP (Dark Blue) Samples Showing an Eight Wavenumbers Difference in Vibrational Frequency of the In-plane Metalloporphyrin Deformation Mode. 70

Figure 4.6. High-energy Resolution Core Level XP Spectra of the Co $2p_{3/2}$ Region Recorded Using Samples of CoT3FPP|GaP (Green) and CoT3FPP|PVP|GaP (Dark Blue). 71

Figure Page

Figure 5.1. Molecular Structures of (a) Copper Fused Porphyrin, Cu_2FP, and (b) Non-fused Monomeric Copper Porphyrin, CuP.....77

Figure 5.2. Experimental (Red or Blue) and Simulated (Black) X-band (9.44 GHz) EPR Spectra of (a) CuP and (b) Cu_2FP Collected in Dichloromethane at 30 K or 40 K Respectively.....78

Figure 5.3. High-energy Resolution Core Level XP Spectra of Cu 2p Region Recorded Using Samples of Cu_2FP (Blue) or CuP (Red) Dropcasted onto a Glassy Carbon Disk...82

Figure 5.4. Cyclic Voltammograms of Cu_2FP (Blue) and CuP (Red) Recorded in a 0.1 M Tetrabutylammonium Hexafluorophosphate Dichloromethane Solution Using a 3 mm Diameter Glassy Carbon Electrode and a Scan Rate of 500 mV s^{-1} Under (a) Non-rotating Conditions and 0.34 mM in Porphyrin and (b) Rotating (1000 RPM) Conditions and 0.1 mM in Porphyrin.....84

Figure 5.5. Differential Pulse Voltammetry Data Recorded Using Cu_2FP (0.1 mM) (Blue) or CuP (0.1 mM) (Red) in a 0.1 M $TBAPF_6$ Dichloromethane Solution Under Argon. All Measurements Were Recorded Using a 3 mm Diameter Glassy Carbon Working Electrode at Room Temperature and the Ferrocenium/ferrocene Redox Couple as an Internal Reference. 85

Figure 5.6. Absorption Spectra of (a) Cu_2FP and (b) CuP Recorded in Dichloromethane. 86

Figure 5.7. (a and b) UV−Vis-NIR Absorption Spectra of Cu_2FP (6.5 μM) Recorded in a 0.1 M $TBAPF_6$ Benzonitrile Solution Polarized at Potentials to Generate Cu_2FP (Blue),

Cu_2FP^{1-} (Black), and Cu_2FP^{2-} (Green). 87

Figure 5.8. UV–Vis Absorption Spectra of CuP (25 μM) Recorded in a 0.1 M $TBAPF_6$ Benzonitrile Solution Polarized at Potentials to Generate CuP (Red) and CuP^{1-} (Dark Red). 88

Figure 5.9. FTIR Absorption Spectra of (c) CuP (0.4 mM) Polarized at Potentials to Generate CuP (Red) and CuP^{1-} (Black) as Well as (d) Cu_2FP (0.4 mM) Polarized at Potentials to Generate Cu_2FP (Blue), Cu_2FP^{1-} (Black), and Cu_2FP^{2-} (Green) Collected in a 0.1 M $TBAPF_6$ Dichloromethane Solution. 89

Figure 5.10. Voltammogram of 0.01 mM Cu_2FP in a 0.1 M $TBAPF_6$ Dichloromethane Solution with 65 mM TFA Recorded at 600 mV s^{-1}. All Potentials Are Reported Versus the HA/H_2 Equilibrium Potential in Dichloromethane, Calculated Using the Open Circuit Potential Method Developed by Bullock and Roberts. 91

Figure 5.11. Plot of i_{cat} Versus the Scan Rate for 0.01 mM Cu_2FP in a 0.1 M $TBAPF_6$ Dichloromethane Solution with 19.5 mM TFA. 92

Figure 5.12. Plot of i_{cat}/i_p Versus the Square Root of the Concentration of TFA. The Plateau Currents Are Taken from Cyclic Voltammograms Recorded at 600 mV s^{-1} Using 0.01 mM Cu_2FP in a 0.1 M $TBAPF_6$ Dichloromethane Solution with 19.5−84.5 mM TFA. 93

Figure 5.13. Plot of k_{obs} Versus the Concentration of TFA. The Data Points Used to Calculate Are the i_{cat}/i_p Values from the Plot of i_{cat}/i_p Versus the Square Root of the Concentration of TFA Shown in Figure 5.12. 95

Figure Page

Figure 5.14. Voltammograms of (a) 0.01 mM Cu_2FP (Blue) and 0.01 mM CuP (Red) as Well as (b) 0.01 mM (Blue) and 0.1 mM (Dark Blue) Cu_2FP Recorded in a 0.1 M $TBAPF_6$ Dichloromethane Solution Using a 1 mm Diameter Glassy Carbon Electrode and a Scan Rate of 100 mV s^{-1} in the Presence of 16.25 (Solid) or 32.5 (Dash) mM TFA. 96

Figure 5.15. Voltammograms of 0.01 mM Cu_2FP Recorded in a 0.1 M $TBAPF_6$ Dichloromethane Solution at a Scan Rate of 100 mV s^{-1} with Either 0 mM (Black Solid), 16.25 mM (Blue Solid), or 32.5 mM (Blue Dashed) mM TFA. 98

Figure 5.16. Rotating Ring-disk Measurements (100 mV s^{-1}) of Hydrogen Evolution Using 0.01 mM of Cu_2FP in a Dichloromethane Solution with 0.1 M $TBAPF_6$ Electrolyte and 2.6 mM TFA at a Glassy Carbon Electrode. (Top) GC Disk Potential. (Middle) GC Disk Current. (Bottom) Pt-ring Current (the Pt Ring Was Held at 0.79 V vs Fc^+/Fc). ...100

Figure 5.17. Absorption Spectra of Cu_2FP (12.5 μM) Recorded in (a) Dichloromethane or (b) Benzonitrile in the Absence (blue) or Presence (Black) of TFA (87.5 mM) After 4 h. 101

Figure 6.1. Synthetic Scheme Used to Prepare 1 or 2 where (a) $BF_3(OEt)_2$, $CHCl_3$, DDQ, Ar; (b) NBS, $CHCl_3$, Ar, Reflux; (c) 4-VPBA, K_2CO_3, $Pd(Ph_3)_4$, Reflux; (d) $Co(Ace)_2*4H_2O$ or $Fe(Cl)_3*3H_2O$, DMF, Reflux. 109

Figure 6.2. 400 MHZ ^1H NMR Spectrum of 5,10,15,20-tetra-*p*-tolylporphyrinrecorded in Chloroform-d. ^1H NMR (400 MHz, $CDCl_3$): δ –2.77 (2H, s, NH), 2.70 (12H, s, CH_3), 7.55 (8H, d, J = 7.8 Hz, ArH), 8.09 (8H, d, J = 7.8 Hz, ArH) 8.85 (8H, s, βH). 116

Figure Page

Figure 6.3. 400 MHZ ^{1}H NMR Spectrum of *β*-bromo-5,10,15,20-tetra-*p*-tolylporphyrin Recorded in Chloroform-d. ^{1}H NMR (400 MHz, $CDCl_3$): δ –2.85 (2H, s, NH), 2.70 (12H, s, CH_3), 7.58-7.50 (8H, m, ArH), 7.95 (2H,d, *J* = 7.8 Hz, ArH), 8.10 (2H, d, *J* = 7.8 Hz, ArH) 8.10 (2H, d, *J* = 7.5 Hz, ArH), 8.10 (2H, d, *J* = 7.3 Hz, ArH), 8.93-8.74 (7H, m, βH). 117

Figure 6.4. 400 MHZ ^{1}H NMR Spectrum of 5,10,15,20-tetra-*p*-tolyl-2-(4-vinylphenyl)porphyrin Recorded in Chloroform-d. ^{1}H NMR (400 MHz, $CDCl_3$) δ –2.63 (2H, s, NH), 2.38 (3H, s, CH_3), 2.67 (3H, s, CH_3), 2.70 (6H, s, CH_3), 5.25 (1H, d, *J* = 11.1 Hz, CH), 5.78 (1H, d, *J* = 17.7 Hz, CH), 6.76 (1H, dd, *J* = 17.6 Hz, *J* = 10.87 Hz, CH), 7.01 (2H, d, *J* = 7.7 Hz, ArH), 7.18 (2H, d, *J* = 8.1 Hz, ArH), 7.25 (2H, d, *J* = 7.9 Hz, ArH), 7.51 (2H, d, *J* = 7.8 Hz, ArH), 7.54 (2H, d, *J* = 7.6 Hz, ArH), 7.56 (2H, d, *J* = 7.6 Hz, ArH), 7.73 (2H, d, *J* = 7.9 Hz, ArH), 8.09 (2H, d, *J* = 7.8 Hz, ArH), 8.10 (2H, d, *J* = 7.8 Hz, ArH), 8.10 (2H, d, *J* = 7.8 Hz, ArH), 8.87-8.74 (7H, m, βH). 118

Figure 6.5. 400 MHZ ^{1}H NMR Spectra (Black) with Overlaid gCOSY (Aromatic Region) of 5,10,15,20-tetra-*p*-tolyl-2-(4-vinylphenyl)porphyrin Recorded in Chloroform-d.....119

Figure 6.6. (Left) Absorption Spectra of 5,10,15,20-tetra-*p*-tolyl-2-(4-vinylphenyl)porphyrin Recorded in Toluene Showing the Soret Band Normalized to 1 (Solid) and the Highest Energy Q-Band Normalized to 0.5 (Dashed). (Right) Normalized Absorbance Spectra Showing the Lowest Energy Q-Bands of the Model Compound 5,10,15,20-tetra-*p*-tolylporphyrin (Dashed) and 5,10,15,20-tetra-*p*-tolyl-2-(4-vinylphenyl)porphyrin (Solid) are Included for Comparison. 120

Figure 6.7. (Left) Absorbance Spectra of 1 Recorded in Toluene Showing the Soret Band

Normalized to 1 (Solid) and the Highest Energy Q-Band Normalized to 0.5 (Dashed). (Right) Normalized Absorbance Spectra Showing the Lowest Energy Q-Bands of the Model Compound 3 (Dashed) and 1 (Solid) Are Included for Comparison.....121

Figure 6.8. (Left) Absorbance Spectra of 2 Recorded in Toluene Showing the Soret Band Normalized to 1 (Solid) and the Highest Energy Q-Band Normalized to 0.5 (Dashed). (Right) Normalized Absorbance Spectra Showing the Lowest Energy Q-Bands of the Model Compound 4 (Dashed) and 2 (Solid) Are Included for Comparison.....121

Figure 6.9 400 MHZ ^{1}H NMR Spectrum of 2-bromo-5,10,15,20-tetrakis(3-fluorophenyl) Porphyrin (7) Recorded in Chloroform-d. ^{1}H NMR (400 MHz, $CDCl_3$): δ –2.94 (2H, s, NH), 7.47–7.57 (4H, m, ArH), 7.64–7.76 (4H, m, ArH), 7.78–8.01 (8H, m, ArH), 8.75–8.95 (7H, m, βH). 129

Figure 6.10. 400 MHZ ^{1}H NMR Spectrum of 5,10,15,20-tetrakis(3-fluorophenyl)-2-(4-vinylphenyl) Porphyrin (8) Recorded in Chloroform-d. ^{1}H NMR (400 MHz, $CDCl_3$): δ –2.72 (2H, s, NH), 5.30 (1H, d, J = 12 Hz, CH), 5.78 (1H, d, J = 20 Hz, CH), 6.76 (1H, dd, J = 20 Hz, J = 12 Hz, CH) 7.02 (1H, td, J = 8 Hz, J = 2 Hz, ArH), 7.20 (1H, q, ArH), 7.26 (2H, d, J = 8 Hz, ArH), 7.33 (2H, d, J = 8 Hz, ArH), 7.44–7.62 (4H, m, ArH), 7.64–7.77 (4H, m, ArH), 7.90–8.04 (6H, m, ArH), 8.69–8.90 (7H, m, βH). 130

Figure 6.11. Photograph of the Electrochemical Setup Used for Rotating Ring-disk Experiments. 141

Figure 6.12. ^{1}H NMR Spectra of (Top) 5,10,15,20-tetra-*p*-tolylporphyrin and (Bottom) *meso*-β doubly-fused 5,24-di(*p*-tolyl)-10,19,29,38-tetramesitylporphyrin in Chloroform-d 142

Figure 6.13. Voltammograms of Cu_2FP (0.01 mM) Collected in a 0.1 M $TBAPF_6$ Dichloromethane Solution Under Argon with an Increasing Amount of TFA (19.5–84.5 mM) and at a Scan Rate of 600 mV s^{-1}.....143

Figure 6.14. Voltammograms of Cu_2FP (0.01 mM) Collected in a 0.1 M $TBAPF_6$ Dichloromethane Solution Under Argon with TFA (19.5 mM) and at Scan Rates of 300–900 mV s^{-1}.....143

Figure 6.15. Linear Sweep Voltammograms Recorded Using a Glassy Carbon Working Electrode in a 0.01 mM Cu_2FP Solution (Blue Solid) or in a Solution without Cu_2FP Present, Following Collection of the Blue Linear Sweep Voltammogram and Rinsing the Electrode Surface with Fresh Dichloromethane (Purple Solid).....144

Figure 6.16. Voltammograms of 0.01 mM Cu_2FP Recorded in a 0.1 M $TBAPF_6$ Dichloromethane Solution at a Scan Rate of 600 mV s^{-1} with 65 mM TFA using Either a 3 mm Glassy Carbon Disk (Yellow) or a Platinum Wire (Maroon and Green) as the Counter Electrode. 144

Figure 6.17. Voltammograms of 0.1 mM Cu_2FP Recorded in a 0.1 M $TBAPF_6$ Dichloromethane Solution at a Scan Rate of 600 mV s^{-1} with 65 mM TFA Using Either a 3 mm Glassy Carbon Disk (Yellow) or a Platinum Wire (Maroon and Blue) as the Counter Electrode. 145

Figure 6.18. Voltammograms of 0.01 mM Cu_2FP (Blue) and 0.01 mM CuP (Red) Recorded in a 0.1 M $TBAPF_6$ Dichloromethane Solution at a Scan Rate of 100 mV s^{-1} with Either 16.25 mM (Solid) or 32.5 mM (Dashed) TFA. Voltammograms Recorded Using Porphyrin-free Solutions of 0.1 M $TBAPF_6$ in Dichloromethane at a Scan Rate of

100 mV s^{-1} (Black), with Either 16.25 mM (Solid) or 32.5 mM (Dashed) TFA, Are Included for Comparison. All Voltammograms Were Recorded Using a 1 mm Diameter Glassy Carbon Working Electrode at Room Temperature and the Ferrocenium/ferrocene Redox Couple as an Internal Reference. 145

Figure 6.19. Voltammograms of 0.01 mM Cu_2FP (Blue) and 0.02 mM CuP (Pink) Recorded in a 0.1 M $TBAPF_6$ Dichloromethane Solution at a Scan Rate of 100 mV s^{-1} with Either 16.25 mM (Solid) or 32.5 mM (Dashed) TFA. 146

Figure 6.20. (b) Voltammograms of 0.1 mM Cu_2FP (Dark Blue) and 0.2 mM CuP (Orange) Recorded in a 0.1 M $TBAPF_6$ Dichloromethane Solution at a Scan Rate of 100 mV s^{-1} with Either 16.25 mM (Solid) or 32.5 mM (Dashed) TFA. 146

Figure 6.21. Voltammograms of 0.1 mM Cu_2FP (Dark Blue) and 0.1 mM CuP (Dark Red) Recorded in a 0.1 M $TBAPF_6$ Dichloromethane Solution at a Scan Rate of 100 mV s^{-1} with Either 16.25 mM (Solid) or 32.5 mM (Dashed) TFA. 147

Figure 6.22. MALDI-TOF MS Data Collected Using Samples of Cu_2FP Following 4 h of Exposure to a Solution of 87.5 mM TFA (7000 Equivalents of TFA with Respect to the Concentration of Cu_2FP Used in these Experiments / 12.5 μM in Cu_2FP) in Dichloromethane. 147

LIST OF ABBREVIATIONS

Abbreviation	Meaning
AFM	Atomic force microscopy
ATR	Attenuated total reflectance
DDQ	2,3-dichloro-5,6-dicyano-1,4-benzoquinone
DMF	Dimethylformamide
Cu_2FP	biCu(II) *meso*-β doubly-fused 5,24-di(*p*-tolyl)-10,19,29,38-tetramesitylporphyrin
CuP	Cu(II) porphyrin, copper(II) 5,10,15,20-tetra-*p*-tolylporphyrin
CV	Cyclic voltammetry
EDS	Energy dispersive spectroscopy
EDX	Energy - dispersive X-ray spectroscopy
EPR	Electron paramagnetic resonance
EQE	External quantum efficiency
FE	Faradaic efficiency
FBFP	*meso*-β doubly-fused 5,24-di(*p*-tolyl)-10,19,29,38-tetramesitylporphyrin
FTIR	Fourier-transform infrared
F	Faraday constant
GaP	Gallium phosphide
GATR	Grazing angle attenuated total reflectance

gCOSY	Gradient correlation spectroscopy
GC	Glassy carbon
hfc	Hyperfine coupling
HER	Hydrogen evolution reaction
HOMO	Highest occupied energy level
ICP-MS	Inductively coupled plasma mass spectroscopy
IR-SEC	Infrared spectroelectrochemistry
LUMO	Lowest occupied energy level
MALDI-TOF MS	Matrix assisted laser desorption/ionization time-of-flight mass spectrometer
NBS	N-bromosuccinamide
NMR	Nuclear magnetic resonance
PEC	Photoelectrochemical
RHE	Reversible hydrogen electrode
RRDE	Rotating ring-disk electrode
SCE	Standard calomel reference electrode
SEC	Spectroelectrochemistry
SEM	Scanning electron microscopy
$TBAPF_6$	Tetrabutylammonium hexafluorophosphate
TEM	Transmission electron microscopy
TTP	5,10,15,20-tetra-*p*-tolylporphyrin
TLC	Thin-layer chromatography
TON	Turnover number

TOF	Turnover frequency
TFA	Trifluoroacetic acid
UV-Vis	Ultraviolet-visible
V	Volts
V vs Fc^{+}/Fc	Volts versus the ferrocenium/ferrocene
XP	X-ray photoelectron
4-VPBA	4-Vinylphenyl boronic acid
1	Cobalt(II) 5,10,15,20-tetra-*p*-tolyl-2-(4-vinylphenyl)porphyrin
2	Iron(III) 5,10,15,20-tetra-*p*-tolyl-2-(4-vinylphenyl)porphyrin chloride
3	Cobalt(II) 5,10,15,20-tetra-*p*-tolylporphyrin
4	Iron(III) 5,10,15,20-tetra-*p*-tolylporphyrin chloride
5	5,10,15,20-tetra-*p*-tolyl-2-(4-vinylphenyl)porphyrin
6	5,10,15,20-tetrakis(3- fluorophenyl)porphyrin
7	2-bromo-5,10,15,20-tetrakis (3-fluorophenyl)porphyrin
8	5,10,15,20-tetrakis(3-fluorophenyl)-2-(4-vinylphenyl) porphyrin
9	Cobalt(II) 5,10,15,20-tetrakis(3-fluorophenyl)-2-(4-vinylphenyl) porphyrin
10	Cobalt(II) 5,10,15,20-tetrakis(3-fluorophenyl)porphyrin
CoP|GaP	GaP modified with 1
FeP|GaP	GaP modified with 2

PVP|GaP	GaP modified with PVP
CoP|PVP|GaP	GaP modified with PVP and 3
CoT3FPP|GaP	GaP modified with 9
CoT3FPP|PVP|GaP	GaP modified with PVP and 10

CHAPTER 1 INTRODUCTION

Portions of this work are excerpted with permission from:

Khusnutdinova, D.; Wadsworth, B. L.; Flores, M.; Beiler, A. M.; Reyes, E. A.; Zenkov, Y.; Moore, G. F. *ACS Catal.* **2018**, *8* (10), 9888–9898.

Khusnutdinova, D.; Beiler, A. M.; Wadsworth, B. L.; Nanyangwe, S. K.; Moore, G. F. *J. Porphyr. Phthalocyanines* **2018**, *22* (6), 461–466.

Khusnutdinova, D.; Flores, M.; Beiler, A. M.; Moore, G. F. *Photosynthetica* **2018**, *56* (1), 67–74.

Khusnutdinova, D.; Beiler, A. M.; Wadsworth B. L.; Jacob S. I.; Moore G. F. *Chem. Sci.* **2017**, *8* (1), 253–259.

1.1 Alternative Energy Storage

Energy and environmental issues will likely dominate science and society for the next several decades as climate change threatens the wellbeing of the planet.[1] The most abundant, renewable energy supply is solar. However, the diffuse and intermittent nature of sunlight hinders global-scale applications for meeting our society`s technological energy demands. Thus, effective methods for coupling the capture and conversion of solar energy (including applications of existing photovoltaic technologies) with storage mechanisms represents an outstanding challenge in the field of renewable energy and chemical sciences. Using the process of photosynthesis as inspiration, solar energy can be stored in the form of chemical bonds, producing fuels and other value-added chemical products. In this scenario, the development of advanced materials, processes, and techniques for controlling matter and energy at the nanoscale is receiving increased global attention[2] as a technological path to restoring a safe operating space for humanity.[3,4]

Technologies for producing and using carbon-neutral fuels such as hydrogen, an energy-dense chemical by mass (143 MJ kg), could provide a path towards universal access to clean and affordable energy while limiting the environmental impact. Hydrogen production using water splitting electrolyzers powered by photovoltaics offer one strategy for producing fuels using solar energy.[5] The hydrogen evolution reaction (HER) ($2H^+ + 2\ e^- \rightarrow H_2$), a half-reaction fundamental to several chemical transformations with relevance to energy transduction, is among the simplest proton-coupled electron transfer reactions. The long-established industrial catalyst for activating this transformation is elemental platinum. However, concerns that future market demands for platinum and other rare-earth elements could outpace availability have prompted researchers to seek

alternative materials and design principles to prepare catalysts for the production of hydrogen and other industrially relevant chemicals.[6,7]

In summary, the work presented herein describes the design, synthesis, and characterization of metalloporphyrin HER catalysts and their applications in preparing heterogeneous-homogeneous (photo)electrocatalytic materials.

1.2 Metalloporphyrins

Tetrapyrrolic macrocycles, including metalloporphyrins, serve important roles in biology and as components in emerging molecular-based materials and technologies.[8-17] As electrocatalysts, they are capable of chemically transforming protons into hydrogen as well as converting carbon dioxide into carbon monoxide when electrochemically activated in solution or immobilized at a conductive substrate polarized at an appropriate potential (Figure 1.1).

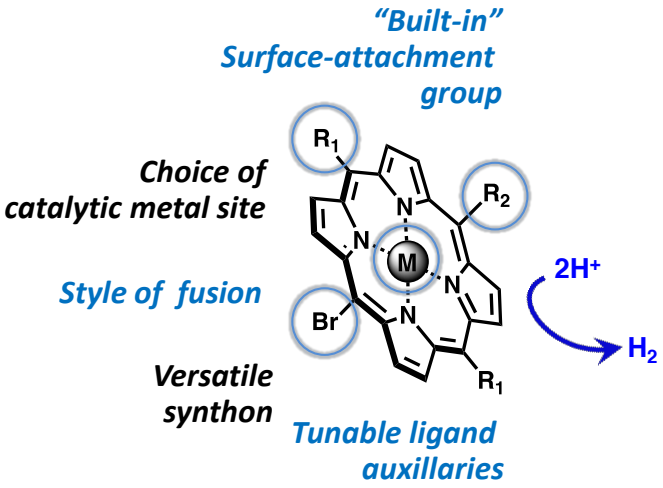

Figure 1.1. Schematic depiction of a core porphyrin unit highlighting the synthetic versatility for applications in catalyzing the hydrogen evolution reaction.

The synthetic versatility of the porphyrin architecture includes, but is not limited to, selection of the catalytic metal site for controlling activity and choice of ligand auxiliaries for tailoring their molecular structure as well as associated electronic properties (Figure 1.1). These structural properties afford opportunities for fundamental studies of energy-relevant chemical conversions and yield molecular-based strategies to design catalysts with enhanced activity to drive a range of redox reactions.

1.3 Catalysis

Catalysts are central to energy conversion in biology and technology.[18-26] They provide low-energy pathways for steering chemical transformations and are used in applications ranging from manufacturing fuels and fine chemicals to controlling the bioenergetic reactions essential to all living organisms.

In the context of chemical catalysis, supported molecular assemblies offer a promising approach to combining favorable features associated with homogeneous catalysts, including enhanced synthetic control over their physical properties. Such hybrid materials have been reported using a range of chemical approaches to assemble molecular components onto conducting or semiconducting substrates.[27-32] In these constructs, chemical transformations can be triggered by application of an electrochemical bias or, in the case of photochemically active materials, by illumination of the sample. In technological processes, the solid-state form factors of heterogeneous electrocatalytic materials make them conducive to many industrial applications, including reactions where they provide a means of activating small molecules at electrified interfaces.[33] Conversely, the study of homogeneous molecular catalysts has provided researchers significant insights regarding mechanisms and active site structure-function relationships governing myriad catalytic processes.[32,34-36] Unlike traditional surface electrocatalysts,

where the active sites are integral to the electrode and are structurally less well-defined, favorable features of homogeneous molecular electrocatalysts include enhanced synthetic control over their physical properties as dictated by their well-defined structures. Thus, they are distinct entities with their own electronic and chemical properties.

1.4 Homogeneous Catalysis

Although heterogeneous catalytic materials dominate industrial applications, the well-defined structures associated with homogeneous molecular catalysts offer opportunities to improve mechanistic insights of the structure-function relationships governing catalytic active sites and their extended coordination environments. In the rapidly developing field of molecular electrocatalysis, researchers continue to explore the use of chemical coordination environments to control the catalytic properties of earth-abundant elements, facilitating mechanistic studies that can be prohibitive in more complex heterogeneous assemblies and thus aiding the design of better homogeneous as well as heterogeneous catalysts.[28,37-40] Reports on the H_2-evolving molecular electrocatalysts are based on earth-abundant elements such as Mo, Ni, Fe, Ni and Co.[32,41-46] Their catalytic performance can be evaluated by kinetic and thermodynamic parameters obtained from electrochemical measurements including the standard benchmarking parameters: turnover number (TON), turnover frequency (TOF), and overpotential.[47]

Cobalt porphyrin electrocatalysts (*e.g.* cobalt *meso*-tetrakis(*N*,*N*,*N*-trimethylanilinium-4-yl)porphyrin) were investigated by Spiro and Kellett for catalysis of hydrogen production from water. As nucleophiles, electrochemically generated Co^{I} species can be protonated to form cobalt hydrides that couple with protons and evolve hydrogen. Controlled-potential electrolysis at -0.95 V vs SCE, show molecular cobalt porphyrins generate H_2 in acidic media (pH 3.4) with ~100% current (Faradaic) efficiency and with no evidence of

catalysts decomposition. However, the adsorption of catalytic material on electrodes (glassy carbon, platinum, or tin oxide), detected as a peak for the return oxidation wave of the catalytic redox couple, complicated kinetic analysis.[48]

Fujita and coworkers have shown that solutions of cobalt porphyrins in organic-based electrolytes can also electrochemically reduce CO_2 to CO and formate when Co^0 species are formed by one-electron reduction of Co^I. The authors also have shown this process can be achieved at less negative potentials, but with smaller catalytic currents, when using fluorinated analogs of the cobalt porphyrins.[49]

Work by Savéant and coworkers show iron porphyrins can serve as homogeneous electrocatalysts for hydrogen evolution when dissolved in an *N, N`*-dimethylformamide electrolyte solution containing protonated triethylamine. In this example, hydrogen is the only product with no significant catalyst degradation after 1 h of electrolysis performed at -1.6 V vs SCE. The proposed electrocatalytic mechanism involves reduction of the iron porphyrin to form Fe^0, which is then protonated to form an iron hydride that further reacts with acid in solution to protonate the hydride and release hydrogen. A theoretical turnover frequency value of $4*10^5$ s^{-1} was extrapolated from the experimental kinetic results collected at low acid concentration.[50]

1.4.1 Fused Metalloporphyrins

Fused bimetallic porphyrin architectures, where two porphyrin macrocycles are doubly or triply connected through *meso*- or β-positions, have been investigated for applications in optics, molecular wires, and organic conducting materials. [51-57] The electrocatalytic properties of this class of compounds have only recently been reported, in a publication by our research group, and are presented as part of this dissertation.

Electrocatalytic properties of a highly active molecular catalyst, binuclear copper(II) fused porphyrin complex (Figure 1.2), for activating the HER are described highlighting the concept of extended aromaticity and the use of fused bimetallic porphyrin as a structural motif for enhancing the catalysis of reductive chemical transformations including the conversion of protons to hydrogen.

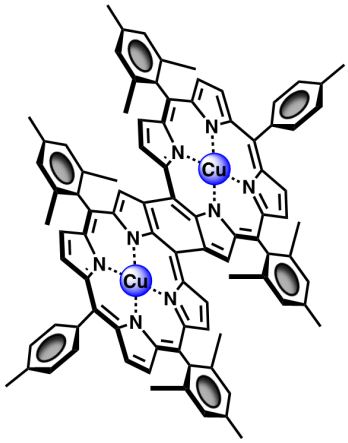

Figure 1.2. Molecular structure of binuclear copper fused porphyrin.

The molecular / electronic structure imposed by fusion of the porphyrin macrocycles creates an extended π-system architecture that is characterized by a relatively large bathochromic shift in absorption spectrum, including the presence of transitions in the near-IR region.[51] The electrochemical properties of fused porphyrins are consistent with the described red-shift in absorption spectrum where the HOMO-LUMO gaps are reduced, shifting the redox potentials for oxidative and reductive processes to less positive and less negative values.

Fused bimetallic porphyrins represent a new class of molecular catalysts that possess favorable properties for applications in electrocatalysis, including the ability to 1) store multiple redox equivalents, 2) delocalize electrons across an extended multi-metallic

scaffold, 3) be reduced as well as oxidized at significantly less applied bias potentials compared to those required for analogous non-fused porphyrins, and 4) provide an alternative strategy, compared to the use of electron-withdrawing or electron-donating functional groups, to adjust the redox properties of molecular catalysts.[58,59]

1.5 Heterogeneous Catalysis

Artificial photosynthesis, which uses concepts inspired by its biological counterpart to produce fuels, is an attractive approach to storing solar energy.[60-63] To this end, the immobilization of molecules on semiconductor materials is gaining interest.[64] Although some recent progress has been made in developing such assemblies,[15,28,65-71] finding new and more effective ways to interface catalysts to semiconductor surfaces remains a major challenge.[32] Immobilization of porphyrins on substrates to produce photoelectrosynthetic or electrocatalytic assemblies that activate energy-related chemical transformations can be achieved through covalent modification of the (semi)conductor surface with molecular catalysts as well as noncovalent bonding strategies to achieve catalyst immobilization including adsorption, electropolymerization, coordination chemistry, or dropcasting. One of the first examples of covalent grafting of cobalt porphyrins onto a glassy carbon electrode for H_2 production in solution was reported by Spiro and coworkers.[72] In their work, cobalt *meso*-tetrakis(2-aminophenyl)porphyrins are chemically bound to a carbon substrate with surface carboxylic acid groups that were converted to the acyl chloride to be linked to the amine functional groups of the porphyrin macrocycle following the metal insertion reaction. The described constructs were studied with cyclic voltammetry in organic and aqueous conditions. In pH 7 phosphate buffer, the cobalt porphyrin-modified glassy carbon surface is active for proton reduction at a potential less than 200 mV negative of the H^+/H_2 equilibrium potential. The recorded activity in aqueous conditions

was 10-fold greater than the current recorded in a dimethyl sulfoxide solution. The rapid decay in catalytic current was observed over time due to disruption of the covalent attachment, causing leaching of cobalt porphyrin catalyst.

Robert *et. al.* assembled pyrene-functionalized iron porphyrins on carbon nanotubes through noncovalent van der Waals π-π interactions between the pyrene functional group and a carbon surface, forming an active hybrid material that converts CO_2 into CO with a Faradaic efficiency of 85% in aqueous conditions.[73] The successful immobilization of molecular species was confirmed with XP spectroscopy and electrochemical testing. A stable catalytic activity was maintained over 12 h corresponding to a turnover number of 813 and a TOF of 72 h^{-1} operating with a 480 mV overpotential. However, the proposed desorption of the pyrene anchors from the surface limits implementation of such catalytic systems.

Robert and coworkers have also shown that iron porphyrins can be covalently grafted on carbon nanotubes, presenting a new strategy that can be applied to other conductive and semiconducting surfaces.[74] First, carbon nanotubes are functionalized with 4-(N-Boc-aminomethyl)benzene groups while refluxing in acetonitrile following the deprotection reaction to form amine groups that react with a molecular iron porphyrin precursor facilitating a covalent bond between the carbon surface and a catalyst. The covalent immobilization was verified using XP spectroscopy and cyclic voltammetry. The functionalized materials convert CO_2-to-CO with a 500 mV overpotential and with a turnover frequency of 178 h^{-1} obtained from a 3 h electrolysis.

A noncovalent porphyrin attachment strategy was described by Brudvig, Wang and coworkers, and is achieved through a deposition of a molecular copper porphyrin complex (copper 5,10,15,20-tetrakis(2,6-dihydroxyphenyl)porphyrin)) onto a carbon

cloth, resulting in an active heterogeneous system that can reduce CO_2 to hydrocarbons in aqueous media.[75] Structural characterization via XPS, SEM, and EDX confirmed the presence of molecular copper porphyrin on the electrode before and after catalytic measurements. The main products of catalysis, methane and ethylene, are generated with rates equal to 4.3 and 1.8 molecules $site^{-1}$ s^{-1}, respectively, when the modified-electrode is polarized at -0.976 V vs RHE. Conversion of CO_2 to hydrocarbons has an associated Faradaic efficiency of 44%, suppressing the alternative reduction pathway of forming hydrogen. Electrochemical studies of the copper functionalized material coupled with Density Function Theory showed that the observed catalytic current at ~ -0.9 V vs RHE is likely correlated with a one-electron redox process Cu^0/Cu^-.

An attachment method used to build hybrid systems for photoelectrosynthetic hydrogen production reported by Beiler and coworkers leverages a coordination chemistry approach in which the metal center of cobalt porphyrins are coordinated to a nitrogen site of a polypyridyl modified gallium phosphide surface.[76] These cobalt porphyrin-modified photocathodes are photoactive for the proton reduction reaction and upon 1-sun illumination, evolve hydrogen from a neutral pH aqueous solution with the rate of 18 mol s^{-1} when polarized at 0 V vs RHE. Surface characterization was performed prior to and after photoelectrochemical characterization by surface-sensitive measurements including XP and GATR-FTIR spectroscopies, as well as ellipsometry, electrochemistry, and IPC-MS spectrometry. Experimental results confirm the molecular modification involving cobalt coordination onto the nitrogen sites of the polymer film. These results include XP analysis of the N 1s peak as well as the value of the in-plane metalloporphyrin deformation mode of the cobalt porphyrin macrocycle as detected by GATR-FTIR spectroscopy. In addition, post-photoelectrochemical analysis provides evidence

supporting the molecular integrity of porphyrin components remain intact. The described attachment method provides a means to assemble a highly active photocathode, but is limited by use of metal centers that can effectively coordinate to pyridinic nitrogens.

1.5.1 Metalloporphyrins for Heterogeneous Solar H_2 Evolution

As part of this dissertation, a novel covalent strategy for assembling metalloporphyrins onto semiconducting surfaces is described. The presented work focuses on the synthetic methodology and structural characterizations of cobalt and iron porphyrin derivatives with a functional group that acts as a surface attachment linker for the photochemical grafting of the porphyrin macrocycle to the surface of a gallium phosphide (GaP) semiconductor. These hybrid constructs are shown to be active for solar hydrogen production (Figure 1.3), achieving activities that are among the highest reported to date.

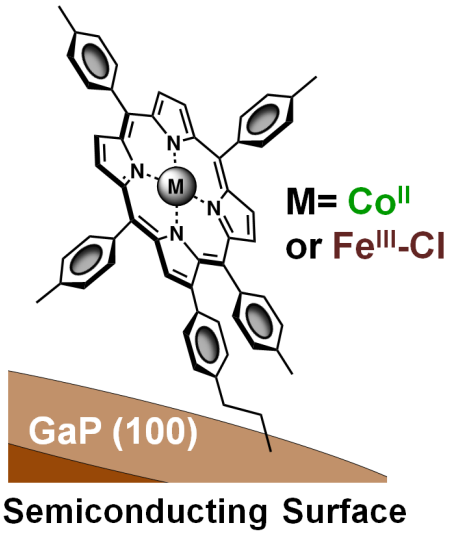

Figure 1.3. Structural representation of the cobalt and / or iron porphyrin- functionalized gallium phosphide surface.

In such hybrid assemblies, the porphyrin-modified surface of the semiconductors harvests the power of the sun for efficient production of net carbon-neutral fuels. The surface

modification leverages a one-step method to chemically graft metalloporphyrin complexes onto p-type GaP(100).

The selection of chemically and structurally different substituents on the porphyrin macrocycles provide a molecular-based strategy for tuning the electrochemical properties of redox catalysts and mediators.[67,77-79] This concept is expanded in this work describing the synthesis and characterization of a cobalt porphyrin substituted with 3-fluorophenyl groups at all four *meso*-positions of the porphyrin ring modified with single 4-vinylphenyl surface attachment group at one of the β- positions. Unmodified fluorinated cobalt porphyrin is a known homogeneous electrocatalyst for the reduction of CO_2 in solution studies.[49,80] Due to the electron-withdrawing nature of the 3-fluorophenyl substituents, electrochemical measurements of the described fluorinated cobalt porphyrin show the $Co^{II/I}$ redox process occurs ≈ 100 mV less negative than that of the nonfluorinated analog. In addition, a second reduction process, occurring at more negative potentials and assigned to the Co^{I}/Co^{0} couple, is clearly resolved within the electrochemical window of the solvent. Fabrication of molecular-modified materials with the reported complex for solar activated CO_2 reduction studies is underway.

1.5.2 Surface Characterization Methods

Molecular-modified surfaces have applications in a range of existing and emerging technologies.[18,81-83] While fundamentally interesting, practical applications of heterogeneous catalytic systems demand improved understanding and control over the structural properties governing the function of these architectures. The list of available surface-sensitive techniques for characterization of heterogeneous catalytic systems prepared via either covalent or noncovalent methods includes: XP spectroscopy, attenuated total reflectance (ATR) or grazing angle attenuated total reflectance Fourier

transform infrared spectroscopy (GATR-FTIR), scanning electron microscopy (SEM), energy dispersive spectroscopy (EDS), transmission electron microscopy (TEM), and atomic force microscopy (AFM).

The surface characterization studies of thin-film modified substrates via GATR-FTIR spectroscopy are presented in this work. The results demonstrate the use of GATR-FTIR spectroscopy as a sensitive tool for characterizing porphyrin-modified surfaces with absorption signals that are close to the detection limits of many common spectroscopic techniques. This study focuses specifically on structural characterization of cobalt fluoro-porphyrin-modified surfaces of gallium phosphide. In these hybrid constructs, porphyrin surface attachment is achieved using either a two-step method, involving coordination of cobalt fluoro-porphyrin metal centers to nitrogen sites on an initially applied thin-film polypyridyl surface coating, or via a direct modification strategy, using a cobalt fluoro-porphyrin precursor bearing a covalently bonded 4-vinylphenyl surface attachment group at a β-position (Figure 1.4).

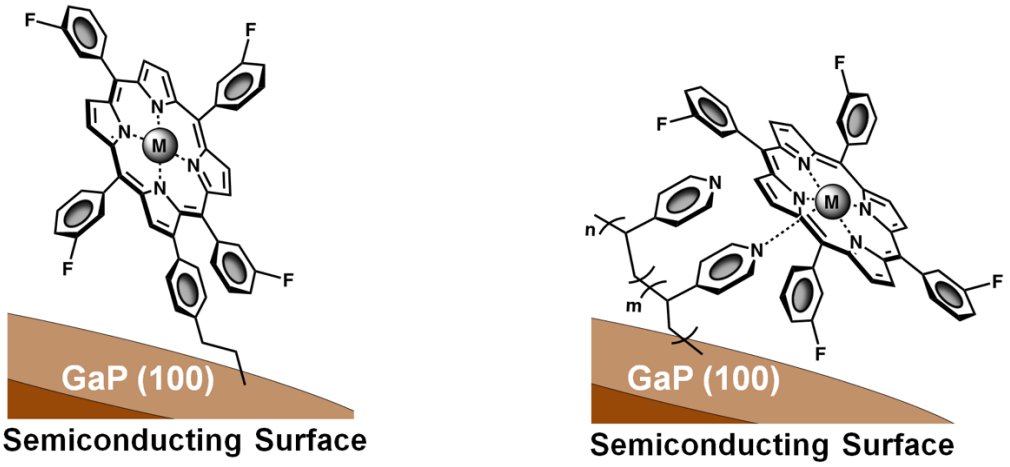

Figure 1.4. Structural representations depicting the architectures resulting from two distinct attachment methods used to prepare cobalt fluoro-porphyrin surface coatings on

gallium phosphide (where M = Co).

Both surface-attachment chemistries leverage the UV-induced immobilization of alkenes but result in distinct structural connectivities of the grafted porphyrin units and their associated vibrational spectra.

1.6 Outlook and Conclusions

Controlling matter and information across the *nano*-, *meso*-, and *macro*- scales is a challenge for science and the imagination. The main focus of this dissertation is developing synthetic methodologies for constructing integrated photocathodes for light activating chemical transformations that include capturing, converting, and storing solar energy as fuel as well as exploring a new class of molecular catalysts for HER. Innovative synthetic methods support the development of new concepts and improve the understanding of fundamental aspects of structure-function relationships governing the use of extended aromaticity. Exploring the use of bimetallic architectures for solar fuel production advances knowledge of molecular catalysis in complex environments, further technological advancements, identifies novel applications, and inspires design of a new class of catalysts contributing to the field of chemical catalysis, interface chemistry, and solar fuels renewable energy science research.

1.7 References

(1) *IPCC* 5th Assessment Report, Geneva, Switzerland, **2014**.

(2) Faunce, T. A.; Lubitz, W.; Rutherford, A. W.; MacFarlane, D.; Moore, G. F.; Yang, P.; Nocera, D. G.; Moore, T. A.; Gregory, D. H.; Fukuzumi, S.; et al. Energy and Environment Policy Case for a Global Project on Artificial Photosynthesis. *Energy Environ. Sci.* **2013**, *6* (3), 695–698.

(3) Rockström, J.; Steffen, W.; Noone, K.; Persson A.; Chapin, F. S.; Lambin, E. F.; Lenton, T. M.; Scheffer, m.; Folke, C.; Schellnhuber, H. J.; Nykvist, B. A Safe Operating space for Humanity. *Nature* **2009**, *461*, 472–475.

(4) Steffen, W.; Richardson, K.; Rockström, J.; Cornell, S. E.; Fetzer, I.; Bennett, E. M.; Biggs, R.; Carpetner, S. R.; de Vries, W.; de Wit, C. A.; Folke, C.; Gerten, D.; Heinke, J.; Mace, G. M.; Persson, L. M.; Ramanathan, V.; Reyers, B.; Sörlin, S. Planetary Boundaries: Guiding Human Development on a Changing Planet. *Science* **2015**, *347* (6223), 736–746.

(5) Ardo, S.; Rivas, D. F.; Modestino, M. A.; Greiving, V. S.; Abdi, F. F.; Llado, E. A.; Artero, V.; Ayers, K.; Battaglia, C.; Becker, J-P.; et al. Pathways to Electrochemical Solar-Hudrogen Technologies. *Energy Environ. Sci.* **2018**, *11* (10), 2768–2783.

(6) Vesborg, P. C.; Jaramillo, T. F. Addressing the Terawatt Challenge: Scalability in the Supply of Chemical Elements for Renewable Energy. *RSC Adv.* **2012**, *2* (21), 7933−7947.

(7) The Role of the Chemical Sciences in Finding Alternatives to Critical Resources: A Workshop Summary. National Research Council. National Academies Press. **2012**.

(8) Auwärter, W.; Écija, D.; Klappenberger, F.; Barth, J. V. Porphyrins at Interface. *Nat. Chem.* **2015**, *7*, 105−120.

(9) Morris, A. J.; Meyer, G. J.; Fujita, E. Molecular Approach to the Photocatalytic reduction of Carbon Dioxide for Solar Fuels. *Acc. Chem. Res*. **2009**, *42* (12), 1983−1994.

(10) Lin, S.; Diercks, C. S.; Zhang, Y.-B.; Kornienko, N.; Nichols, E. M.; Zhao, Y.; Paris, A. R.; Kim, D.; Yang, P.; Yaghi, O. M.; Chang, C. J. Covalent Organic Frameworks Comprising Cobalt Porphyrins for Catalytic CO_2 Reduction in Water. *Science* **2015**, *349* (6253), 1208−1213.

(11) Rigsby, M. L.; Wasylenko, D. J.; Pegis, M. L.; Mayer, J. M. Medium Effect Are as Important as Catalyst Design for Selectivity in Electrocatalytic Oxygen reduction by Iron-Porphyrin Complexes. *J. Am. Chem. Soc*. **2015**, *137* (13), 4296−4299.

(12) Swierk, J. R.; Méndez- Hernández, D. D.; McCool, N. S.; Liddell, P.; Terazono, Y.; Pahk, I.; Tomlin, J. J.; Oster, N. V.; Moore, T. A.; Moore, A. L.; Gust, D.; Mallouk, T. E. Metal-Free Organic Sensitizers for Use in Water-Splitting Dye-Sensitized Photoelectrochemical Cells. *Proc. Natl. Acad. Sci. U. S. A.* **2015**, *112* (6), 1681−1686.

(13) Costentin, C.; Robert, M.; Savéant, J.-M. Current Issues in Molecular Catalysis Illustrated by Iron Porphyrins as Catalysts of the CO_2-to-CO Electrochemical Conversion. *Acc. Chem. Res.* **2015**, *48* (12), 2996−3006.

(14) Ahrenholtz, S. R.; Epley, C. C.; Morris, A. J. Solvothermal Preparation of an Electrocatalytic Metalloporphyrin MOF Thin Film and its Redox Hopping Charge-Transfer Mechanism. *J. Am. Chem. Soc.* **2014**, *136* (6), 2464−2472.

(15) Yao, S. A.; Ruther, R. E.; Zhang, L.; Franking, R. A.; Hamers, R. J.; Berry, J. F. Covalent Attachment of Catalyst Molecules to Conductive Diamond: CO2 Reduction Using "Smart" Electrodes. *J. Am. Chem. Soc.*, **2012**, *134* (38) 15632−15635.

(16) Lindsey, J. S.; Bocian, D. F. Molecules for Charge-Based Information Storage. *Acc. Chem. Res.*, **2011**, *44* (8) 638−650.

(17) Civic, M. R.; Dinolfo, P. H. Electrochemical Rectification of Redox Mediators Using Porphyrin-Based Molecular multilayered Films on ITO electrodes. *ACS Appl. Mater. Interfaces* **2016**, *8* (31), 20465−20473.

(18) *Basic Research Needs for Catalysis Science to Transform Energy Technologies*, U.S. Department of Energy: Basic Energy Science Workshop Report; U.S. Government Printing Office: Washington, DC, 2017.

(19) Grunes, J.; Zhu, J.; Somorjai, G. A. Catalysis and Nonoscience. *Chem. Commun*. **2003**, *18*, 2257−2260.

(20) Kamat, P. V.; Tvrdy, K.; Baker, D. R.; Radich, J. G. Beyond Photovoltaics: Semiconductor Nanoarchitectures for Liquid-Junction Solar Cells. *Chem. Rev.* **2010**, *110* (11), 6664–6688.

(21) Nocera, D. G. Solar Fuels and Solar Chemicals Industry. *Acc. Chem. Res.* **2017**, *50* (3), 616–619.

(22) Hambourger, M.; Moore, G. F.; Kramer, D. M.; Gust, D.; Moore, A. L.; Moore, T. A. Biology and Technology for Photochemical Fuel Production. *Chem. Soc. Rev.* **2009**, *38* (1), 25–35.

(23) Moore, G. F.; Brudvig, G. W. Energy Conversion in Photosynthesis: A Paradigm for Solar Fuel Production. *Annu. Rev. Condens. Matter Phys.* **2011**, *2* (1), 303–327.

(24) Benson, E. E.; Kubiak, C. P.; Sathrum, A. J.; Smeieja, J. M. Electrocatalytic and Homogeneous Approaches to Conversion of CO_2 to Liquid Fuels. *Chem. Soc. Rev.* **2009**, *38* (1), 89–99.

(25) Kumar, B.; Llorente, M.; Froehlich, J.; Dang, T.; Sathrum, A.; Kubiak, C. P. Photochemical and Photoelectrochemical Reduction of CO_2. *Annu. Rev. Phys. Chem.* **2012**, *63*, 541–569.

(26) Ye, R.; Zhao, J.; Wickemeyer, B. B.; Toste, F. D.; Somorjai, G. A. Foundations and Strategies of the Construction of Hybrid Catalysts for Optimized Performance. *Nat. Catal.* **2018**, *1* (5), 318–325.

(27) Wang, M.; Yang, Y.; Shen, J.; Jiang, J.; Sun, L. Visible-Light-Absorbing Semiconductor/Molecular Catalyst Hybrid Photoelectrodes for H_2 or O_2 Evolution: Recent Advances and Challenges. *Sustain. Energy Fuels* **2017**, *1* (8), 1641–1663.

(28) Queyriaux, N.; Kaeffer, N.; Morozan, A.; Chavarot-Kerlidou, M.; Artero, V. Molecular Cathode and Photocathode Materials for Hydrogen Evolution in Photoelectrochemical Devices. *J. Photochem. Photobiol. C Photochem. Rev.* **2015**, *25*, 90–105.

(29) Wen, F.; Li, C. Hybrid Artificial Photosynthetic Systems Comprising Semiconductors as Light Harvesting and Biomimetic Complexes as Molecular Cocatalysts. *Acc. Chem. Res.* **2013**, *46* (11), 2355–2364.

(30) Bullock, R. M.; Das, A. K.; Appel, A. M. Surface Immobilization of Molecular Electrocatalysts for Energy Conversion. *Chem. - A Eur. J.* **2017**, *23* (32), 7626–7641.

(31) Jiao, J.; Yu, M.; Holten, D.; Lindsey, J. S.; Bocian, D. F. Characterization of Hydroporphyrins Covalently Attached to Si(100). *J. Porphyrins and Phthalocyanines* **2017**, *21*, 453–464.

(32) McKone, J. R.; Marinescu, S. C.; Brunschwig, B. S.; Winkler, J. R.; Gray, H. B. Earth-Abundant Hydrogen Evolution Electrocatalysts. *Chem. Sci.* **2014**, *5*, 865–878.

(33) Mizuno, N.; Misono, M. Heterogeneous Catalysis. *Chem. Rev.* **1998**, *98* (1), 199–218.

(34) Armstrong, F. A.; Hirst, J. Reversibility and Efficiency in Electrocatalytic Energy Conversion and Lessons From Enzymes. *Proc. Natl. Acad. Sci. U. S. A.* **2011**, *108* (34), 14049–14054.

(35) Rakowski DuBois, M.; Dubois, D. L. The Role of the First and Second Coordination Spheres in the Design of Molecular Catalysts for H_2 Production and Oxidation. *Chem. Soc. Rev.* **2009**, 38, 62–72.

(36) Cracknell, J. A.; Vincent, K. A.; Armstrong, F. A. Enzymes as Working or Inspirational Electrocatalysts for Fuel Cells and Electrolysis. *Chem. Rev.* **2008**, *108* (7), 2439–2461.

(37) Helm, M. L.; Stewart, M. P.; Bullock, R. M.; DuBois, M. R.; DuBois, D. L. A Synthetic Nickel Electrocatalyst with a Turnover Frequency Above 100,000 s^{-1} for H_2 Production. *Science* **2011**, *333* (6044), 863–866.

(38) Ginovska-Pangovska, B.; Dutta, A.; Reback, M. L.; Linehan, J. C.; Shaw, W. J. Beyond the Active Site: The Impact of the Outer Coordination Sphere on Electrocatalysts for Hydrogen Production and Oxidation. *Acc. Chem. Res.* **2014**, *47* (8), 2621–2630.

(39) Bacchi, M.; Berggren, G.; Niklas, J.; Veinberg, E.; Mara, M. W.; Shelby, M. L.; Poluektov, O. G.; Chen, L. X.; Tiede, D. M.; Cavazza, C.; Field, M. J.; Fontecave, M.; Artero, V. Cobaloxime-Based Artificial Hydrogenases. *Inorg. Chem.* **2014**, *53* (15), 8071–8082.

(40) Dutta, A.; Ginovska, B.; Raugei, S.; Roberts, J. A.; Shaw, W. J. Optimizing Conditions for Utilization of an H_2 Oxidation Catalyst with Outer Coordination Sphere Functionalities. *Dalton Trans.* **2016**, *45*, 9786–9793.

(41) Wiese, S.; Kilgore, U. J.; Ho, M.-H.; Raugei, S.; DuBois, D. L.; Bullock, R. M.; Helm, M. L. Hydrogen Production Using Nickel Electrocatalysts with Pendant Amines: Ligand Effects on Rates and Overpotentials. *ACS Catal.* **2013**, *3* (11), 2527–2535.

(42) Tsay, C.; Yang, J. Y. Electrocatalytic Hydrogen Evolution Under Acidic Aqueous Conditions and Mechanistic Studies of a Highly Stable molecular Catalyst. *J. Am. Chem. Soc.* **2016**, *138* (43), 14174–14177.

(43) Maher, A. G.; Passard, G.; Dogutan, D. K.; Halbach, R. L.; Anderson, B. L.; Gagliardi, C. J.; Taniguchi, M.; Lindsey, J. S.; Nocera, D. G. Hydrogen Evolution Catalysis by a Sparsely Substituted Cobalt Chlorin. *ACS Catal.* **2017**, *7* (5), 3597–3606.

(44) McCrory, C. C. L.; Uyeda, C.; Peters, J. C. Electrocatalytic Hydrogen Evolution in Acidic Water with Molecular Cobalt Tetraazamacrocycles. *J. Am. Chem. Soc.* **2012**, *134* (6), 3164–3170.

(45) Du, P.; Eisenberg, R. Catalysts Made of Earth-abundant Elements (Co, Ni, Fe) for Water Splitting: Recent Progress and Future Challenges. *Energy Environ. Sci.* ***2012***, *5* (3), 6012–6021.

(46) Karunadasa, H. I.; Chang, C. J.; Long, J. R. A Molecular Molybdenum-oxo Catalyst for Generation Hydrogen from Water. *Nature* **2010**, *464*, 1329–1333.

(47) Artero, V.; Savéant, J.-M. Toward the Rational Benchmarking of Homogeneous H_2- evolving Catalysts. *Energy Environ. Sci.* **2014**, *7* (11), 3808–3814.

(48) Kellet, R. M.; Spiro, T. G. Cobalt(I) Porphyrin Catalysis of Hydrogen Production from Water. *Inorg. Chem.* **1985**, *24* (15), 2373–2377.

(49) Behar, D.; Dhanasekaran, T.; Neta, P.; Hosten, C. M.; Ejeh, D.; Hambright, P.; Fujita, E. Cobalt Porphyrin Catalyzed Reduction of CO2. Radiation Chemical, Photochemical, and Electrochemical Studies. *J. Phys. Chem. A* **1998**, *102* (17), 2870–2877.

(50) Bhugun, I.; Lexa, D.; Savéant, J.-M. Homogeneous Catalysis of Electrochemical Hydrogen Evolution by Iron(0) Porphyrins. *J. Am. Chem. Soc.* **1996**, *118* (16), 3982–3983.

(51) Tsuda, A.; Osuka, A. A Fully Conjugated Porphyrin Tapes with Electronic Absorption Bands that Reach into Infrared. *Science* **2001**, *293* (5527), 79–82.

(52) Tsuda, A.; Furuta, H; Osuka, A. Syntheses, Structural Characterizations, and Optical and Electrochemical Properties of Directly Fused Diporphyrins. *J. Am. Chem. Soc.* **2001**, *123* (42), 10304−10321.

(53) Kim, D.; Osuka, A. Photophysical Properties of Directly Linked Linear Porphyrin Arrays. *J. Phys. Chem. A* **2003**, *107* (42), 8791−8816.

(54) Cheng, F.; Zhang, S.; Adronov, A.; Echegoyen, L.; Diederich, F. Triply Fused ZnII–Porphyrin Oligomers: Synthesis, Properties, and Supramolecular Interactions with Single-Walled Carbon Nanotubes (SWNTs). *Chem. - Eur. J.* **2006**, *12* (23), 6062−6070.

(55) Brennan, B. J.; Arero, J.; Liddell, P. A.; Moore, T. A.; Moore, A. L.; Gust, D. Selective Oxidative Synthesis of Meso-Beta Fused Porphyrin Dimers. *J. Porphyrins Phthalocyanines* **2013**, *17* (4), 247−251.

(56) Lin, S. Y.; DiMagno S. G.; Therien M. J. Highly Conjugated, Acetylenyl Bridged Porphyrins: New Models for Light-Harvesting Antenna Systems. *Science* **1994**, *264* (5162), 1105−1111.

(57) Anderson H. L. Building Molecular Wires from the Colours of Life: Conjugated Porphyrin Oligomers. *Chem. Commun*. **1999**, *23*, 2323−2330.

(58) Costentin, C.; Savéant, J. M. Towards an Intelligent Design of Molecular Electrocatalysts. *Nat. Rev. Chem.* **2017**, *1*, 0087.

(59) Pegis, M. L.; McKeown, B. A.; Kumar, N.; Lang, K.; Wasylenko, D. J.; Zhang, X. P.; Raugei, S.; Mayer, J. M. Homogeneous Electrocatalytic Oxygen Reduction Rates Correlate with Reaction Overpotential in Acidic Organic Solutions. *ACS Cent. Sci*. **2016**, *2* (11), 850−856.

(60) Bard, A.; Fox, M. A. Artificial Photosynthesis: Solar Splitting of Water to Hydrogen and Oxygen. *Acc. Chem. Res.* **1995**, *28* (3), 141–145.

(61) Blankenship, R. E.; Tiede, D. M.; Barber, J.; Brudvig, G. W.; Fleming, G.; Ghirardi, M.; Gunner, M. R.; Junge, W.; Kramer, D. M.; Melis, A.; et al. Comparing Photosynthetic and Photovoltaic Efficiencies and Recognizing the Potential for Improvement. *Science* **2011**, *332* (6031), 805–809.

(62) Tran, P. D.; Wong, L. H.; Barber, J.; Loo, J. S. C. Recent Advances in Hybrid Photocatalysts for Solar Fuel Production. *Energy Environ. Soc. Rev.* **2012**, *5* (3), 5902–5918.

(63) Swierk, J. R.; Mallouk, T. E. Design Development of Photoanodes for Water- splitting Dye-sensitized Photoelectrochemical Cells. *Chem. Soc. Rev.* **2013**, *42* (6), 2357–2387.

(64) Walter, M. G.; Warren, E. L.; McKone, J. R.; Boettcher, S. W.; Mi, Q.; Santori, E. a.; Lewis, N. S. Solar Water Splitting Cells. *Chem. Rev.* **2010**, *110* (11), 6446–6473.

(65) Downes, C. A.; Marinescu, S. C. Efficient Electrochemical and Photoelectrochemical H $_2$ Production from Water by a Cobalt Dithiolene One-Dimensional Metal–Organic Surface. *J. Am. Chem. Soc.* **2015**, jacs.5b07020.

(66) Krawicz, A.; Yang, J.; Anzenberg, E.; Yano, J.; Sharp, I. D.; Moore, G. F. Photofunctional Construct That Interfaces Molecular Cobalt-Based Catalysts for H2 Production to a Visible-Light-Absorbing Semiconductor. *J. Am. Chem. Soc.* **2013**, *135*, 11861–11868.

(67) Cedeno, D.; Krawicz, A.; Doak, P. Using Molecular Design to Control the Performance of Hydrogen-Producing Polymer-Brush-Modified Photocathodes. *J. Phys. Chem. Lett.* **2014**, *5* (18), 3222–3226.

(68) Kim, H. J.; Seo, J.; Rose, M. J. H_2 Photogeneration Using a Phosphonate-anchored Ni-PNP Catalyst on a Band-edge-modified p-Si(111)IAZO Construct. *ACS Appl. Mater. Interfaces*, **2016**, *8* (2), 1061–1066.

(69) Gu, J.; Yan, Y.; Young, J. L.; Steirer, K. X.; Neale, N. R.; Turner, J. A. Water Reduction by a P-$GaInP_2$ Photoelectrode Stabilized by an Amorphous TiO_2 Coating and a Molecular Cobalt Catalyst. *Nat. Mater.* **2016**, *15* (4), 456–460.

(70) Beiler, A. M.; Khusnutdinova, D.; Jacob, S. I.; Moore, G. F. Chemistry at the Interface: Polymer-Functionalized GaP Semiconductors for Solar Hydrogen Production. *Ind. Eng. Chem. Res.* **2016**, *55* (18), 5306–5314.

(71) Beiler, A. M.; Khusnutdinova, D.; Jacob, S. I.; Moore, G. F. Solar Hydrogen Production Using Molecular Catalysts Immobilized on Gallium Phosphide (111)A and (111)B Polymer-Modified Photocathodes. *ACS Appl. Mater. Interfaces* **2016**, *8* (15), 10038–10047.

(72) Kellett, R. M.; Spiro, T. G. Cobalt Porphyrin Electrode Films as H_2 Evolution Catalysts. *Inorg. Chem.* **1985**, *24* (15), 2378–2382.

(73) Maurin, A.; Robert, M. Noncovalent Immobilization of a Molecular Iron-based Electrocatalyst on Carbon Electrodes for Selective, Efficient CO_2-to-CO Conversion in Water. *J. Am. Chem. Soc.* **2016**, *138* (8), 2492–2495.

(74) Maurin, A.; Robert, M. Catalytic CO2-to-CO Conversion in Water by Covalently Functionalized Carbon Nanotubes with a Molecular Iron Catalyst. *Chem.Commun*. **2016**, *52* (81), 12084–12087.

(75) Weng, Z.; Jiang, J.; Wu, Y.; Wu, Z.; Guo, X.; Materna, K. L.; Liu, W.; Batista, V. S.; Brudvig, G. W.; Wang, H. Electrochemical CO_2 Reduction to Hydrocarbons on a Heterogeneous molecular Cu Catalyst in Aqueous Solution. *J. Am. Chem. Soc.* **2016**, *138* (26), 8076–8079.

(76) Beiler, A. M.; Khusnutdinova, D.; Wadsworth, B. L.; Moore, G. F. Cobalt Porphyrin-Polypyridyl Surface Coatings for Photoelectrosynthetic Hydrogen Production. *Inorg. Chem.* **2017**, *56* (20), 12178–12185.

(77) Rosenthal, J.; Luckett, T. D.; Hodgkiss, J. M.; Nocera, D. G. Photocatalytic Oxidation of Hydrocarbons by a Bis-iron(III)-μ-oxo Pacman Porphyrin Using O_2 and Visible Light. *J. Am. Chem. Soc.* **2006**, *128* (20), 6546–6547.

(78) Berben, L. A.; Peters, J. C. Hydrogen Evolution by Cobalt Tetraimine Catalysts Adsorbed on Electrode Surfaces. *Chem. Commun.* **2010**, *46* (3), 398–400.

(79) Rose, M. J.; Gray, H. B.; Winkler, J. R. Hydrogen Generation Catalyzed by Fluorinated Diglyoxime-iron Complexes at Low Overpotentials. *J. Am. Chem. Soc.* **2012**, *134* (20), 8310–8313.

(80) Dhanasekaran, T.; Grodkowski, J.; Neta, P.; Hambright, P.; Fujita, E. p-Terphenyl-sensitized Photoreduction of CO_2 with Cobalt and Iron Porphyrins. Interaction between CO and Reduced Metalloporphyrins. *J. Phys. Chem. A*, **1999**, *103* (38), 7742–7748.

(81) Gooding, J. J.; Ciampi, S. The Molecular Level Modification of Surfaces: from Self-assembled Monolayers to Complex Molecular Assemblies. *Chem. Soc. Rev*. **2011**, *40* (5), 2704–2718.

(82) Vilan, A.; Cahen, D. Chemical Modification of Semiconductor Surfaces for Molecular Electronic. *Chem. Rev*. **2017**, *117* (5), 4624–4666.

(83) Forbes, M. D. E. What We Talk About When We Talk About Light. *ACS Cent. Sci.* **2015**, *1* (7), 354–363.

CHAPTER 2 COBALT AND IRON PORPHYRIN-MODIFIED GALLIUM PHOSPHIDE SURFACES FOR SOLAR HYDROGEN PRODUCTION

Portions of this work are excerpted with permission from:

Khusnutdinova, D.; Beiler, A. M.; Wadsworth B. L.; Jacob S. I.; Moore G. F. *Chem. Sci.* **2017**, *8* (1), 253–259.

Reproduced from Ref. 119 with permission from the Royal Society of Chemistry.

2.1 Introduction

Heterogeneous systems based on cobalt or iron porphyrin molecular catalysts immobilized onto a surface of gallium phosphide with a high activity for photoelectrosynthetic hydrogen production in aqueous conditions are described in this chapter. A direct one-step method to chemically graft metalloporphyrins to a visible-light-absorbing semiconductor is presented with the aim of constructing an integrated photocathode for light activating chemical transformations that include capturing, converting, and storing solar energy as fuels. Structural characterization of the hybrid assemblies is achieved using surface-sensitive spectroscopic methods, and functional performance for photoinduced hydrogen production is demonstrated via three-electrode electrochemical testing combined with product analysis using gas chromatography. Measurements of the total per geometric area porphyrin surface loadings using a cobalt-porphyrin-based assembly indicate a turnover frequency of 3.9 H_2 molecules $site^{-1}$ s^{-1}, representing one of the highest activities for a molecular-catalyst-modified semiconductor photoelectrode operating at the H^+/H_2 equilibrium potential under 1-sun illumination.

Cobalt and iron porphyrin complexes are chemically grafted onto p-type GaP(100), a midsize optical band gap semiconductor that has shown promise in light-emitting-diode technologies and in applications for solar energy transduction as a light capture and conversion component (Figure 2.1).[1-8] Metalloporphyrin analogs are prepared via a novel synthetic strategy to yield a macrocycle with a pendent 4-vinylphenyl surface attachment group at the β-position of the porphyrin ring structure. This modification allows use of the UV-induced immobilization chemistry of olefins[9-14] to attach intact metalloporphyrin complexes to the semiconductor surface. While the mechanistic details of the vinyl group

attachment chemistry are not settled, molecular binding appears to occur over bridging oxygen atoms on GaP surfaces.[10,15,16]

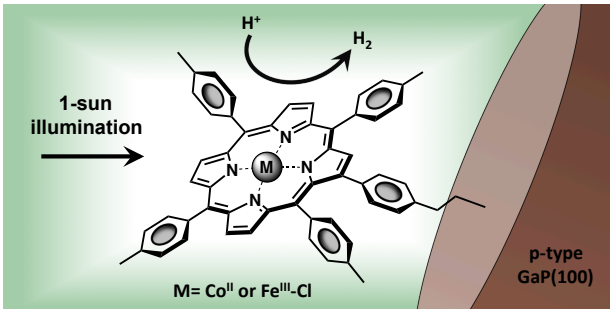

Figure 2.1. Schematic representation of chemically modified cobalt or iron porphyrin complexes directly attached to the GaP surface for photoelectrosynthetic hydrogen production.

2.2 Results and Discussion

2.2.1 Materials Preparation

Molecular precursors

Synthesis of the 4-vinylphenyl functionalized metalloporphyrin precursors, cobalt(II) 5,10,15,20-tetra-*p*-tolyl-2-(4-vinylphenyl)porphyrin (1), iron(III) 5,10,15,20-tetra-*p*-tolyl-2-(4-vinylphenyl)porphyrin chloride (2), as well as model compounds, metalloporphyrins without a surface attachment group, cobalt(II) 5,10,15,20-tetra-*p*-tolylporphyrin (3), iron(III) 5,10,15,20-tetra-*p*-tolylporphyrin chloride (4), and a free-base porphyrin, 5,10,15,20-tetra-*p*-tolyl-2-(4-vinylphenyl)porphyrin (5) is described in detail in Chapter 6.

Surface modification

Preparation of the GaP substrates for subsequent photochemical functionalization using the structurally modified porphyrins begins with buffered hydrofluoric acid treatment to

remove the bulk surface oxide layers. First, diced semiconductor samples were degreased by wiping the surface with an acetone-soaked cotton swab and ultrasonically cleaning in acetone and isopropanol for 5 min each, followed by drying under nitrogen. Samples were then exposed to an air-generated oxygen plasma (Harrick Plasma, U.S.) at 30 W for 2 min. Surface oxide layers were then removed by immersion of the plasma-treated samples in buffered hydrofluoric acid (6:1 HF/NH_4F in H_2O) for 5 min, followed by rinsing with Milli-Q water. The freshly etched wafers are placed into a sealed quartz flask containing an argon-sparged solution of the appropiate porphyrin precursor (1 mM) and illuminated with shortwave UV-light (254 nm) for 2 h (Figure 2.2). The porphyrin-functionalized wafers are then removed from the flask, ultrasonically cleaned, and dried under nitrogen. Prepared constructs are CoP|GaP and FeP|GaP formed using 1 and 2, respectively.

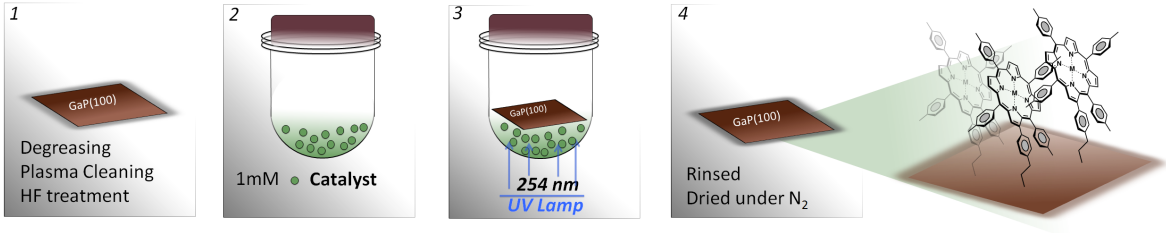

Figure 2.2. Schematic representation of the attachment strategy used to assemble metalloporphyrin modified gallium phosphide wafers (see main text for further details).

Electrode Fabrication

GaP working electrodes were fabricated by applying an indium-gallium eutectic (Aldrich) to the backside of a wafer, then fixing a copper wire to the back of the wafer using a conductive silver epoxy (Circuit Works). The copper wire was passed through a

glass tube, and the wafer was insulated and attached to the glass tube with Loctite 615 Hysol Epoxi-patch adhesive. The epoxy was allowed to fully cure before testing the electrodes.

2.2.2 Surface Characterization via GATR-FTIR and XP Spectroscopies

Chemically modified and unmodified surfaces of the samples were characterized via grazing angle total reflectance Fourier transform infrared (GATR-FTIR) spectroscopy. Absorption spectra of unmodified GaP(100) substrates following acid treatment are characterized by significant residual surface oxygen coverage, and static water contact angles of <10° indicate a dominant coverage by hydrophilic hydroxyl groups (Figure 2.3).

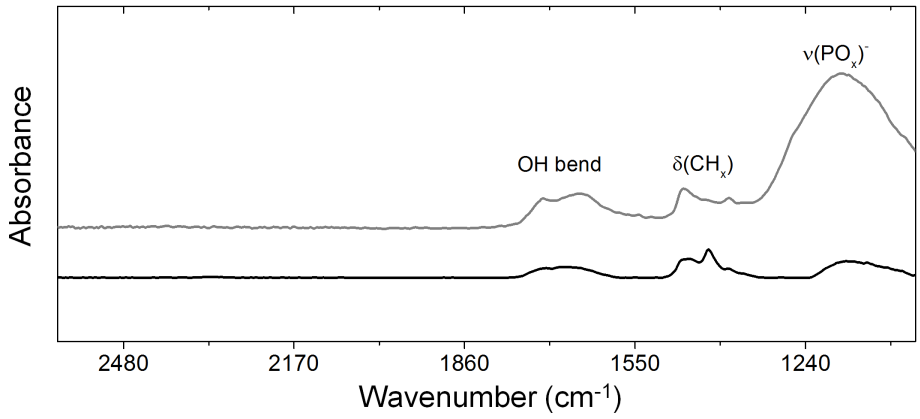

Figure 2.3. GATR-FTIR absorption spectra of unmodified GaP(100) before (gray) and after (black) etching with HF solution (6:1 HF/NH_4F in H_2O).

However, GATR-FTIR absorption spectra collected using samples following cobalt or iron porphyrin functionalization, 1 or 2, yielding CoP|GaP or FeP|GaP, respectively, are characterized by unique vibrational features corresponding to C=C bond ring modes of the porphyrin, appearing at 1607 cm^{-1}, as well as transitions that are assigned to the C_β-H,

C_α-N, and C_β-C_β vibrations of the macrocycle (Figure 2.4). The porphyrin related absorbance bands observed on the metalloporphyrin-modified GaP surfaces are consistent with previous literature reports regarding the peak positions of analogous non-surface immobilized porphyrins.[17-19]

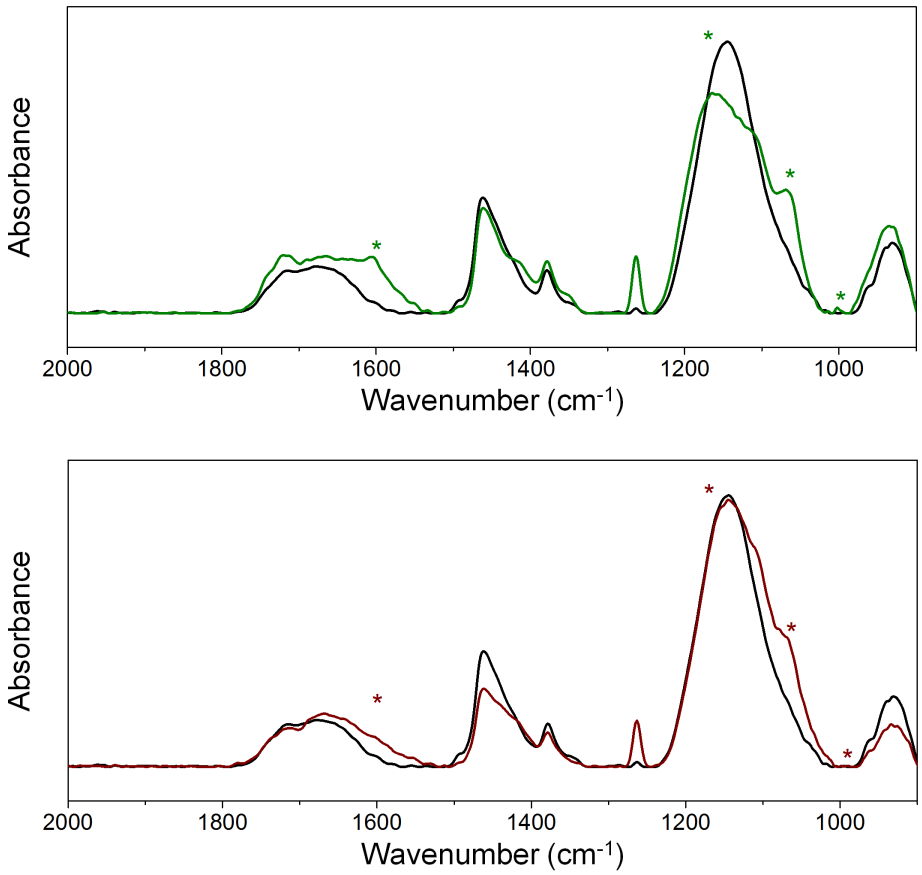

Figure 2.4. GATR-FTIR absorption spectra of CoP|GaP (green), FeP|GaP (dark red), and unmodified GaP (black).

FTIR transmission spectra of the cobalt and iron porphyrin precursors (i.e. prior to their surface immobilization), show similar C=C bond ring modes centered at 1607 cm^{-1}, but also include an additional pronounced peak centered at 1626 cm^{-1} associated with the

vinyl C=C bond (Figure 2.5). The lack of this pronounced feature at 1626 cm^{-1} in absorption spectra of the metalloporphyrin-modified GaP samples indicates undetectable to no vinyl functionality on the surfaces, consistent with the proposed mechanism of the vinyl group grafting chemistry on hydroxyl and oxygen-terminated surfaces.[15, 16, 9-11]

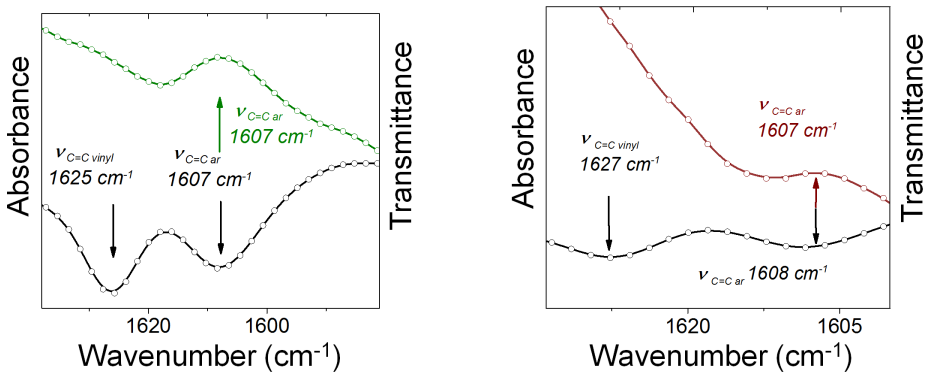

Figure 2.5. (left) GATR-FTIR absorption spectrum of CoP|GaP (green) and FTIR transmission spectrum of the cobalt porphyrin precursor, cobalt(II) 5,10,15,20-tetra-*p*-tolyl-2-(4-vinylphenyl)porphyrin (black) in KBr. (right) GATR-FTIR absorption spectrum of FeP|GaP (dark red) and FTIR transmission spectrum of the iron porphyrin precursor, iron(III) 5,10,15,20-tetra-*p*-tolyl-2-(4-vinylphenyl)porphyrin (black) in KBr.

Further, the vibrational frequencies associated with an in-plane metalloporphyrin deformation $\nu_{Co\text{-}N}$ and $\nu_{Fe\text{-}N}$ (where ν is the vibrational frequency) observed on the surfaces of the CoP|GaP or FeP|GaP (1001 cm^{-1} and 997 cm^{-1}, respectively) provide compelling evidence that the porphyrin metal centers remain intact following the grafting procedure (Figure 2.6). In contrast, the value of the in-plane porphyrin deformation mode, $\nu_{N\text{-}H}$, of analogous free-base porphyrins, 5, occurs at 966 cm^{-1} (Figure 2.7). The similarity in values of in-plane metalloporphyrin deformation modes observed on the

metalloporphyrin-functionalized GaP surfaces with those observed in spectra of analogous non-surface-attached metalloporphyrins indicates the porphyrin metal centers maintain a similar vibrational environment following immobilization. Lastly, spectra of control samples, in which metalloporphyrins without the vinyl group functionality, 3 and 4, are used during the photochemical grafting step, show no evidence of porphyrin complexes at the GaP surface.

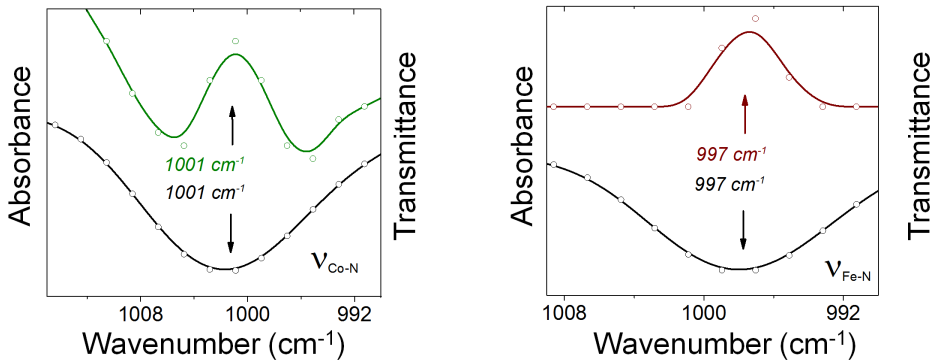

Figure 2.6. (left) GATR-FTIR absorption spectrum showing the $\nu_{Co–N}$, at the surface of CoP|GaP (green) and FTIR transmission spectrum showing the $\nu_{Co–N}$ of the non-surface attached cobalt porphyrin (black) in KBr. (right) GATR-FTIR absorption spectrum showing the $\nu_{Fe–N}$ at the surface of FeP|GaP (dark red) and FTIR transmission spectrum showing the $\nu_{Fe–N}$ of the non-surface-attached iron porphyrin (black) in KBr.

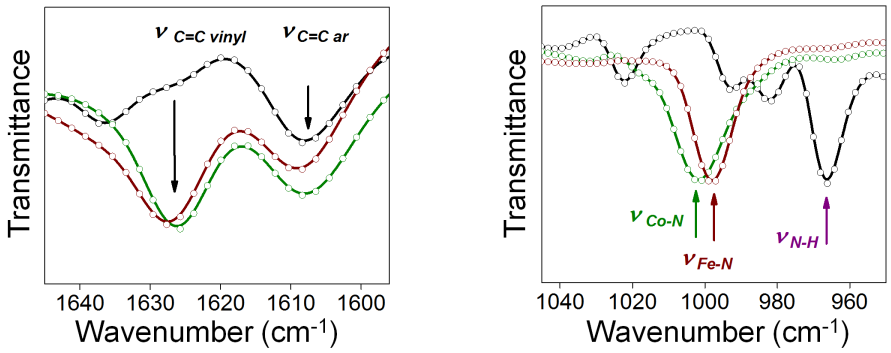

Figure 2.7. FTIR transmission spectra of 5,10,15,20-tetra-*p*-tolylporphyrin (black), cobalt(II) 5,10,15,20-tetra-*p*-tolyl-2-(4-vinylphenyl)porphyrin (green), and iron(III) 5,10,15,20-tetra-*p*-tolyl-2-(4-vinylphenyl)porphyrin chloride (dark red) in KBr.

X-ray photoelectron (XP) spectroscopy provides additional characterization and evidence of successful functionalization. As compared to spectra obtained using unmodified GaP samples, survey XP spectra of CoP|GaP surfaces show the presence of additional N, Co, and C elements associated with attached cobalt porphyrins, and spectra of FeP|GaP surfaces show the presence of additional N, Fe, and C elements associated with attached iron porphyrins (Figure 2.8). In addition, the high-energy resolution Co 2p core level spectrum of the CoP|GaP samples shows peaks centered at 780.9 eV ($2p_{3/2}$) and 796.7 eV ($2p_{1/2}$) with a 2:1 branching ratio (Figure 2.9). The Co $2p_{3/2}$ signal indicates a complex multiplet structure, consistent with the oxidation state +2 and the open-shell (d^7) character of the Co ion.[20,21] For the FeP|GaP substrates, Fe 2p core level spectra contain features characteristic of Fe^{III} porphyrins, including peaks centered at 710.8 eV ($2p_{3/2}$) and 724.1 eV ($2p_{1/2}$) (Figure 2.9).[22] Lastly, analysis of the Co 2p and N 1s spectral intensity ratios of CoP|GaP spectra as well as the Fe 2p and N 1s spectral intensity ratios of FeP|GaP spectra yields metal : nitrogen ratios of 1:4 for both constructs, indicating no

detectable loss of Co or Fe from the attached porphyrin units following UV-induced grafting.

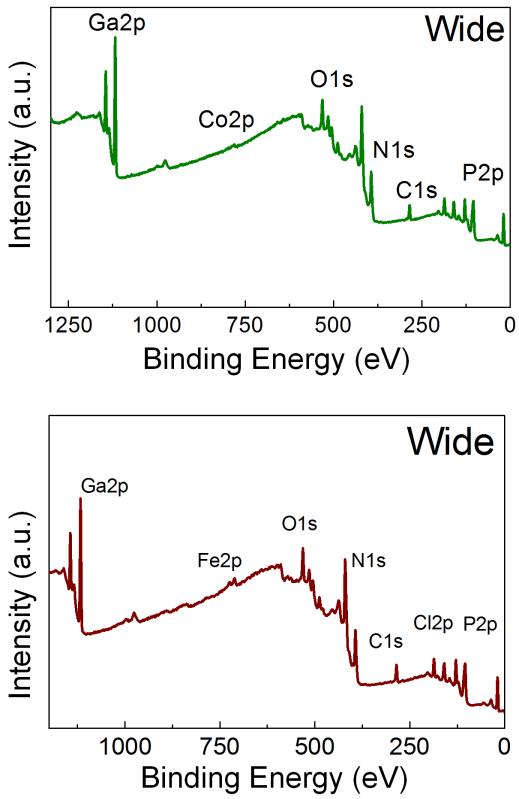

Figure 2.8. XP survey spectra of CoP|GaP (green) and FeP|GaP (dark red).

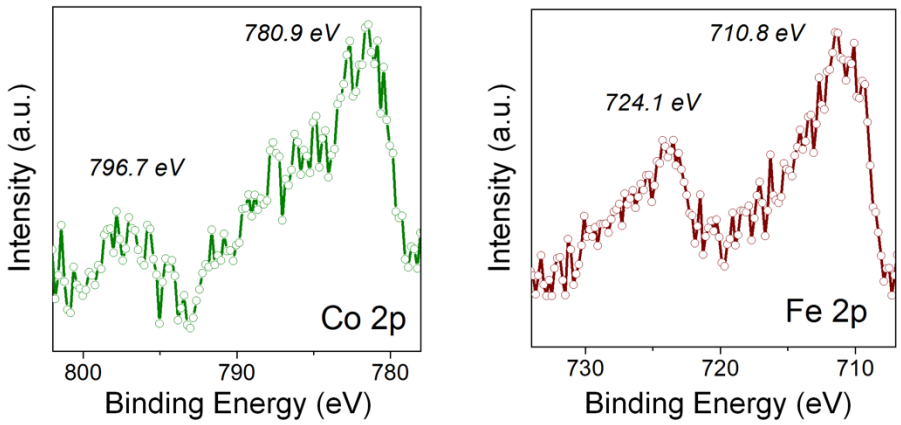

Figure 2.9. Co 2p core level XP spectrum of CoP|GaP (green) and Fe 2p (dark red) core level XP spectrum of FeP|GaP.

2.2.3 Photoelectrochemical Measurements

Catalytic activity of the resulted photoelectrodes was performed via photoelectrochemical (PEC) studies in a three-electrode configuration cell under 1-sun illumination in aqueous solutions. Illumination of CoP|GaP electrodes polarized at 0 V vs RHE in pH neutral aqueous solutions results in hydrogen generation at an initial rate of ~ 10 μL min^{-1} cm^{-2}. This rate of hydrogen evolution exhibits less than 10% loss of activity over 4 h of PEC measurement. By contrast, the iron-based constructs, FeP|GaP, show significant diminution of performance during PEC testing, including a rapid loss in current density following illumination during bulk-electrolysis measurements (Figure 2.10). Further, the relatively stable photocurrent densities that are measured after the drop off are similar in value to those initially achieved using unmodified GaP electrodes polarized at the same potential (0 V vs RHE) (Figure 2.11).

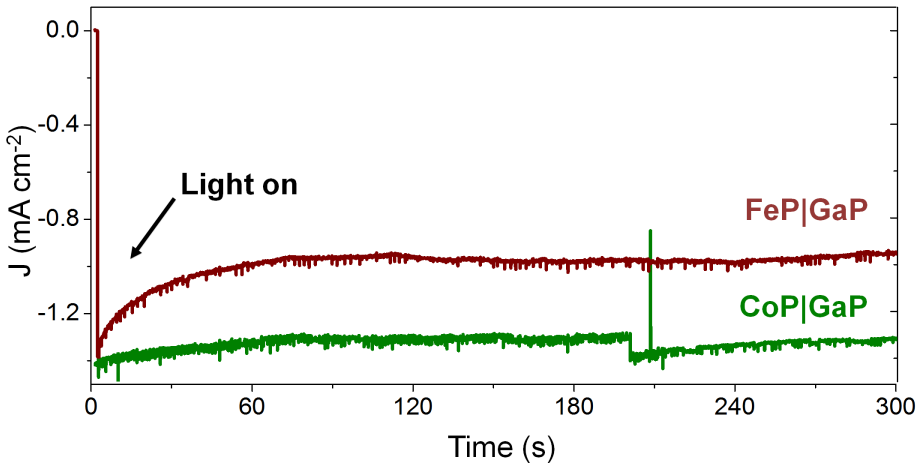

Figure 2.10. Chronoamperograms using CoP|GaP (green) or FeP|GaP (dark red) working electrodes polarized at a constant potential of 0 V vs RHE and under 1-sun illumination (100 mW cm^{-2}).

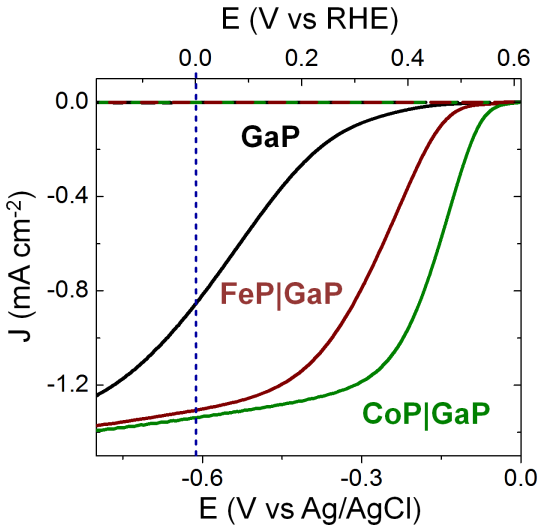

Figure 2.11. Linear sweep voltammograms recorded in the dark (dashed) or under 1-sun illumination (solid) using unmodified GaP(100) (black), CoP|GaP (green), or FeP|GaP (dark red) working electrodes collected in a three-electrode electrochemical cell in phosphate buffer (pH 7).

Thus, there is a nearly complete loss of the photocurrent gains afforded by the iron porphyrin, 2, functionalization. Although the iron porphyrins are notorious for their relative instability and propensity to form μ-oxo dimers,[23-27] a detailed analysis of the photocurrent degradation pathways regarding the FeP|GaP constructs is currently unavailable. These results do, however, illustrate the synthetic versatility of the porphyrin architecture, including selection of the catalytic metal site for controlling activity, and presence of ligand auxiliaries for tailoring their molecular structure as well as associated electronic properties. During PEC testing, the formation of gas bubbles at the surface of the porphyrin-modified electrode are transiently observed in linear sweep voltammetry experiments, when the electrodes are polarized at potentials generating cathodic currents, and continuously observed during bulk photoelectrolysis experiments (Figure 2.12).

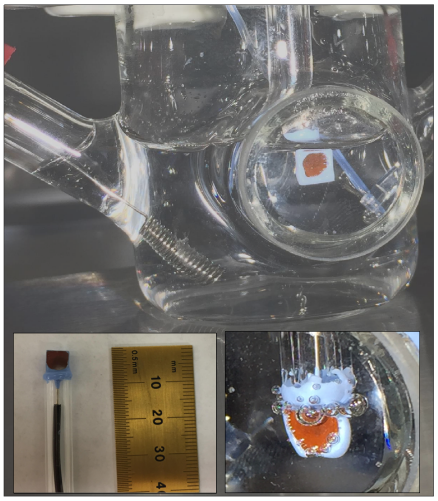

Figure 2.12. A photograph of a CoP|GaP photocathode (insert) under photoelectrochemical testing.

Gas chromatography analysis of the photoproducts confirms the production of hydrogen with near-unity Faradaic efficiency (measured at ~97% following 30 min of illumination) when using CoP|GaP working electrodes (Figure 2.13). These results confirm that no measurable hydrogen is present prior to illumination of the electrode surface (Figure 2.14) and the rate of hydrogen production is directly correlated with the current produced by the photocathode during illumination. Measurements performed using FeP|GaP working electrodes polarized at 0 V vs RHE also confirm the photoproduction of hydrogen. However, the Faradaic efficiency is ~45% following 6 min of illumination. To facilitate comparisons with data obtained using the metalloporphyrin-modified GaP constructs in aqueous conditions, cyclic voltammograms of 3 and 4 recorded in organic solvents with a supporting electrolyte (0.1 M tetrabutylammonium hexafluorophosphate in butyronitrile) are included in this report (Figure 2.15).

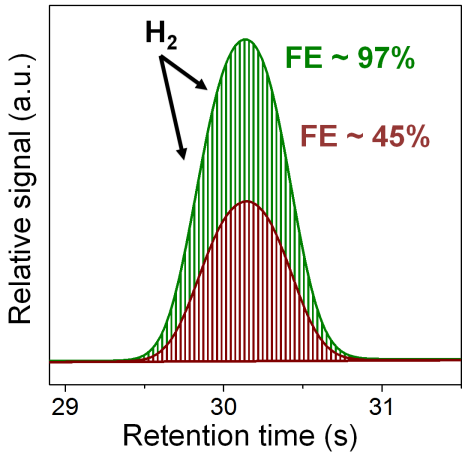

Figure 2.13. Gas chromatograms obtained using samples of headspace gas collected from sealed photoelectrochemical cells containing working electrodes polarized at a constant potential of 0 V vs RHE and under 1-sun illumination. The amount of hydrogen produced in these experiments corresponds to a Faradaic efficiency of 97% following 30

min of illumination using CoP|GaP and 45% following 6 min of illumination using FeP|GaP sample.

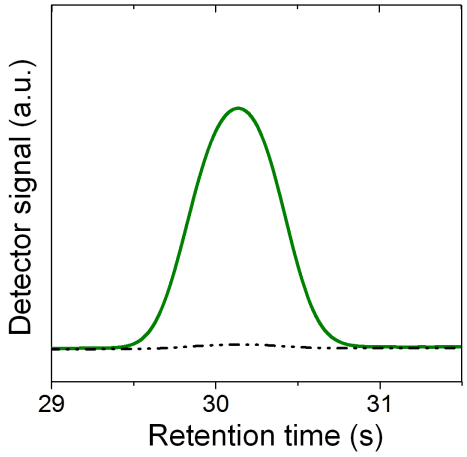

Figure 2.14. Gas chromatograms obtained using gas samples of the headspace collected from a sealed photoelectrochemical cell equipped with a CoP|GaP working electrode polarized at 0 V vs RHE. The samples were collected before (dash-dotted) and after (solid) 30 min of illumination (100 mW cm^{-2}).

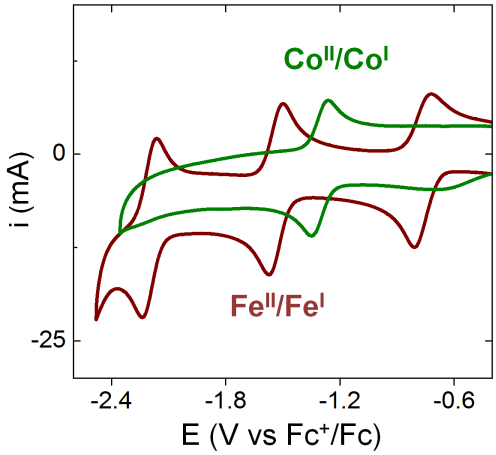

Figure 2.15. Cyclic voltammograms recorded using butyronitrile solutions of model cobalt porphyrin, 3, (green) or iron porphyrin, 4, (dark red) compounds.

Under these conditions, the difference in potential between the midpoints of the Co^{II}/Co^{I} and Fe^{II}/Fe^{I} couples is ~ 230 mV, with the cobalt relay occurring at less negative potentials (Table 2.1).

Table 2.1 Midpoint Potentials for the Reduction of 3 and 4.

Compound	^{III}E (V vs Fc^+/Fc)	^{II}E (V vs Fc^+/Fc)	^{i}E (V vs Fc^+/Fc)
3	NA	-1.33 (ΔEp=90 mV)	-
4	-2.21 (ΔE_p=80 mV)	-1.56 (ΔE_p=80 mV)	-0.78 (ΔE_p=84 mV)

For the metalloporphyrin-modified GaP surfaces, a difference in potential to access the catalytically active cobalt or iron redox state in aqueous conditions may contribute to the 120 mV offset required to achieve a -1 mA cm^{-2} current density using the CoP|GaP versus FeP|GaP photocathodes (Table 2.2).

Table 2.2 PEC Characteristics of GaP, CoP|GaP, and FeP|GaP Photocathodes.

Construct	V_{oc} (V vs RHE)	E at -1 mA cm^{-2} (V vs RHE)	J at 0 V vs RHE (mA cm^{-2})
GaP	0.57 ± 0.03	-0.04 ± 0.06	0.86 ± 0.21
CoP|GaP	0.61 ± 0.01	-0.35 ± 0.03	-1.31 ± 0.03
FeP|GaP	0.61 ± 0.01	+0.23 ± 0.07	-1.29 ± 0.04

However, other factors, including differences in hydricity of the metal centers[28-30] and possible changes in electronic structure of the underlying semiconductors upon functionalization[31-35] may contribute to this divergence. Nonetheless, the saturating current densities, measured at 0 V vs RHE using CoP|GaP working electrodes, do increase approximately linearly with illumination intensity (Figure 2.16), indicating that photocarrier transport to the interface in part limits the performance and that improvement in the spectral coverage and photophysical properties of the underpinning semiconductor could yield additional efficiency gains.

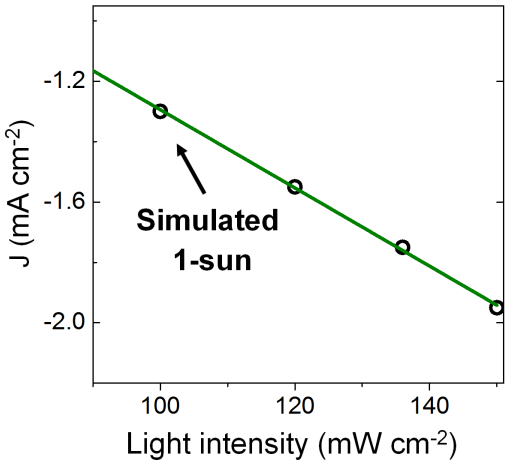

Figure 2.16. Photocurrent density recorded at increasing illumination intensity using a CoP|GaP working electrode polarized at 0 V vs RHE in phosphate buffer (pH 7).

A comparison of the photon flux striking the CoP|GaP surface at simulated 1-sun intensity with the electron flux measured during PEC testing allows an analysis of external quantum efficiency (EQE). Considering only photons in the GaP actinic range, i.e. those with energies higher than 2.26 eV GaP band gap, the EQE = 19% for CoP|GaP electrodes polarized at 0 V vs RHE. A similar analysis of the optical to chemical power conversion efficiency (η)[36] is achieved by comparing the spectral irradiance at this wavelength range with the output chemical power represented by the rate of hydrogen production. Using the enthalpy of H_2 combustion (286 kJ mol^{-1}) or change in Gibbs free energy (237 kJ mol^{-1}), η = 11% or 9%, respectively. These measurements are performed using a three-electrode configuration and thus represent energetics and efficiencies associated with a photocathode component, not a device.[37,38]

2.2.4 Turnover Frequency

Total cobalt loadings on the CoP|GaP surface were obtained using inductively coupled plasma mass spectrometry (ICP-MS), yielding a cobalt porphyrin surface concentration

of 0.59 ± 0.03 nmol cm^{-2}. The loadings obtained from this analysis combined with the current densities measured in polarization experiments using CoP|GaP working electrodes yield information on the activity of the electrodes per number of porphyrins assembled on the surface and thus an estimate of the immobilized porphyrin turnover frequency (TOF). Using only the increase in current density obtained for a GaP electrode polarized at 0 V vs RHE following cobalt porphyrin surface functionalization, this equates to TOF of 3.9 H_2 molecules $site^{-1}$ s^{-1}, representing one of the highest activity reported for a molecular-catalyst-modified semiconductor photoelectrode operating at the H^+/H_2 equilibrium potential under 1-sun illumination. In future work, implementation of porphyrins with improved catalytic features and the development of synthetic methodologies to achieve higher porphyrin surface loading as well as improved interfacial dynamics may lead to further performance gains.

2.3 Conclusions

In this chapter, a one-step method to chemically graft metalloporphyrin catalysts onto p-type gallium phosphide (100) is described. The cobalt and iron porphyrin complexes are structurally modified with a 4-vinylphenyl group essential to successful semiconductor attachment using the UV-induced grafting method. Structural analysis of the constructs using surface-sensitive characterization techniques, including XP and GATR-FTIR spectroscopies, provides evidence of successful grafting. The resulting hybrid material can be used as a photocathode for driving the hydrogen evolution half-reaction and shows significantly improved photoelectrochemical performance over unmodified gallium phosphide electrodes. When using GaP(100) with identical doping conditions (i.e. cut from the same ingot), the PEC results using CoP|GaP show an enhanced rate and stability of photoinduced hydrogen production over the analogous FeP|GaP assemblies. Co and Fe

porphyrins permit access to metal^{I}/metal^{0} redox couples and are known catalysts for the electrochemical reduction of carbon dioxide. Thus, methods to covalently graft porphyrins to semiconductor substrates could lead to new perspectives and approaches of photoelectrochemically activating carbon dioxide. In addition, the porphyrins are synthetically versatile, allowing tailoring of their molecular structure and electronic properties as new discoveries and material developments emerge. Key features of the reported constructs include the use of metalloporphyrins with built-in chemical sites for direct grafting to a GaP semiconductor, creating hybrid assemblies capable of converting photonic energy to fuel.

2.4 References

(1) Halmann, M. Photoelectrochemical Reduction of Aqueous Carbon Dioxide on P-Type Gallium Phosphide in Liquid Junction Solar Cells. *Nature* **1978**, *275*, 115–116.

(2) Grätzel, M. Photoelectrochemical Cells. *Nature* **2001**, *414*, 338–344.

(3) Liu, C.; Dasgupta, N. P.; Yang, P. Semiconductor Nanowires for Artificial Photosynthesis. *Chem. Mater.* **2014**, *26* (1), 415–422.

(4) Kaiser, B.; Fertig, D.; Ziegler, J.; Klett, J.; Hoch, S.; Jaegermann, W. Solar Hydrogen Generation with Wide-Band-Gap Semiconductors: GaP(100) Photoelectrodes and Surface Modification. *Chem. Phys. Chem.* **2012**, *13* (12), 3053–3060.

(5) Barton, E. E.; Rampulla, D. M.; Bocarsly, A. B. Selective Solar-Driven Reduction of CO_2 to Methanol Using a Catalyzed. *J. Am. Chem. Soc.* **2008**, *130* (20), 6342–6344.

(6) Price, M. J.; Maldonado, S. Macroporous N-GaP in Nonaqueous Regenerative Photoelectrochemical Cells. *J. Phys. Chem. C* **2009**, *113* (28), 11988–11994.

(7) Liu, C.; Sun, J.; Tang, J.; Yang, P. Zn-Doped p-Type Gallium Phosphide Nanowire Photocathodes from a Surfactant-Free Solution Synthesis. *Nano Lett.* **2012**, *12* (10), 5407–5411.

(8) Standing, A.; Assali, S.; Gao, L.; Verheijen, M. A.; van Dam, D.; Cui, Y.; Notten, P. H. L.; Haverkort, J. E. M.; Bakkers, E. P. A. M. Efficient Water Reduction with Gallium Phosphide Nanowires. *Nature Communication.* **2015**, *6*, 7824–7831.

(9) Li, B.; Franking, R.; Landis, E. C.; Kim, H.; Hamers, R. J. Photochemical Grafting and Patterning of Biomolecular Layers onto TiO_2 Thin Films. *ACS Appl. Mater. Interfaces* **2009**, *1* (5), 1013–1022.

(10) Moore, G. F.; Sharp, I. D. A Noble-Metal-Free Hydrogen Evolution Catalyst Grafted to Visible Light-Absorbing Semiconductors. *J. Phys. Chem. Lett.* **2013**, *4* (4), 568–572.

(11) Richards, D.; Zemlyanov, D.; Ivanisevic, A. Assessment of the Passivation Capabilities of Two Different Covalent Chemical Modifications on GaP(100). *Langmuir* **2010**, *26* (11), 8141–8146.

(12) Seifert, M.; Koch, A. H. R.; Deubel, F.; Simmet, T.; Hess, L. H.; Stutzmann, M.; Jordan, R.; Garrido, J. A.; Sharp, I. D. Functional Polymer Brushes on Hydrogenated Graphene. *Chem. Mater.* **2013**, *25* (3), 466–470.

(13) Steenackers, M.; Gigler, A. M.; Zhang, N.; Deubel, F.; Seifert, M.; Hess, L. H.; Lim, C. H.; Loh, K. P.; Garrido, J. A.; Jordan, R.; et al. Polymer Brushes on Graphene. *J. Am. Chem. Soc.* **2011**, *133* (27), 10490–10498.

(14) Cicero, R. L.; Linford, M. R.; Chidsey, C. E. D. Photoreactivity of Unsaturated Compounds with Hydrogen-Terminated Silicon(111). *Langmuir* **2000**, *16* (13), 5688–5695.

(15) Krawicz, A.; Yang, J.; Anzenberg, E.; Yano, J.; Sharp, I. D.; Moore, G. F. Photofunctional Construct That Interfaces Molecular Cobalt-Based Catalysts for H_2 Production to a Visible-Light-Absorbing Semiconductor. *J. Am. Chem. Soc.* **2013**, *135* (32), 11861–11868.

(16) Beiler, A. M.; Khusnutdinova, D.; Jacob, S. I.; Moore, G. F. Solar Hydrogen Production Using Molecular Catalysts Immobilized on Gallium Phosphide (111)A and (111)B Polymer-Modified Photocathodes. *ACS Appl. Mater. Interfaces* **2016**, *8* (15), 10038–110047.

(17) Sun, Z.-C.; She, Y.-B.; Zhou, Y.; Song X.-F.; Li, K. Synthesis, Characterization and Spectral Properties of Substituted Tetraphenylporphyrin Iron Chloride Complexes. *Molecules* **2011**,*16* (4), 2960–2970.

(18) Lu, X.; Geng, Z.; Wang, Y.; Lv, B.; Kang, J. Synthesis and Characterization of Three New Unsymmetrical Porphyrins and Their Cobalt Complexes. *Synth. React. Inorg. Met. Org. Chem.* **2002**, *32* (5), 843–851.

(19) Costa, A. A.; Ghesti, G. F.; Macedo, J. L.; Braga V. S.; Santos, M. M., Dias, J. A., Dias, S. L. Immobilization of Fe, Mn and Co Tetraphenylporphyrin Complexes in MCM-41 and their Catalytic Activity in Cyclohexene Oxidation Reaction by Hydrogen Peroxide. *J. of Mol. Cat. A* **2008**, *282* (1-2), 149–157.

(20) Karweik, D. H.; Winograd, N. Nitrogen Charge Distributions in Free-Base Porphyrins, Metalloporphyrins, and Their Reduced Analogues Observed by X-Ray Photoelectron Spectroscopy. *Inorg. Chem.* **1976**,*15* (10), 2336–2342.

(21) Flechtner, K.; Andreas Kretschmann, A.; Steinrück, H.-P.; Gottfried, J. M. NO-Induced Reversible Switching of the Electronic Interaction between a Porphyrin-Coordinated Cobalt Ion and Silver Surface. *J. Am. Chem. Soc.* **2007**,*129* (40), 12110–12111.

(22) Lipińska, M. E.; Novais, J. P.; Rebelo, S. L.-H.; Bachiller-Baeza, B.; Rodriguez-Ramos, I.; Guerrero-Ruiz, A.; Freire, C. Microwave Assisted Silylation of Graphite Oxide and Iron (III) Porphyrin Interaction. *Polyhedron* **2014**, *81*, 475–484.

(23) Oveisi, A. R.; Zhang, K.; Khorramabadi-zad, A.; Farha O. K.; Hupp, J. T. Stable and Catalytically Active Iron Porphyrin-Based Porous Organic Polymer: Activity as Both a Redox and Lewis Acid Catalyst. *Sci. Rep*. **2015**, *5*, 10621–10629.

(24) Shin, K.; Kramer, S. K.; Goff, H. M. Base-Promoted Autoreduction of Iron(III) Porphyrins in Dimethyl Sulfoxide Solution: Magnetic Resonance Spectroscopy of Hydroxoiron(II) Porphyrin Complexes. *Inorg. Chem.* **1987**, *26* (24), 4103–4106.

(25) Modi, S.; Shedbalkar, V. P.; Behere, D. V. Kinetics of Autoreduction of Iron(III) Porphyrins by Cyanide Ion. *Inorg. Chim. Acta* **1990**, *173* (1), 9–12.

(26) Balch, A. L.; Noll, B. C.; Olmstead, M. M.; Phillips, S. L. Structural and Spectroscopic Characterization of Iron(III) Dioxoporphodimethene Complexes and Their Autoreduction to an Iron(II) Complex in Pyridine. *Inorg. Chem.* **1996**, *35* (22), 6495–6506.

(27) Claire, T. N. St.; Balch, A. L. *In Situ* Monitoring of the Degradation of Iron Porphyrins by Dioxygen with Hydrazine as Sacrificial Reductant. Detection of Paramagnetic Intermediates in the Coupled Oxidation Process by ^{1}H NMR Spectroscopy. *Inorg. Chem*. **1999**, *38* (4), 684–691.

(28) DuBois, D. L.; Berning, D. E. Hydricity of Transition-Metal Hydrides and Its Role in CO_2 Reduction. *Appl. Organomet. Chem.* **2000**, *14*, 860–862.

(29) Creutz, C.; Chou, M. H. Hydricities of d^6 Metal Hydride Complexes in Water. *J. Am. Chem. Soc.* **2009**, *131* (8), 2794–2795.

(30) Connelly, S. J.; Wiedner, E. S.; Appel, A. M. Predicting the Reactivity of Hydride Donors in Water: Thermodynamic Constants fir Hydrogen. *Dalton Trans.* **2015**, *44*, 5933–5938.

(31) Barroso, M.; Cowan, A. J.; Pendlebury, S. R.; Grätzel, M.; Klug, D. R.; Durrant, J. R. The Role of Cobalt Phosphate in Enhancing the Photocatalytic Activity of α-Fe_2O_3 Toward Water Oxidation. *J. Am. Chem. Soc.* **2011**, *133* (38), 14868–14871.

(32) Lin, F.; Boettcher, S. W. Adaptive Semiconductor/Electrocatalyst Junctions in Water-Splitting Photoanodes. *Nat. Mater.* **2014**, *13* (1), 81–86.

(33) Thorne, J. E.; Li, S.; Du, C.; Qin, G.; Wang, D. Energetics at the Surface of Photoelectrodes and Its Influence on the Photoelectrochemical Properties. *J. Phys. Chem. Lett.* **2015**, *6* (20), 4083–4088.

(34) Klahr, B.; Gimenez, S.; Fabregat-Santiago, F.; Hamann, T.; Bisquert, J. Water Oxidation at Hematite Photoelectrodes: The Role of Surface Stets. *J. Am. Chem. Soc.* **2012**, *134* (9), 4294–4302.

(35) Waegele, M. M.; Chen, X.; Herlihy, D. M.; Cuk, T. How Surface Potential Determines the Kinetic of the First Hole Transfer of Photocatalytic Water Oxidation. *J. Am. Chem. Soc.* **2014**, *136* (30), 10632–10639.

(36) Nozik, A. J. Photoelectrolysis of Water Using Semiconducting TiO_2 Crystals. *Nature* **1975**, *257*, 383–386.

(37) Chen, Z.; Jaramillo, T.F.; Deutsch, T. G.; Kleiman-Shwarsctein, A.; Forman, A. J.; Gaillard, N.; Garland, R.; Takanabe, K.; Heske, C.; Sunkara, M.; et. al. Accelerating materials Development for Photoelectrochemical Hydrogen Production: Standards for Methods, Definitions, and Reporting Protocols. *J. Mater. Res*., **2010**, *25* (1), 3–16.

(38) Khusnutdinova, D.; Beiler, A. M.; Wadsworth B. L.; Jacob S. I.; Moore G. F. Metalloporphyrin-modified Semiconductors for Solar Fuel Production. *Chem. Sci.* **2017**, *8* (1), 253–259.

CHAPTER 3 SYNTHESIS AND CHARACTERIZATION OF A COBALT FLUORO-PORPHYRIN WITH A BUILT-IN SURFACE ATTACHMENT MOIETY

Portions of this work are excerpted with permission from:

Khusnutdinova, D.; Flores, M.; Beiler, A. M.; Moore, G. F. *Photosynthetica* **2018**, *56* (1), 67–74.

The final publication is available at link.springer.com/article/10.1007/s11099-018-0783-y

3.1 Introduction

Controlled synthetic manipulations of molecular structure and peripheral substituents of porphyrin macrocycles enable the design and preparation of molecular catalysts with desired properties and functions. In this chapter, the synthesis and characterization of a novel cobalt(II) 5,10,15,20-tetrakis(3-fluorophenyl)porphyrin bearing a 4-vinylphenyl surface attachment group at a beta position on the macrocycle is described. Electrochemical measurements show the 3-fluorophenyl groups at the *meso*-positions of the porphyrin perturb the reduction potentials of the complex to more positive values as compared to non-fluorinated analogs, thus allowing access to reduced cobalt porphyrin species at significantly less negative applied bias potentials.

Fluorine substitution provides a powerful synthetic tool in organic and bioorganic chemistry.[1,2] The chemical stability and relatively small size of fluorine coupled with its highly electron-withdrawing nature (a 4.0 on the Pauling scale) are attractive features. In addition to the use of fluoro-groups as reporters in ^{19}F NMR studies[3-6], this highly electronegative group has shown promise in promoting novel protein-substrate as well as protein-protein interactions[7-9] and provides a molecular strategy for tuning the electrochemical properties of redox catalysts and mediators.[10-15]

Porphyrins serve important roles in living systems and as molecular components in technological assemblies for sensor applications, catalysis, and energy transduction. As an example of the latter described in Chapter 2, a synthetic methodology to chemically graft metalloporphyrins to visible-light-absorbing semiconductors for construction of an integrated photocathode with applications in artificial photosynthesis[16-23] including light activation of chemical transformations for capturing, converting, and storing solar energy in the form of chemical bonds. In this assembly, the semiconductor serves as a light

capture and conversion component as well as a physical support for assembling the modified cobalt fluoro-porphyrin catalysts. Thus the assembly combines solid-state light capture and conversion materials with molecular surface coatings to enhance photoelectrochemical fuel production activity. For the fluorinated porphyrin analog described in this report, electrochemical measurements show the $Co^{II/I}$ redox process occurs ≈100 mV less negative than that of the previously reported nonfluorinated analog described in Chapter 2. In addition, a second reduction process, occurring at more negative potentials and assigned to the Co^{I}/Co^{0} couple, is clearly resolved within the electrochemical window of the solvent. These results are consistent with the electron-withdrawing nature of the 3-fluorophenyl substituents and previous reports on cobalt(II) tetrakis(3-fluorophenyl)porphyrin[24,25], a known homogeneous electrocatalyst for the reduction of CO_2 in solution studies.

Nuclear magnetic resonance, electron paramagnetic resonance, UV-Vis absorption, and Fourier transform infrared spectroscopies coupled with mass spectrometry confirm successful synthesis of the target compound and provide information on the magnetic, electronic, and vibrational structure of the complex. The unique electron configuration surrounding the nucleus of fluorine in molecules (on average it is surrounded by nine electrons) provides a wider range and higher sensitivity of the fluorine chemical shifts than those typically encountered with other elements resulting in an unprecedented upfield ^{19}F resonance ascribed to the unique connectivity of the reported structure and causing close proximity of one of the 3-fluorophenyl groups to the ring current of the covalently attached 4-vinylphenyl surface attachment group.

3.2 Results and Discussion

3.2.1 Materials Preparation

Synthesis of 5,10,15,20-tetrakis(3- fluorophenyl)porphyrin (6), 2-bromo-5,10,15,20-tetrakis (3-fluorophenyl)porphyrin (7), 5,10,15,20-tetrakis(3-fluorophenyl)-2-(4-vinylphenyl) porphyrin (8), cobalt(II) 5,10,15,20-tetrakis(3-fluorophenyl)-2-(4-vinylphenyl) porphyrin (9), and cobalt(II) 5,10,15,20-tetrakis(3-fluorophenyl)porphyrin (10) is described in detail in Chapter 6.

3.2.2 Synthesis and Characterization

The synthetic scheme used to prepare the target compound, 9, is shown in Figure 3.1.

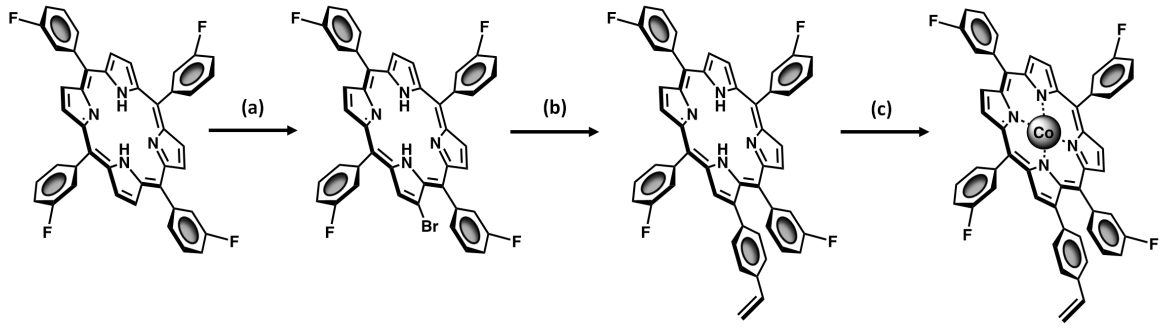

Figure 3.1. Synthetic scheme used to prepare cobalt(II) 5,10,15,20-tetrakis(3-fluorophenyl)-2-(4-vinylphenyl)porphyrin where (a) NBS, $CHCl_3$, Ar, reflux; (b) 4-VPBA, K_2CO_3, $Pd(Ph_3)_4$, reflux; (c) $Co(OAc)_2*4H_2O$, DMF, reflux.

The starting material, 5,10,15,20-tetrakis(3-fluorophenyl) porphyrin, 6, is synthesized according to previously reported literature procedures.[26,27] Bromination of 6 with N-bromosuccinamide (NBS) in a mixture of dichloromethane and methanol affords 2-bromo-5,10,15,20-tetrakis (3-fluorophenyl)porphyrin, 7, in 45% yield. Successful monobromination at the beta position of the macrocycle is confirmed by NMR spectroscopy and MALDI-TOF mass spectrometry. In particular, the β-pyrrolic proton resonances in the ^1H NMR spectrum of 7 observed as a broad multiplet signal between

8.75–8.95 ppm that integrates to seven, consistent with the magnetically nonequivalent environments of the β-pyrrolic protons following the bromination reaction. This is in stark contrast to the starting compound 6, where the four-fold symmetry of the macrocycle results in a single β-proton resonance that integrates to eight and is centered at 8.86 ppm (Figure 3.2).

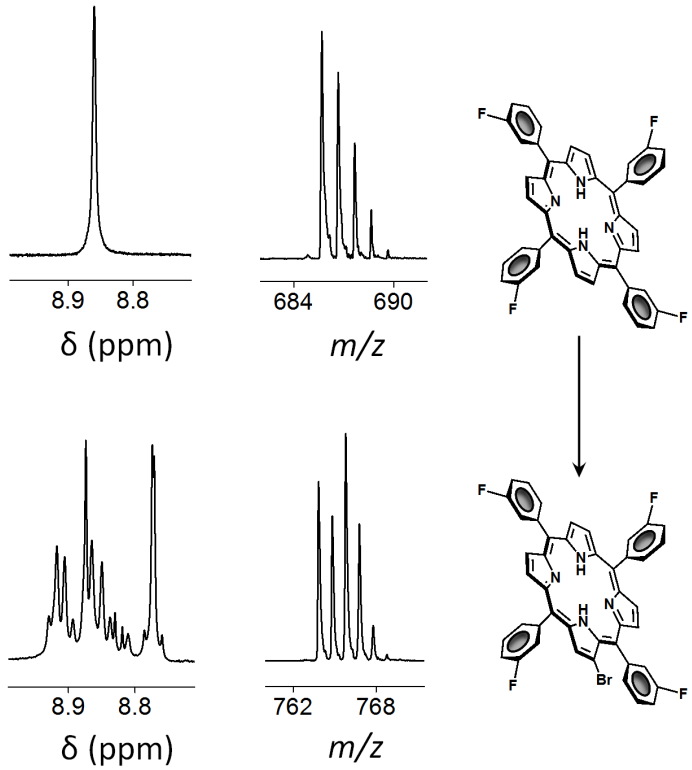

Figure 3.2. ^{1}H NMR spectra showing the symmetry of β-pyrrolic protons of compound 6 (top left) and compound 7 (bottom left). MALDI-TOF MS data showing the isotopic distribution patterns of 6 (top center) and 7 (bottom center). Corresponding molecular structures of 6 (top right) and 7 (bottom right).

As anticipated for the unique isotopic distribution patterns associated with bromine-containing compounds, 7 reveals two isotope clusters with near equal intensities and *m/z* = 763.83 and 765.89 for the M^+ peaks (where M = $C_{44}H_{25}BrF_4N_4$, calcd. 764.12 and 766.12). In comparison with the absorption spectrum of 6, a 3 nm bathochromic shift is observed for the Soret absorption maximum as well as all four Q-bands, and the transition at 548 nm is diminished in relative intensity with respect to the other three Q-band transitions.

In the next synthetic step, a Suzuki cross-coupling reaction between 7 and 4-vinylphenyl boronic acid is used to prepare 5,10,15,20-tetrakis(3-fluorophenyl)-2-(4-vinylphenyl)porphyrin, compound 8, with 58% yield. Confirmation of the molecular connectivity of 8 includes, but is not limited to, ^{1}H, ^{13}C, and ^{19}F NMR spectroscopy. The ^{1}H NMR spectrum of 8 shows the characteristic splitting pattern in the region of 5.11– 6.90 ppm associated with the resonances of the vinylic protons and consistent with their assignments. The proton NMR spectrum of this region is shown in Figure 3.3 along with the overlaid 2-dimensional gradient correlation spectroscopy (gCOSY) spectrum showing the cross-peak patterns assigned to trans- and cis-vicinal coupling between the doublet of doublets (J = 20 Hz, J = 12 Hz) proton signal H_a at 6.76 ppm and the signals assigned to the pair of geminal protons H_b and H_c appearing as doublets (J = 20 Hz and J = 12 Hz) at 5.78 ppm and 5.30 ppm, respectively. In the ^{13}C NMR spectrum of 8 a signal at 204.37 ppm is assigned to the deshielded carbons that are directly bound to fluorines. Finally, unlike the single triplet observed at –116.40 ppm in the ^{19}F spectra of 6, arising from the magnetic equivalence of the four fluoro groups and coupling to neighboring protons, the ^{19}F NMR spectrum of 8 confirms the presence of magnetically nonequivalent fluorine environments, including a relatively upfield triplet at –117.86 ppm (Figure 3.4).

The upfield shift of this resonance is ascribed to the operation of a unique through space phenyl ring current effect induced by the nearby 4-vinylphenyl moiety.

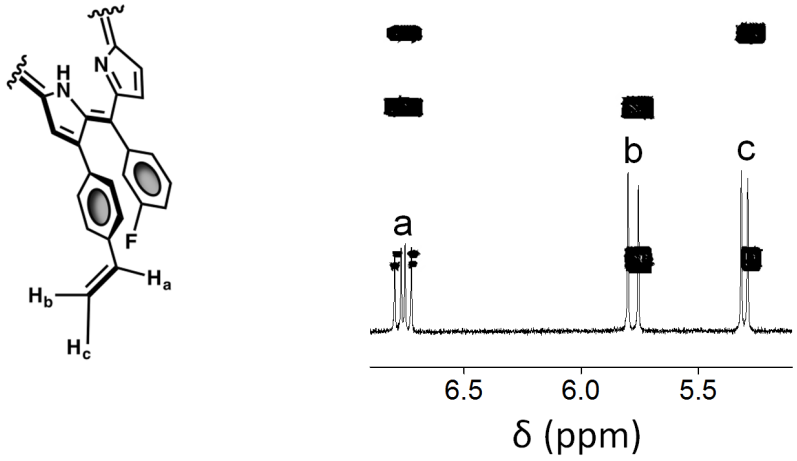

Figure 3.3. (left) Molecular structural fragment of compound 8 depicting a conformation in which the fluorine of a 3-fluorophenyl group is exposed to the ring current of the nearby 4-vinylphenyl moiety; (right) ^{1}H NMR spectrum showing the vinylic proton region of 8 and the overlaid gCOSY spectrum.

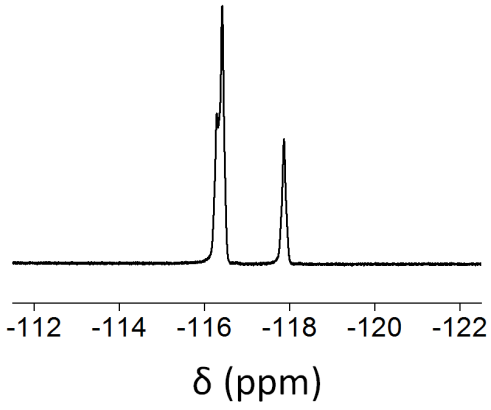

Figure 3.4. ^{19}F NMR of compound 8 showing the unique magnetic environments of the four fluoro groups, including a significantly upfield resonance centered at –117.86 ppm.

In the final synthetic step, the target compound is prepared by treating porphyrin 8 with cobalt(II) acetate in a refluxing solution of dimethylformamide, yielding cobalt(II) 5,10,15,20-tetrakis(3-fluorophenyl)-2-(4-vinylphenyl)porphyrin, compound 9, with 98% yield, following purification via column chromatography. Successful insertion of cobalt into the tetrapyrrolic macrocycle of 8 is confirmed by the electronic absorption (UV-Vis) spectrum of the target molecule collected in dichloromethane. The absorption spectrum of 9 shows two intense bands with one component associated with the Soret band transition at 412 nm and another for a Q-band transition appearing at 532 nm. This result is consistent with the approximate D_{4h} symmetry of the macrocycle following the metal insertion. Conversely the Q-band transitions of the free-base porphyrins appear as four absorption bands due to the reduced symmetry. For the target compound, there is also a ≈ 5 nm red shift of the Soret band and lowest energy Q-band as compared to a spectrum of cobalt(II) 5,10,15,20-tetrakis(3-fluorophenyl) porphyrin, 10, a model porphyrin compound that does not contain the 4-vinylphenyl functional group. The conversion of 8 into 9 was also confirmed by FTIR spectroscopy; in particular, the transmission spectrum of 9 does not contain the peak at 980 cm^{-1} associated with pyrrolic in-plane N–H porphyrin deformation of the free-base fluorinated porphyrin 6.[28] Instead, a new feature appears at 1004 cm^{-1} that is associated with an in-plane cobalt porphyrin deformation.[29, 30] The FTIR transmission spectrum of 9 also includes vibrational features assigned to C_{β}– H, C_{α}–C_{β} (1078–1111 cm^{-1}), C_m–C_{ph} (1265–1303 cm^{-1}), C_{α}–N (1347 cm^{-1}), C_{β}=C_{β}, C=C_{ph} (1377–1480 cm^{-1}), and C–F (1133–1178, 1554–1627 cm^{-1}) modes (Figure 3.5).[31-33]

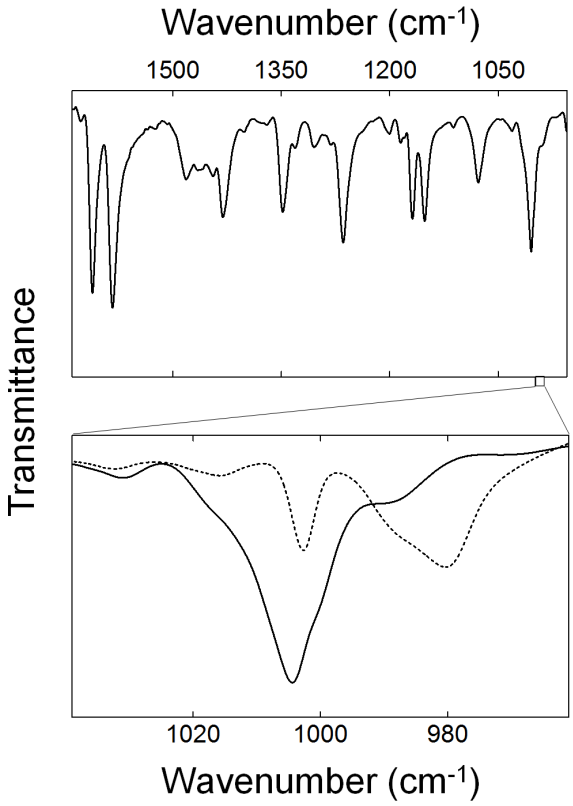

Figure 3.5. FTIR transmission spectrum of 9 collected in KBr (top) and an expanded plot of the 961–1039 cm^{-1} region (bottom), showing the transmission spectrum of 9 (solid) as well as the free-base precursor 3 (dashed).

The electronic structure of 9 was also investigated using X-band (9.44 GHz) electron paramagnetic resonance (EPR) spectroscopy at 4 K (Figure 3.6). The observed spectral features are consistent with a S = 1/2 spin system. To obtain the EPR parameters, the respective spin Hamiltonian was fit to the data. The EPR spectrum of 9 is well fit considering a low-spin ^{59}Co(II) center (d^7, S_{Co} = 1/2, I_{Co} = 7/2) with anisotropic *g*-values (g_x = 2.081, g_y = 2.020, g_z = 1.966) and non-resolved hyperfine coupling interactions between the magnetic moment of the unpaired electron and the magnetic moment of the ^{59}Co nucleus. Finally, the MS data of 9 show a single isotope cluster with *m/z* = 844.96

for M^+ (where M = $C_{52}H_{30}CoF_4N_4$, calcd. 845.17), consistent with the mass of the target compound.

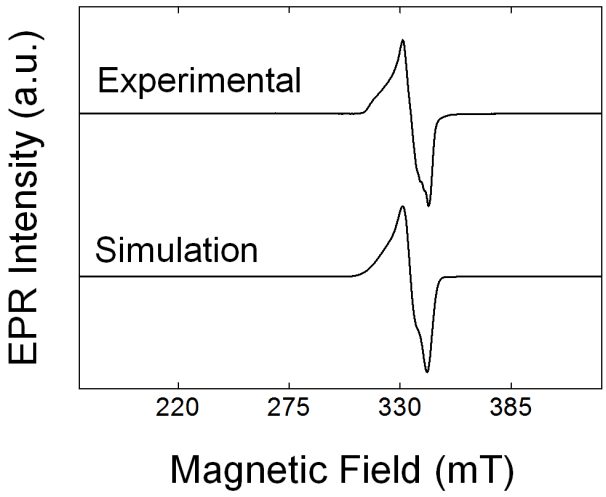

Figure 3.6. Experimental (top) and simulated (bottom) X-band (9.44 GHz) EPR spectra of 9 collected at 4 K in dichloromethane.

3.2.3 Electrochemical Studies

The electrochemical properties of 9 were studied via cyclic voltammetry (CV) in an argon sparged solution of 0.1 M tetrabutylammonium hexafluorophosphate in butyronitrile using a glassy carbon working electrode, a platinum counter electrode, and a silver wire pseudo reference with ferrocene as an internal standard (Figure 3.7).
Under these conditions, the CV of 9 shows three well-defined redox features within the potential window + 0.98 to –2.22 V vs SCE that for simplicity are assigned to metal-based redox processes. However, distinguishing ligand-based reductions from those that are metal-centered can be difficult and reductive processes of cobalt porphyrins have been ascribed to both innocent and non-innocent ligand chemistry.[32,34-36]

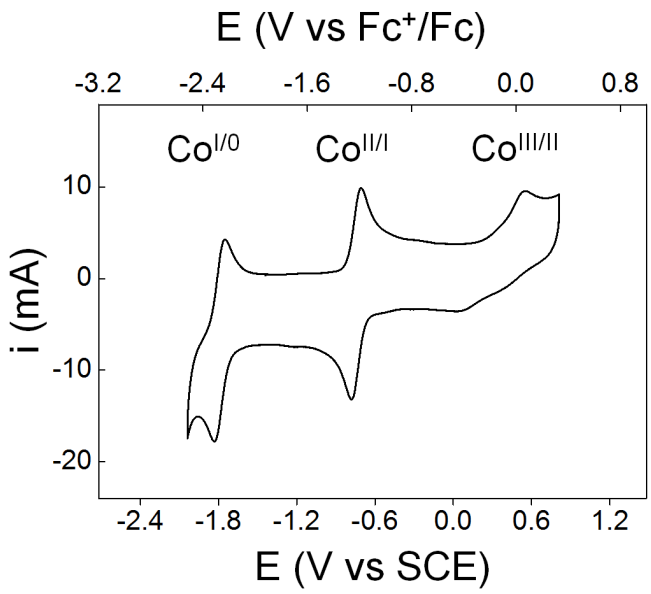

Figure 3.7. Cyclic voltammogram of 9 recorded in 0.1 M tetrabutylammonium hexafluorophosphate in butyronitrile under argon using a glassy carbon electrode and a scan rate of 500 mV s^{-1}.

This situation is of particular interest in connection with catalysis of multielectron redox processes by earth abundant metals where one-electron redox-state changes are often preferred. Assignments of the redox couples measured for 9, their midpoint potentials ($^{n}E_{1/2}$), and associated peak-to-peak separations (ΔE_p) are listed in Table 3.1.

Table 3.1. Midpoint Potentials for the Reduction, ^{nI}E, and Oxidation, ^{ni}E, of 9.

Compound	$^{n}E_{1/2}$ (V vs SCE), (ΔEp, mV)		
	^{II}E ($Co^{I/0}$ or P/P^{-})	^{I}E ($Co^{II/I}$)	^{i}E ($Co^{III/II}$)
9	-1.79 (77)	-0.75 (72)	+0.29 (379)

The most oxidative feature, at $E_{1/2}$ = + 0.29 V vs SCE, is ascribed to the Co^{III}/Co^{II} couple, a quasi-reversible process with a relatively large peak-to-peak separation (ΔE_p = 379 mV) due to sluggish electron transfer during the oxidation of low spin Co^{II} ion and a slow self-exchange electron transfer rate.[32, 37] The Co^{II}/Co^{I} redox couple is assigned to the chemically reversible process occurring at $E_{1/2}$ = –0.75 V vs SCE with a peak-to-peak separation of 72 mV and the Co^{I}/Co^{0} redox couple is assigned to the most reducing feature at $E_{1/2}$ = –1.79 V vs SCE with a peak-to-peak separation of 77 mV. In comparison with cobalt(II) 5,10,15,20-tetrakis(4-methylphenyl)-2-(4-vinylphenyl)porphyrin, the complex reported here allows access to the Co^{II}/Co^{I} and Co^{I}/Co^{0} relays at significantly less negative applied bias potentials. Likewise, these values are consistent with reports on the electrochemistry of cobalt(II) 5,10,15,20- tetrakis(3-fluorophenyl)porphyrin, a known homogeneous electrocatalyst for the reduction of CO_2 in solution studies. Thus, installment of the 4-vinylphenyl moiety does not deactivate the ability of the fluorinated porphyrin complex to access the Co^{I} and Co^{0} states at relatively low (i.e. less negative) potentials.

3.3 Conclusions

A novel synthetic methodology to prepare a cobalt(II) tetrakis(3-fluorophenyl)porphyrin with a built-in 4-vinylphenyl surface attachment moiety is reported. Spectroscopic characterization, including: ^{1}H NMR, ^{13}C NMR, ^{19}F NMR, UV-Vis, FTIR, and EPR, as well as MALDI-TOF MS confirm the molecular structure of the target molecule. Electrochemical studies reveal the 3-fluorophenyl substituents allow the porphyrin complex to deliver relatively low potential Co^{I} and Co^{0} species as compared to a previously reported non-fluorinated analog. The surface attachment chemistry will be shown and discussed in Chapter 4; however, the photoelectrochemical properties of resulting complex will be part of a future report.

3.4 References

(1) O´Hagan, D.; Rzepa, H. S. Some Influences of Fluorine in Bioorganic Chemistry. *Chem. Commun.* **1997**, *7*, 645–652. *Nature* **1978**, *275*, 115–116.

(2) Chambers, R. D. Fluorine in Organic Chemistry. *Blackwell Publishing Ltd. Oxford.* **2004.**

(3) Gerig, J. T. Fluorin Magnetic Resonance in Biochemistry. *Biol. Magn. Reson., Springer*, *New York*, **1978**.

(4) Sykes, B. D.; Hull, W. E.; Snyder, G. H. Experimental Evidence for Role of Cross-relaxation in Proton Nuclear Magnetic Resonance Spin Lattice Relaxation Time Measurements in Proteins. *Biophys. J*. **1978**, 21 (2), 137–146.

(5) Toi, H.; Homma, M.; Suzuki, A.; Ogoshi, H. Paramagnetic ^{19}F N.M.R. Spectra of Iron(III) Porphyrins Substituted with CF_3 Groups and Reconstituted Myoglobin. *J. Chem. Soc. Chem. Comm.* **1985**, *24*, 1791–1792.

(6) Dalvit, C.; Vulpetti, A. Fluorine – Protein Interactions and ^{19}F NMR Isotopic Chemical Shifts: an Empirical Correlation with Implication for Drug Design. *Chem. Med. Chem.* **2011**, *6* (1), 104–114.

(7) Tierno, M. E.; Mead, D.; Asato, A. E.; Liu, R. S.; Sekiya, N.; Yoshihara, K.; Chang, C. W.; Nakanishi, K.; Govindjee, R.; Ebrey, T. G. 14-Fluorobacterio-rhodopsin and other Fluorinated and 14-substituted Analogues. An Extra, Unusually Red-shifted Pigment Formed During Dark Adaptation. *Biochemistry* **1990**, *29* (25), 5948–5953.

(8) Kim, C.-Y.; Chang, J. S.; Doyon, J. B.; Baird, T. T.; Fierke, C. A.; Jain, A.; Chrristianson, D. W. Contribution of Fluorine to Protein – Ligand Affinity in the Binding of Fluoro-aromatic Inhibitors to Carbonic Anhydrase II. *J. Am. Chem. Soc.* **2000**, *122* (49), 12125–12134.

(9) Yolder, N. C.; Kumar, K. Fluorinated Amino Acids in Protein Design and Engineering. *Chem. Soc. Rev.* **2002**, *31* (6), 335–341.

(10) Rosenthal ,J.; Luckett, T. D.; Hodgkiss, J. M.; Nocera, D. G. Photocatalytic Oxidation of Hydrocarbons by a Bis-iron(III)-μ-oxo Pacman Porphyrin Using O_2 and Visible Light. *J. Am. Chem. Soc.* **2006**, *128* (20), 6546–6547.

(11) Moore, G. F.; Hambourger, M.; Gervaldo, M.; Poluektov, O. G.; Rajh, T.; Gust, D.; Moore, T.A.; Moore, A. L. A Bioinspired Construct that Mimics the Proton Coupled Electron Transfer between $P680^{*}+$ and the Tyr(Z)-His 190 Pair of Photosystem II. *J. Am. Chem. Soc.* **2008**, *130* (32), 10466–10467.

(12) Moore, G. F.; Konezny, S. J.; Song, H.; Milot, R. L.; Blakemore, J. D.; Minjoo, L. L.; Batista, V. S.; Schmuttenmaer, C. A.; Crabtree, R. H.; Brudvig, G. W. Bioinspired High-potential Porphyrin Photoanodes. *J. Phys. Chem. C* **2012**, *116* (7), 4892–4902.

(13) Rose, M. J.; Gray, H. B.; Winkler, J. R. Hydrogen Generation Catalyzed by Fluorinated Diglyoxime-iron Complexes at Low Overpotentials. *J. Am. Chem. Soc.* **2012**, *134* (20), 8310–8313.

(14) Cedeno, D.; Krawicz, A.; Doak, P. Using Molecular Design to Control the Performance of Hydrogen-Producing Polymer-Brush-Modified Photocathodes. *J. Phys. Chem. Lett.* **2014**, *5* (18), 3222–3226.

(15) Berben, L. A.; Peters, J. C. Hydrogen Evolution by Cobalt Tetraimine Catalysts Adsorbed on Electrode Surfaces. *Chem. Commun.* **2010**, *46* (3), 398–400.

(16) Bard, A.; Fox, M. A. Artificial Photosynthesis: Solar Splitting of Water to Hydrogen and Oxygen. *Acc. Chem. Res.* **1995**, *28* (3), 141–145.

(17) Blankenship, R. E.; Tiede, D. M.; Barber, J.; Brudvig, G. W.; Fleming, G.; Ghirardi, M.; Gunner, M. R.; Junge, W.; Kramer, D. M.; Melis, A.; et al. Comparing Photosynthetic and Photovoltaic Efficiencies and Recognizing the Potential for Improvement. *Science* **2011**, *332* (6031), 805–809.

(18) Khusnutdinova, D.; Beiler, A. M.; Wadsworth B. L.; Jacob S. I.; Moore G. F. Metalloporphyrin-modified Semiconductors for Solar Fuel Production. *Chem. Sci.* **2017**, *8* (1), 253–259.

(19) Najafpour, M. M.; Shen, J.-R.; Barber, J.; Moore, G. F. Running on Sun. *Chem. World* **2012**, 43.

(20) Faunce, T. A.; Styring, S.; Wasielewski, M. R.; Brudvig, G. W.; Rutherford, A. W.; Messinger, J.; Lee, A. F.; Hill, C. L.; DeGroot, H.; Fontecave, M.; et al. Artificial Photosynthesis as a Frontier Technology for Energy Sustainability. *Energy Environ. Sci.* **2013**, *6* (4), 1074.

(21) Maher, A. G.; Passard, G.; Dogutan, D. K.; Halbach, R. L.; Anderson, B. L.; Gagliardi, C. J.; Taniguchi, M.; Lindsey, J. S.; Nocera, D. G. Hydrogen Evolution Catalysis by a Sparsely Substituted Cobalt Chlorin. *ACS Catal.* **2017**, *7* (5), 3597–3606.

(22) Hou, H. J. M.; Najafpour, M. M.; Moore, G. F.; Allakhverdiev, S. I. Photosynthesis: Structures, Mechanisms, and Applications. *Springer*, *New York* **2017**, 321–358.

(23) Moore, G. F. Concluding Remarks and Future Perspectives: Looking Back and Moving Forward. *Springer*, *New York* **2017**, 407–414.

(24) Behar, D.; Dhanasekaran, T.; Neta, P.; Hosten, C. M.; Ejeh, D.; Hambright, P.; Fujita, E. Cobalt Porphyrin Catalyzed Reduction of CO2. Radiation Chemical, Photochemical, and Electrochemical Studies. *J. Phys. Chem. A* **1998**, *102* (17), 2870–2877.

(25) Dhanasekaran, T. Grodkowski, J.; Neta, P.; Hambright, P.; Fujita, E. p-Terphenyl-sensitized Photoreduction of CO_2 with Cobalt and Iron Porphyrins. Interaction between CO and Reduced Metalloporphyrins. *J. Phys. Chem. A*, **1999**, *103* (38), 7742–7748.

(26) Adler, A. D.; Longo, F. R.; Finarelli, J. D.; Goldmacher, J.; Assour, J.; Korsakoff, L.A Simplified Synthesis for Meso-tetraphenylporphyrin. *J. Org. Chem.* **1967**, *32* (2), 476–476.

(27) Tomkowicz, Z.; Rams, M.; Bałanda, M.; Foro, S.; Nojiri, H.; Krupskaya, Y.; Kataev, V.; Büchner, B.; Nayak, S. K.; Yakhni, J. V.; Haase, W. Slow Magnetic Relaxations in Manganese(III) Tetra(*meta*-fluorophenyl)-porphyrin-tetracyanoethenide. Composition with the Relative Single Chain Magnet *ortho* Compound. *Inorg. Chem.* **2012**, *51* (18), 9983–9994.

(28) Alben, J. O.; Choi, S. S.; Adler, A. D.; Caughey, W. S. Infrared Spectroscopy of Porphyrins. *Ann. NY Acad. Sci.* **1973**, *206*, 278–295.

(29) Boucher, L. J.; Katz, J. J. The Infrared Spectra of Metalloporphyrins (4000–160 cm^{-1}). *J. Am. Chem. Soc.* **1967**, *89* (6), 1340–1345.

(30) Kincaid, J.; Nakamoto, K. Vibrational Spectra of Transition Metal Complexes of Tetraphenylporphine. *J. Inorg. Nucl. Chem*. **1975**, *37* (1), 85–89.

(31) Nguyen, K.; Day, P. N.; Pachter, R. Effects of Halogenation on the Ionized and Excited States of Free-base and Zinc Porphyrins. *J. Chem. Phys.* **1999**, *110*, 9135–9144.

(32) Sun, H.; Smirnov, V.; DiMagno, S. G. Slow Electron Transfer Rates for Fluorinated Cobalt Porphyrins: Electronic and Conformational Factors Modulating Metalloporphyrin ET. *Inorg. Chem.* **2003**, *42* (19), 6032–6040.

(33) Słota, R.; Broda, M. A.; Dyrda, G.; Ejsmont, K.; Mele, G. Structural and Molecular Characterization of *meso*-substituted Zinc Porphyrins: a DFT Supported Study. *Molecules* **2011**, *16* (12), 9957–9971.

(34) Kadish, K. M.; Caemelbecke, E. V. Electrochemistry of Porphyrins and Related Macrocycles. *J. Solid State Electrochem.* **2003**, *7* (5), 254–258.

(35) Lyaskovskyy, V.; de Bruin, B. Redox Non-innocent Ligands: Versatile New Tools to Control Catalytic Reactions. *ACS Catal.* **2012**, *2* (2), 270–279.

(36) Luca, O. R.; Crabtree, R. H. Redox-active Ligands in Catalysis. *Chem. Soc. Rev.* **2013**, *42* (4), 1440–1459.

(37) Chapman, R. D.; Fleischer, E. B. Direct Measurement of Electron Self-exchange Rates of Cobalt Porphyrins. 1. Outer-sphere Exchange. *J. Am. Chem. Soc.* **1982**, *104* (6), 1575–1582.

CHAPTER 4 VIBRATIONAL STRUCTURAL ANALYSIS OF COBALT FLUORO-PORPHYRIN SURFACE COATINGS VIA GATR-FTIR

Portions of this work are excerpted with permission from:

Preprint of an article published in [*J. Porphyr. Phthalocyanines*, 22, 6, 2018, 461–466]

[DOI: 10.1142/S1088424618500906] © [Copyright World Scientific Publishing Company] [https://www.worldscientific.com/worldscinet/jpp]

4.1 Introduction

One of the structural characterization techniques to analyze chemically modified substrates with a thin layer of molecular species is a grazing angle attenuated total reflectance Fourier transform infrared (GATR-FTIR) spectroscopy that is also a non-destructive and surface-sensitive characterization technique capable of identifying organic and inorganic species, surface functional groups on substrates with relatively high refractive indexes.[1-3] Chapter 4 describes the use of GATR-FTIR spectroscopy for studying chemically modified gallium phosphide (GaP) surfaces containing grafted cobalt(II) porphyrins with 3-fluorophenyl substituents installed at the *meso*-positions of tetrapyrrolic macrocycles. In these hybrid constructs, porphyrin surface attachment is achieved using either a two-step method, involving coordination chemistry of cobalt fluoro-porphyrin metal centers to nitrogen sites on an initially applied thin-film polypyridyl surface coating, or via a direct modification strategy, using a cobalt fluoro-porphyrin precursor bearing a covalently bonded 4-vinylphenyl surface attachment group at a β-position (Figure 4.1).

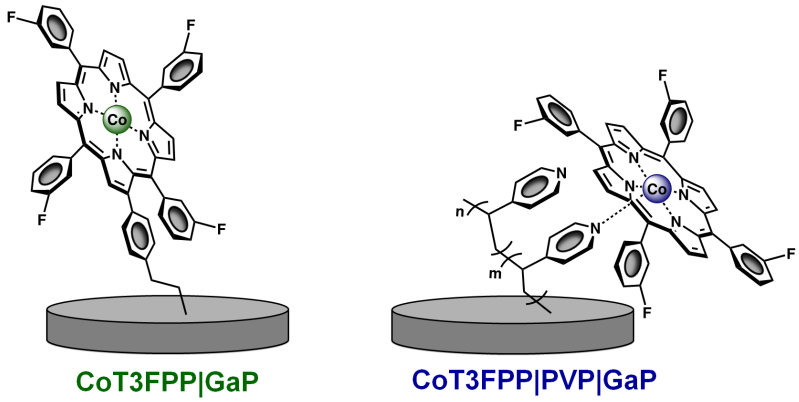

Figure 4.1. Structural representations of cobalt fluoro-porphyrin surface coatings on gallium phosphide.

Both surface-attachment chemistries leverage the UV-induced immobilization of alkenes but result in distinct structural connectivities of the grafted porphyrin units and their associated vibrational spectra. In particular, the in-plane porphyrin deformation vibrational frequency of metalloporphyrin components in samples prepared via coordination to the polymeric interface is characterized by an eight wavenumber shift to higher frequencies compared to that measured on metalloporphyrin-modified surfaces prepared using the one-step attachment method. The more rigid ring structure in the polymeric architecture is consistent with coordination of porphyrin cobalt centers to pyridyl-nitrogen sites on the surface graft. These results demonstrate the use of GATR-FTIR spectroscopy as a sensitive tool for characterizing porphyrin-modified surfaces with absorption signals that are close to the detection limits of many common spectroscopic techniques.

The amplification of signal achieved via GATR-FTIR spectroscopy is due to the grazing angle conditions and resulting enhanced electric field. However, quantitative analysis of surface composition based on absolute FTIR signal intensities, which are sensitive to the pressure of contact between the substrate and sample mount, is limited to relative peak intensity analysis.[4,5]

4.2 Results and Discussion

4.2.1 Materials Preparation

Synthesis

The preparation of porphyrins used in this study, including cobalt(II) 5,10,15,20-tetrakis(3-fluorophenyl)porphyrin (10), cobalt(II) 5,10,15,20-tetrakis(3-fluorophenyl)-2-(4-vinylphenyl)porphyrin (9), cobalt(II) 5,10,15,20-tetra-*p*-tolylporphyrin (3), and

cobalt(II) 5,10,15,20-tetra-*p*-tolyl-2-(4-vinylphenyl)porphyrin (1) (Figure 4.2) were previously described in Chapters 2 and 3.

Sample preparation

The molecular surface coatings used in these studies are composed of cobalt fluoro-porphyrin units immobilized onto gallium phosphide (GaP) substrates via two different methods. The first approach relies on immobilization of cobalt(II) 5,10,15,20-tetrakis(3-fluorophenyl)porphyrin, 10, to a sample of GaP containing an initially applied thin-film polypyridyl coating, PVP|GaP, yielding samples of CoT3FPP|PVP|GaP (Figure 4.2, top). In this method, pyridyl-nitrogen sites on the PVP|GaP surface serve as molecular recognition units to self-assemble cobalt porphyrins along the polymeric interface. The second preparation method involves direct application of a cobalt fluoro-porphyrin complex bearing a 4-vinylphenyl surface attachment group covalently attached at a β-position on the macrocycle, 9.

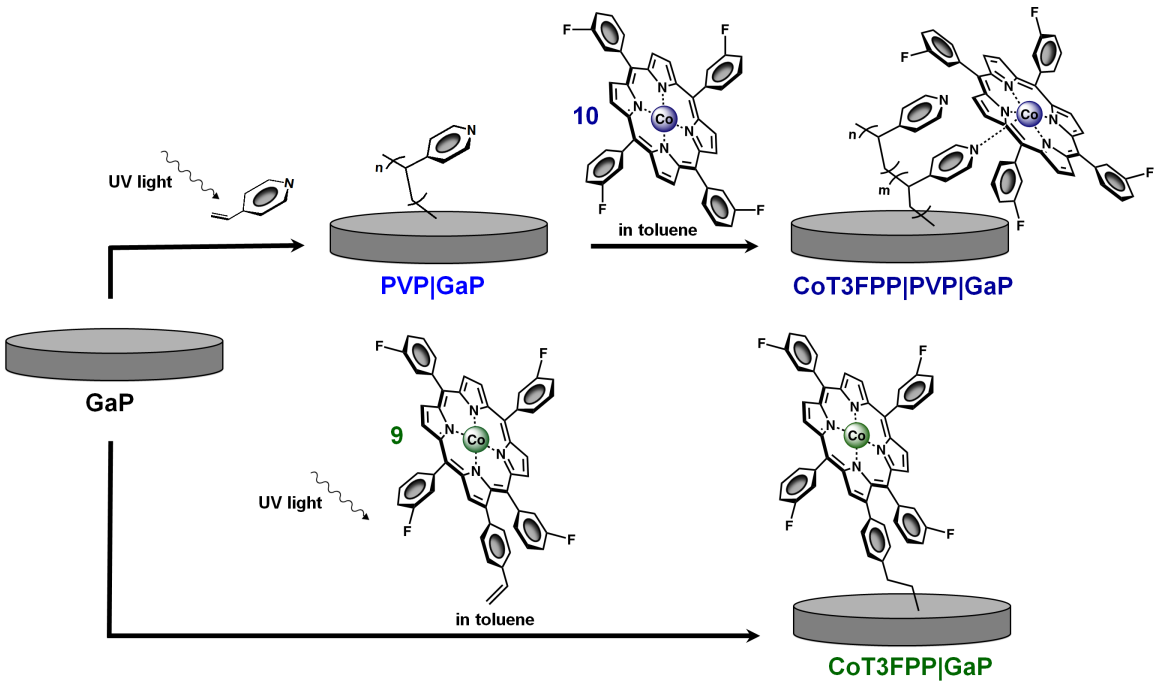

Figure 4.2. Schematic representation depicting the attachment methods, materials, and reagents used to prepare cobalt fluoro-porphyrin surface coatings on gallium phosphide (see main text for details).

Treatment of unmodified-GaP surfaces, GaP, with solutions of this precursor, cobalt(II) 5,10,15,20-tetrakis(3-fluorophenyl)-2-(4-vinylphenyl) porphyrin, 9, in the presence of UV-light yields samples of CoT3FPP|GaP (Figure 4.2, bottom). The surfaces of these two constructs, CoT3FPP|PVP|GaP and CoT3FPP|GaP, possess distinct IR vibrational modes in the range of 980–1740 cm^{-1}, allowing structural analysis and comparison of the cobalt fluoro-porphyrin components in these hybrid architectures.

These surface modification strategies leverage the UV-induced grafting chemistry of olefins to hydroxyl and oxygen-terminated surfaces.[6-9] Modified substrates at each step of surface preparation and functionalization were characterized using X-ray photoelectron

as well as GATR-FTIR spectroscopies. More detailed description of surface modification processes and samples preparations are reported in Chapter 6.

4.2.2 FTIR Characterization

FTIR transmission spectra of the cobalt fluoro-porphyrin molecules used in this work (10 and 9) were collected in a matrix of KBr and are shown in Figure 4.3 (blue and green lines, respectively). For comparisons, spectra of model non-F-containing cobalt porphyrins (3 and 1) are also included in Figure 4.3 (black and red lines, respectively). All four spectra contain similar vibrational features associated with the core porphyrin macrocycles, including bands that can be assigned to C_{β}–H (1170–1078 cm^{-1}), C_m–C_{ph} (1265 cm^{-1}), C_{α}–N and C_{α}–C_{β} (1350–1369 cm^{-1}), as well as C_{β}–C_{β}, C_{α}–C_m, and C=C (1430–1612 cm^{-1}) vibrations.[10-18] It is important to point out that the conjugated ring structure of these complexes likely gives rise to a high degree of vibrational coupling between the various metalloporphyrin modes, thus complicating descriptions of their normal modes. Nonetheless, unlike the transmission spectra of 3 and 1, the spectra of 10 and 9 include strong IR absorption bands located between 1133–1178 cm^{-1} and 1554– 1627 cm^{-1} associated with C–F bond vibrations of the 3-fluorophenyl substituents.[19-22]

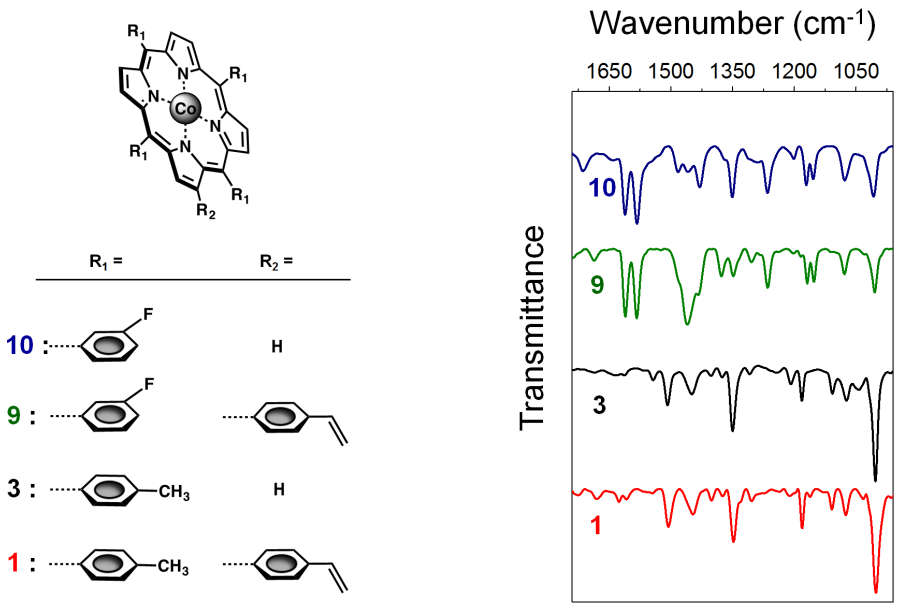

Figure 4.3. Molecular structures of the fluorinated and non-fluorinated model compounds and precursors, including cobalt(II) 5,10,15,20-tetrakis(3-fluorophenyl)porphyrin (10), cobalt(II) 5,10,15,20-tetrakis(3-fluorophenyl)-2-(4-vinylphenyl)porphyrin (9), cobalt(II) 5,10,15,20-tetra-*p*-tolylporphyrin (3), and cobalt(II) 5,10,15,20-tetra-*p*-tolyl-2-(4-vinylphenyl)porphyrin (1) used to assemble CoT3FPP|PVP|GaP, CoT3FPP|GaP, CoP|PVP|GaP, and CoP|GaP, respectively. (right panel) FTIR transmission spectra of 10 (dark blue), 9 (green), 3 (black), and 1 (red) collected in KBr.

Further differences between these four spectra include the vibrational frequency of a metal-sensitive band ascribed to an in-plane cobalt porphyrin deformation, $\nu_{Co\text{-}N}$ (where ν is the vibrational frequency). For samples 10 and 3, this mode is observed at 1007 cm^{-1} or 1003 cm^{-1}, respectively (Table 4.1).

Table 4.1. In-plane Cobalt Porphyrin Deformation Frequencies Measured Using Samples Composed of 10, 9, 3, or 1 in KBr.

$\nu_{Co\text{-}N}$ of the molecular precursors	
Precursor	$\nu_{Co\text{-}N}$ (cm^{-1})
10	1007
9	1005
3	1003
1	1001

In these examples, the 3-fluorophenyl groups at the *meso*-positions of 10 perturb the $\nu_{Co\text{-}N}$, offsetting it to higher values compared to those measured using samples of the non-fluorinated cobalt porphyrin analog, 3. A similar offset ($\Delta\nu_{Co\text{-}N}$) is observed when comparing the $\nu_{Co\text{-}N}$ values measured using samples of the fluorinated and non-fluorinated 4-vinylphenyl containing precursors 9 and 1 (Table 4.1). However, for these compounds (9 and 1) the in-plane cobalt porphyrin deformation vibrational modes appear at slightly lower frequencies compared to the corresponding values measured using samples of 10 and 3, where a proton appears in place of the 4-vinylphenyl surface attachment moiety.

4.2.3 GATR-FTIR Analysis

The GATR-FTIR absorption spectrum of an HF-etched GaP surface is included in Figure 4.4 (black), showing characteristic broad in energy oxide-related absorption bands assigned to OH and PO_x^- surface functional groups[10], centered at 1680 cm^{-1} and 1200 cm^{-1}, as well as a band at 1440 cm^{-1} associated with the presence of adventitious carbon

(CH_x). Conversely, GATR-FTIR spectra of PVP|GaP surfaces are characterized by relatively strong absorption features appearing from 1400–1600 cm^{-1} that are assigned to C–N, C=N, C–H, and CH_2 vibrations of the surface-attached polypyridyl chains (Figure 4.4, blue), confirming successful attachment of the polymeric surface coating, and consistent with previous reports.[23-26] The mode appearing at 1453 cm^{-1} is particularly diagnostic of the planar deformation vibration of CH_2 groups in polymeric chains. For example, this mode is observed in samples of polyvinylpyridine and polystyrene but is not present in spectra of 4-vinylpyridine and styrene monomers.[27] GATR-FTIR absorption spectra of CoT3FPP|PVP|GaP surfaces (Figure 4.4, dark blue) show several vibrational features associated with the presence of cobalt fluoro-porphyrin species, including modes associated with C_β–H (1068–1174 cm^{-1}), C_m–C_{ph} (1263 cm^{-1}), C_α–N and C_α–C_β (1310–1378 cm^{-1}), as well as C_β–C_β, C_α–C_m, and C=C (1508–1643 cm^{-1}) vibrations that appear at values nearly identical to those recorded using samples of the associated molecular precursor 10 in KBr. In addition, several absorption features appearing in the 1400–1600 cm^{-1} region on surfaces of CoT3FPP|PVP|GaP are assigned to vibrational modes associated with polypyridyl units. However, contributions associated with porphyrin ring-based modes also appear in this spectral region, complicating a detailed analysis and assignment of all features. Nonetheless, the in-plane metalloporphyrin deformation vibrational modes, appearing between 1000–1019 cm^{-1}, are exquisitely sensitive to both the elemental nature of the metal center and its local coordination environment.[28-30] Thus, they are also sensitive to the nature of the chemical attachment strategies used in this report to assemble cobalt fluoro-porphyrin-modified GaP surfaces.

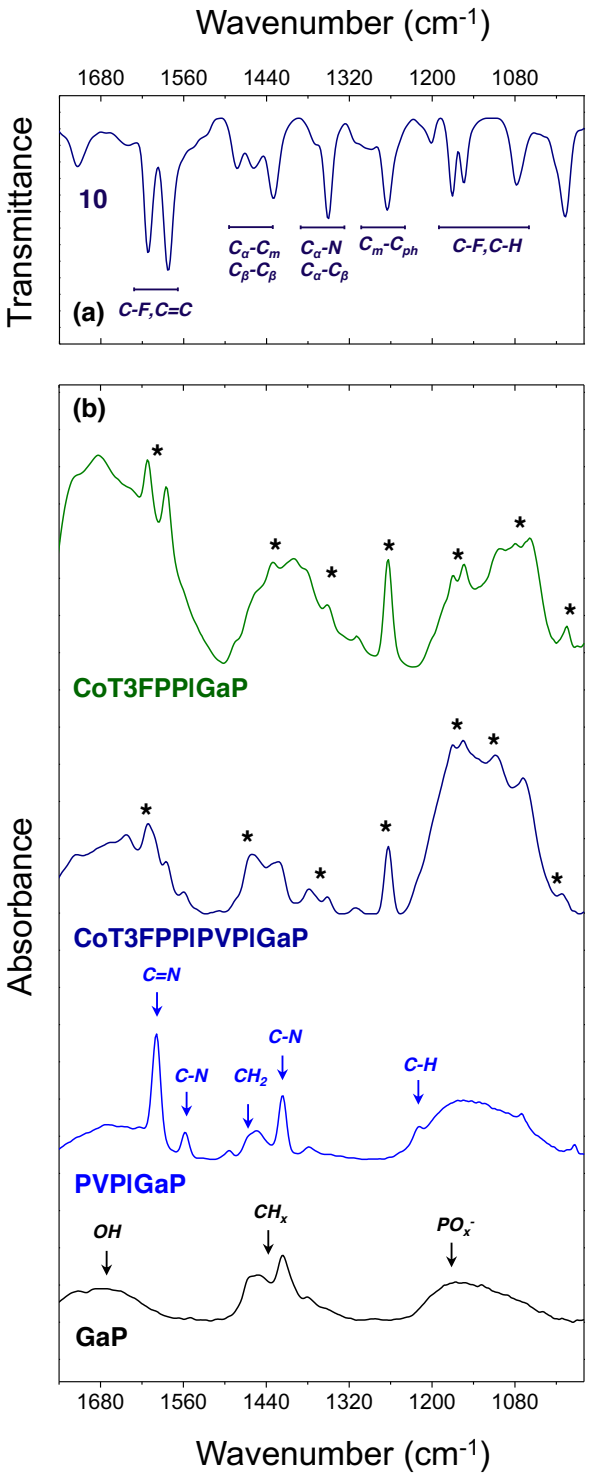

Figure 4.4. (a) FTIR transmission spectrum of 10 collected in KBr, included to facilitate comparisons, as well as (b) GATR-FTIR absorption spectra collected using samples of

GaP (black), PVP|GaP (blue), CoT3FPP|PVP|GaP (dark blue), and CoT3FPP|GaP (green). Surface vibrational modes associated with immobilized cobalt fluoro-porphyrin species are labeled with *.

As previously reported for chemically-modified surfaces composed of non-fluorinated cobalt porphyrin, 3, assembled onto polypyridyl functionalized gallium phosphide substrates, forming CoP|PVP|GaP[25], attachment of porphyrin cobalt centers to surface-grafted pyridyl-nitrogen sites results in a change of the porphyrin's original four-coordinate square planar environment and a diagnostic shift of the in-plane cobalt porphyrin deformation vibration to higher frequencies ($\Delta\nu_{Co\text{-}N} \sim 6$ cm^{-1}).

For the F-containing cobalt porphyrins described in this report, coordination to the surface-grafted pyridyl units gives rise to a similar offset ($\Delta\nu_{Co\text{-}N} \sim 6$ cm^{-1}) of the vibrational frequencies associated with the cobalt fluoro-porphyrin deformation modes (Tables 4.1 and 4.2).

In addition, features arising from C–F bond vibrations are observed at 1155–1171 cm^{-1} and 1585–1643 cm^{-1} on CoT3FPP|PVP|GaP samples, providing further evidence of successful intact fluoro-porphyrin incorporation on these surfaces.

GATR-FTIR analysis of CoT3FPP|GaP samples, prepared using the direct attachment method, also show the presence of surface vibrational modes characteristic of cobalt fluoro-porphyrins, including those with frequencies ascribed to C_β–H (1059–1080 cm^{-1}), C_m–C_{ph} (1263 cm^{-1}), C_α–N and C_α–C_β (1309–1400 cm^{-1}), C_β–C_β, C_α–C_m, C=C (1431– 1612 cm^{-1}), and C–F (1153–1167 cm^{-1} and 1585 cm^{-1}) vibrations (Figure 4.4, green). Yet as anticipated, the $\nu_{Co\text{-}N}$ measured on surfaces of CoT3FPP|GaP samples appears at 1005 cm^{-1}, a value that is unperturbed compared to the $\nu_{Co\text{-}N}$ measured using

samples of the non-surface immobilized fluoro-porphyrin precursor complex, 9, and eight wave-numbers lower in frequency than those measured on surfaces of CoT3FPP|PVP|GaP (Figure 4.5).

Table 4.2. In-plane Cobalt Porphyrin Deformation Frequencies Measured on Surfaces of CoT3FPP|PVP|GaP, CoT3FPP|GaP, CoP|PVP|GaP, and CoP|GaP.

* Values have been previously reported[25, 31]

$\nu_{Co\text{-}N}$ on molecular modified surfaces	
Construct	$\nu_{Co\text{-}N}$ (cm^{-1})
CoT3FPP|PVP|GaP	1012
CoT3FPP|GaP	1005
CoP|PVP|GaP*	1009
CoP|GaP*	1001

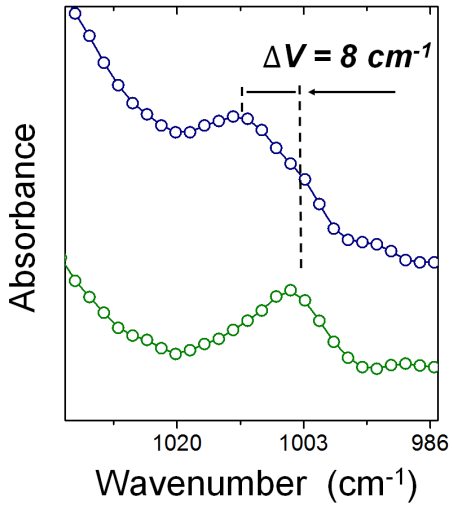

Figure 4.5. GATR-FTIR absorption spectra of CoT3FPP|GaP (green) and CoT3FPP|PVP|GaP (dark blue) samples showing an eight wavenumbers difference in vibrational frequency of the in-plane metalloporphyrin deformation mode.

This similarity of the in-plane cobalt porphyrin deformation vibrational frequencies measured on surfaces of CoT3FPP|GaP and samples of 9 is consistent with previous reports[31] describing a non-fluorinated cobalt porphyrin-modified construct CoP|GaP, where the $\nu_{Co\text{-}N}$ is observed at 1001 cm^{-1} on surfaces of these samples and is identical to the $\nu_{Co\text{-}N}$ measured using samples of the non-fluorinated cobalt porphyrin precursor, 1. For the fluorinated porphyrin samples 10 and 9, the relatively higher frequency in-plane metalloporphyrin deformations compared to those measured using samples of the non-fluorinated complexes 3 or 1 (Table 4.1), indicate a more rigid ring structure for the F-containing congeners.

4.2.4 XP Spectroscopy Studies

In addition to the structural information provided by IR-spectral analysis of the cobalt fluoro-porphyrin-modified GaP constructs CoT3FPP|GaP and CoT3FPP|PVP|GaP, XP

spectroscopy confirms the presence of cobalt species on the surface and provides further information on the oxidation state of the metal centers (Figure 4.6). In particular, high-energy resolution Co $2p_{3/2}$ core level spectra of CoT3FPP|GaP and CoT3FPP|PVP|GaP samples show a single peak centered at 781.2 eV and 781.0 eV, respectively, with a satellite feature at higher binding energies. These results are consistent with the presence of surface-immobilized cobalt species that are predominately in a +2 oxidation state.[20,32- 34]

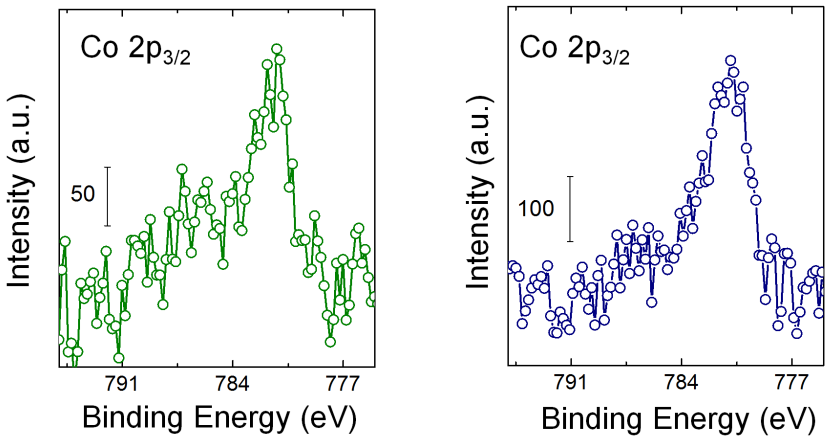

Figure 4.6. High-energy resolution core level XP spectra of the Co $2p_{3/2}$ region recorded using samples of CoT3FPP|GaP (green) and CoT3FPP|PVP|GaP (dark blue).

4.3 Conclusions

Hybrid materials consisting of gallium phosphide semiconductors chemically modified with cobalt fluoro-porphyrins were prepared via two methods: 1) coordination of fluoro-porphyrin cobalt centers to an initially applied polymeric interface and 2) direct attachment of cobalt fluoro-porphyrins containing covalently attached 4-vinylphenyl functional groups. Structural analysis of the resulting constructs using GATR-FTIR and XP spectroscopies confirms the presence of intact cobalt fluoro-porphyrin species on

these surfaces. In addition, FTIR analysis provides a technique for measuring in-plane metalloporphyrin deformation vibrational frequencies, which can be used as a diagnostic spectroscopic handle for characterizing the binding environments of surface-immobilized porphyrins. In particular the frequency of the in-plane cobalt porphyrin deformation vibration measured on surfaces of CoT3FPP|PVP|GaP is eight wavenumbers higher than that measured on surfaces of CoT3FPP|GaP, indicating a more rigid ring structure in these assemblies that is consistent with coordination of cobalt porphyrin metallocenters to pyridyl-nitrogen sites on the PVP surface coating. The concepts described here highlight the sensitivity and non-destructive nature of GATR-FTIR as a tool for analyzing thin-film surface coatings and grafted molecular species, providing spectroscopic information that is not typically obtainable using more traditional infrared-based techniques.

4.4 References

(1) Milosevic, M; Milosevic, V.; Berets, S.L. Grazing Angle Attenuated Total Reflection Spectroscopy: Fields at the Interface and Source of the Enhancement. *Appl. Spectrosc.* **2007**, *61*, 530–536.

(2) Milosevic, M. Internal Reflection and ATR Spectroscopy. *Applied Spectroscopy Reviews* **2004**, *39* (3), 365−384.

(3) Mulcahy, M. E.; Berets, S. L.; Milosevic, M.; Michl, J. Enhanced Sensitivity in Single-reflection Spectroscopy of Organic Monolayers on Metal Substrates (Pseudo-ATR). *J. Phys. Chem. B* **2004**, *108* (5), 1529–1521.

(4) O'Leary, L. E.; Johansson, E.; Brunschwig, B.S.; Lewis, N.S. Synthesis and Characterization of Mixed Methyl/Allyl Monolayers on Si(111). *J. Phys. Chem. B* **2010**, *114* (45), 14298–14302.

(5) Johansson, E.; Hurley, P. T.; Brunschwig, B. S.; Lewis, N. S. Infrared Vibrational Spectroscopy of Isotopically Labeled Ethyl-Terminated Si(111) Surfaces Prepared Using a Two-Step Chlorination/Alkylation Procedure. *J. Phys. Chem. B* **2009**, *113* (34), 15239–152455.

(6) Lummerstorfer, T.; Hoffmann, H. IR Reflection Spectra of Monolayer Films Sandwiched between Two High Refractive Index Materials. *Langmuir* **2004**, *20* (16), 6542–6545.

(7) Lummerstorfer, T.; Hoffmann, H. Click Chemistry on Surfaces: 1,3-Dipolar Cycloaddition Reactions of Azide-Terminated Monolayers on Silica. *J. Phys. Chem. B* **2004**, *108* (13), 3963–3966

(8) Lummerstorfer, T.; Kattner, J.; Hoffmann, H. Monolayers at Solid–solid Interfaces Probed with Infrared Spectroscopy. *Anal. Bioanal. Chem.* **2007**, *388* (1), 55–64.

(9) Wadsworth, B. L.; Beiler, A. M.; Khusnutdinova, D.; Jacob, S. I.; Moore, G. F. Electrocatalytic and Optical Properties of Cobaloxime Catalysts Immobilized at a Surface-Grafted Polymer Interface. *ACS Catal.* **2016**, *6* (12), 8048–8057.

(10) Allara, D.; Stapleton, J. *Chapter 3*, *Springer Series in Surface Science* **2013**.

(11) Zhang, Z.; Hou, S.; Zhu, Z.; Liu, Z. Preparation and Characterization of a Porphyrin Self-Assembled Monolayer with a Controlled Orientation on Gold. *Langmuir* **2000**, *16* (2), 537−540.

(12) Şen, P.; Hirel, C.; Andraud, C.; Aronica, C.; Bretonnière, Y.; Mohammed, A.; Ågren, H.; Minaev, B.; Minaeva, V.; Baryshnikov, G.; Lee, H.-H.; Duboisset, J.; Lindgren, M. Fluorescence and FTIR Spectra Analysis of Trans-A_2B_2-Substituted Di- and Tetra-Phenyl Porphyrins. *Materials* **2010**, *3* (8), 4446−4475.

(13) Alben, J. O.; Choi, S. S.; Adler, A. D.; Caughey, W. S. Infrared Spectroscopy of Porphyrins. *Ann. N. Y. Acad. Sci.* **1973**, 206 (1), 278–295.

(14) Li, X.-Y.; Czernuszewicz, R. S.; Kincaid, J. R.; Spiro, T. G. Consistent Porphyrin Force Field. 3. Out-of-plane Modes in the Resonance Raman Spectra of Planar and Ruffled Nickel Octaethylporphyrin. *J. Am. Chem. Soc.* **1989**, *111* (18), 7012–7023.

(15) Nazeeruddin, M. K.; Humphry-Baker, R.; Officer, D. L.; Campbell, W. M.; Burrell, A. K.; Grätzel, M. Application of Metalloporphyrins in Nanocrystalline Dye-Sensitized Solar Cells for Conversion of Sunlight into Electricity. *Langmuir* **2004**, *20* (15), 6514–6517.

(16) Zhang, Y.-H.; Chen, D.-M.; He, T.; Liu, F.-C. Raman and Infrared Spectral Study of *meso*-Sulfonatophenyl Substituted Porphyrins ($TPPS_n$, n=1, 2A, 2O, 3, 4). *Spectrochimica Acta Part A* **2003**, *59* (1), 87–101.

(17) Thomas, D. W.; Martell, A. E. Metal Chelates of Tetraphenylporphine and Some p-Substituted Derivatives[1,2]. *J. Am. Chem. Soc.* **1959**, *81* (19), 5111–5119.

(18) Rush III, T. S.; Kozlowski, P. M.; Piffat, C. A.; Kumble, R.; Zgierski, M.; Spiro, T. G. Computational Modeling of Metalloporphyrin Structure and Vibrational Spectra: Porphyrin Ruffling in NiTPP. *J. Phys. Chem. B* **2000**, *104* (20), 5020–5034.

(19) Nguyen, K.; Day, P. N.; Pachter, R. Effects of Halogenation on the Ionized and Excited States of Free-base and Zinc Porphyrins. *J. Chem. Phys.* **1999**, *110*, 9135–9144.

(20) Słota, R.; Broda, M. A.; Dyrda, G.; Ejsmont, K.; Mele, G. Structural and Molecular Characterization of *meso*-substituted Zinc Porphyrins: a DFT Supported Study. *Molecules* **2011**, *16* (12), 9957–9971.

(21) Sun, H.; Smirnov, V.; DiMagno, S. G. Slow Electron Transfer Rates for Fluorinated Cobalt Porphyrins: Electronic and Conformational Factors Modulating Metalloporphyrin ET. *Inorg. Chem.* **2003**, *42* (19), 6032–6040.

(22) Narasimham, N. A.; Nielsen, J. R.; Theimer, R. Vibrational Spectra of Fluorinated Aromatics. XIII. Benzotrifluoride. *J. Chem. Phys.* **1957**, *27*, 740−745.

(23) Beiler, A. M.; Khusnutdinova, D.; Jacob, S. I.; Moore, G. F. Chemistry at the Interface: Polymer-Functionalized GaP Semiconductors for Solar Hydrogen Production. *Ind. Eng. Chem. Res.* **2016**, *55* (18), 5306–5314.

(24) Beiler, A. M.; Khusnutdinova, D.; Jacob, S. I.; Moore, G. F. Solar Hydrogen Production Using Molecular Catalysts Immobilized on Gallium Phosphide (111)A and (111)B Polymer-Modified Photocathodes. *ACS Appl. Mater. Interfaces* **2016**, *8* (15), 10038–10047.

(25) Beiler, A. M.; Khusnutdinova, D.; Wadsworth, B. L.; Moore, G. F. Cobalt Porphyrin-Polypyridyl Surface Coatings for Photoelectrosynthetic Hydrogen Production. *Inorg. Chem.* **2017**, *56* (20), 12178–12185.

(26) Krawicz, A.; Yang, J.; Anzenberg, E.; Yano, J.; Sharp, I. D.; Moore, G. F. Photofunctional Construct That Interfaces Molecular Cobalt-Based Catalysts for H2 Production to a Visible-Light-Absorbing Semiconductor. *J. Am. Chem. Soc.* **2013**, *135* (32), 11861–11868.

(27) Panov, V. P.; Kazarin, L. A.; Dubrovin, V. I.; Gusev, V. V.; Kirsh, Y. E. Infrared Spectra of Atactic Poly(4-vinylpyridine). *Zh. Prikl. Spektrosk* **1974**, *21*, 862−869.

(28) Bar-Ilan, A.; Manassen, J. Heterogeneous and homogeneous catalysis by substituted cobalt tetraphenylporphyrins, and correlations with IR spectra. *Journal of Catalysis* **1974**, *33* (1), 68−73.

(29) Boucher, L. J.; Katz, J. J. The Infrared Spectra of Metalloporphyrins (4000–160 cm $^{-1}$). *J. Am. Chem. Soc.* **1967**, *89* (6), 1340–1345.

(30) Kincaid, J.; Nakamoto, K. Vibrational Spectra of Transition Metal Complexes of Tetraphenylporphine. *J. Inorg. Nucl. Chem*. **1975**, *37* (1), 85–89.

(31) Khusnutdinova, D.; Beiler, A. M.; Wadsworth B. L.; Jacob S. I.; Moore G. F. Metalloporphyrin-modified Semiconductors for Solar Fuel Production. *Chem. Sci.* **2017**, *8* (1), 253–259.

(32) Borod'Ko, Y. G.; Vetchinkin, S. I.; Zimont, S. L.; Ivleva, I. N.; Shul'Ga, Y. M. Nature of Satellites in X-ray Photoelectron Spectra XPS of Paramagnetic Cobalt (II) Compounds. *Chem. Phys. Lett.* **1976**, *42* (2), 264−267.

(33) Chuang, T. J.; Brundle, C. R.; Rice, D. W. Interpretation of the X-Ray Photoemission Spectra of Cobalt Oxides and Cobalt Oxide Surfaces. *Surf. Sci.* **1976**, *59* (2), 413–429.

(34) Dillard, J. G.; Schenck, C. V.; Koppelman., M. H. Surface Chemistry of Cobalt in Calcined Cobalt-Kaolinite Materials.". *Clays Clay Miner.* **1983**, *31* (1), 69–72.

CHAPTER 5 BINUCLEAR COPPER FUSED PORPHYRINS FOR ELECTROCATALYTIC HYDROGEN EVOLUTION REACTION

Portions of this work are excerpted with permission from:

Khusnutdinova, D.*; Wadsworth, B. L.*; Flores, M.; Beiler, A. M.; Reyes Cruz E. A; Zenkov Y.; Moore, G. F. *ACS Catal.* **2018**, *8* (10), 9888–9898.

My contribution to this work has resulted in synthesis and characterization of all the compounds reported in this study, electrochemical as well as IR and UV-vis measurements, determining the thermodynamic potential of H^+/H_2 reaction in dichloromethane.

5.1 Introduction

In this chapter binuclear copper porphyrins in which two copper porphyrin macrocycles are doubly fused at the *meso*-β positions are shown to be active electrocatalysts for the hydrogen evolution reaction ($2H^+ + 2e^- \rightarrow H_2$). Structural characterization, including use of electron paramagnetic resonance and x-ray photoelectron spectroscopies, verifies the fused species contains two copper(II) metal centers in its resting state. In comparison to the non-fused copper(II) porphyrin complex (Figure 5.1), the fused species is reduced at significantly less applied bias potentials ($\Delta E_{½} \sim 570$ mV for the first reduction process). Electrochemical characterization in the presence of substrate protons confirms the production of hydrogen with near-unity Faradaic efficiency, and kinetic analysis shows the catalyst achieves a maximum turnover frequency above 2,000,000 s^{-1}. The enhancement in catalytic performance over analogous non-fused copper(II) porphyrins indicates extended macrocycles provide a structural motif and design element for preparing electrocatalysts that activate small molecules consequence to renewable energy.

Structural characterization of the fused bimetallic copper(II) porphyrin used in this report includes the use of electron paramagnetic resonance (EPR) and x-ray photoelectron (XP) spectroscopies, as well as Fourier-transform infrared (FTIR) and ultraviolet-visible (UV-Vis) spectroscopies coupled with electrochemical techniques, all of which have never been reported for this complex. In particular, infrared spectroelectrochemistry (IR-SEC) is used to provide information on bonding changes following reduction of the fused porphyrin macrocycle, and electrochemical methods are used to study the kinetic and thermodynamic parameters governing catalytic performance in non-aqueous solutions using trifluoroacetic acid as a proton source. The latter experiments are performed at

solution concentrations and scan rates that allow access to pure kinetic, no substrate depletion conditions, i.e., where the fraction of activated catalysts at the electrode surface is near unity, and the substrate concentration at the electrode surface is approximately equal to the bulk concentration. This is commonly referred to as S-shaped wave conditions, alluding to the form of the resulting voltammogram.[1-4] Under these conditions, the plateau current of the cyclic voltammogram's S-shaped wave can be used to calculate an observed rate constant, which is the maximum turnover frequency of the catalyst.

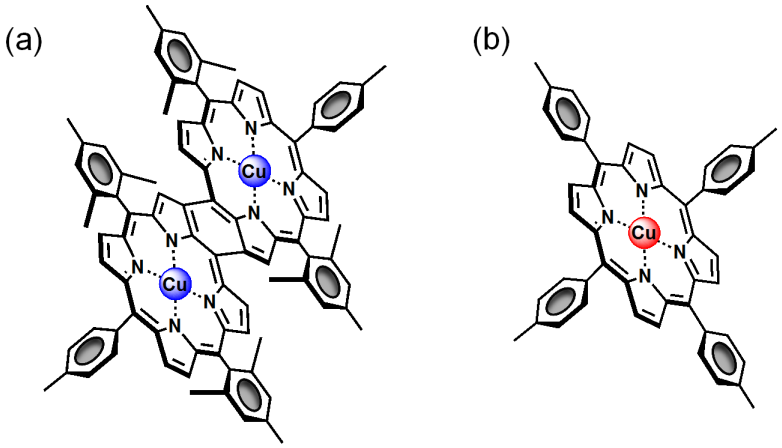

Figure 5.1. Molecular structures of (a) copper fused porphyrin, Cu_2FP, and (b) non-fused monomeric copper porphyrin, CuP.

5.2 Results and Discussion

5.2.1 Materials Preparation

Synthesis

The detailed procedures of synthesizing molecular complexes used in this study that include the fused bicopper(II) *meso*-β doubly-fused 5,24-di(*p*-tolyl)-10,19,29,38-tetramesitylporphyrin (Cu_2FP), non-fused monomeric copper(II) porphyrin, copper(II)

5,10,15,20-tetra-*p*-tolylporphyrin (CuP), free-base *meso*-β doubly-fused 5,24-di(*p*-tolyl)-10,19,29,38-tetramesitylporphyrin (FBFP), and free-base 5,10,15,20-tetra-*p*-tolylporphyrin (TTP) are included in Chapter 6.

5.2.2 Structural Characterization

To better understand the resting state electronic structure of the Cu_2FP used in this report, EPR and XP spectroscopic studies were undertaken. Figure 5.2 (red) depicts the X-band (9.44 GHz) EPR spectrum of CuP in dichloromethane at 30 K.

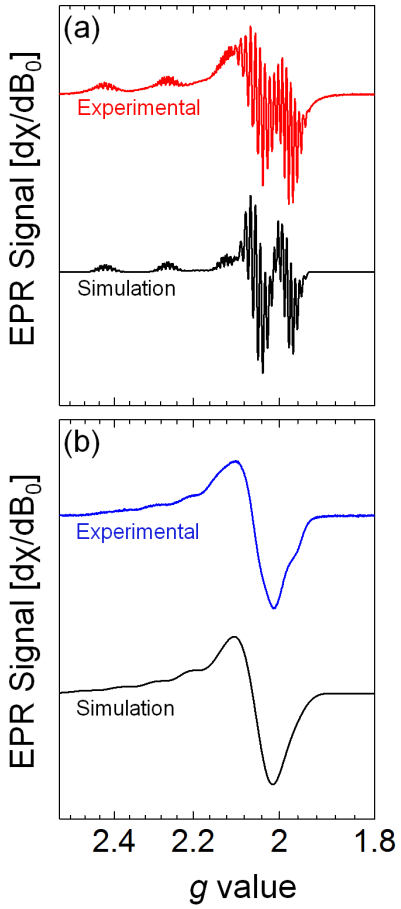

Figure 5.2. Experimental (red or blue) and simulated (black) X-band (9.44 GHz) EPR spectra of (a) CuP and (b) Cu_2FP collected in dichloromethane at 30 K or 40 K respectively.

The observed spectral features are consistent with the presence of a single Cu(II) species,[5-11] i.e., a broad signal containing multiline patterns due to hyperfine coupling (hfc) interactions between the magnetic moment of the unpaired electron and the magnetic moments of neighboring nuclei, including a four-line splitting due to the hfc interaction with the ^{63}Cu (I = 3/2) nucleus.

To obtain the EPR parameters, the respective spin Hamiltonian (see Chapter 6 for more details) was fit to the data (Figure 5.2, black). The spectral features observed for CuP were well-fit considering a single Cu(II) center (S = 1/2) with a *g*-tensor having an axial pattern,[12] *i.e.*, $g_x = g_y = g_\perp = 2.049$ and $g_z = g_\parallel = 2.190$, and axial hfc interactions with one ^{63}Cu (I = 3/2), four equivalent ^{14}N (I = 1), and one ^{1}H (I = 1/2). The fit parameters are summarized in Table 5.1. Figure 5.2 (blue) shows the X-band EPR spectrum of Cu_2FP in dichloromethane at 40 K, displaying a multiline pattern similar to one previously associated with ^{63}Cu hfc interactions corresponding to dimers of copper(II) uroporphyrin III molecules.[6] Thus, the best fit of the EPR spectrum of Cu_2FP was obtained considering two equivalent Cu(II) centers (S = 1/2) with rhombic *g*-values ($g_x = 2.021$, $g_y = 2.077$, and $g_z = g_\parallel = 2.210$) and axial hfc interactions with two equivalent ^{63}Cu (I = 3/2) nuclei (Figure 5.2, black, and Table 5.1). The EPR parameters obtained for CuP and Cu_2FP provide additional details on the electronic structures of the bound Cu(II) centers, including differences resulting from the binding characteristics and chemical nature of the porphyrin ligands in these complexes. In particular, the *g*-tensor represents a measure of the integral properties of Cu(II) and its ligands. The *g*-tensor obtained for CuP, as expected, has axial symmetry with values similar to those previously reported for copper tetraphenylporphyrin chelates and cupric protoporphyrin IX dimethyl ester (Table 5.1).[7,10] The electron-nuclear hfc interaction also provides information on the local

electronic properties of the Cu(II) complex, i.e., the electron spin density distribution. In this case, the parameter $A_{\|}^{Cui}$represents an indirect measure of the electron spin density at the Cu(II) nucleus and the values of $g_{//}$ and $A_{\|}^{Cui}$ obtained for CuP indicate that Cu(II) is coordinated to the porphyrin via four nitrogens in a square planar geometry (Table 5.1).[13] Additional supporting evidence of this geometry arises from the nine-line splitting, due to the hfc between the unpaired electron and four equivalent nitrogen atoms, observed in the EPR spectrum of CuP. By contrast, the *g*-tensor obtained for Cu_2FP has a rhombic pattern and the value of $A_{\|}^{Cui}$ (0.0113 cm^{-1}) is smaller than the one measured for the monomeric Cu(II) porphyrin (0.0203 cm^{-1}). The rhombic distortion of the *g*-values indicates the delocalization of the two unpaired electrons, carried by Cu_2FP, extends beyond a single porphyrin unit of the fused complex. Furthermore, the lower value of $A_{\|}^{Cui}$ obtained for Cu_2FP shows the two unpaired electrons in the fused copper(II) porphyrins, are shared between the two porphyrin molecules. The line broadening of the EPR spectrum of Cu_2FP is also considerably larger than that observed in the EPR spectrum of CuP (Figure 5.2) and this difference in line broadening is primarily ascribed to weak exchange spin-spin interactions (isotropic and dipolar) between the two Cu(II) centers of Cu_2FP.[14, 15]

Table 5.1 Parameters Used to Fit the EPR Spectra of CuP and Cu_2FP Complexes at Low Temperature.

Parameter [a]	CuP T = 30 K	Cu_2FP T = 40 K
g_x	2.049	2.021
g_y	2.049	2.077
$g_{\parallel}$	2.190	2.210
$g_{\perp}$ [b]	2.049	2.049
ΔB_x (MHz)	40	280
ΔB_y (MHz)	40	300
ΔB_z (MHz)	12	304
$A_x^{Cu_i}$ (cm^{-1})	< 0.0013	< 0.0100
$A_y^{Cu_i}$ (cm^{-1})	< 0.0013	< 0.0100
$A_{\parallel}^{Cu_i}$ (cm^{-1})	0.0203	0.0113
$A_x^{N_j}$ (cm^{-1})	0.0017	- [c]
$A_y^{N_j}$ (cm^{-1})	0.0017	-
$A_{\parallel}^{N_j}$ (cm^{-1})	0.0014	-
A_x^{H} (cm^{-1})	< 0.0013	-
A_x^{H} (cm^{-1})	< 0.0013	-
$A_{\parallel}^{H}$ (cm^{-1})	0.0006	-

[a] The fitting parameters were the three *g*-values The fitting parameters were the three *g*-values, g_x, g_y, and $g_\parallel$, where $g_\parallel$ is defined as g_z, the three line widths ΔB_x, ΔB_y, and ΔB_z, and the hfc tensor components, $A_x^{Cu_i}$, $A_y^{Cu_i}$, $A_\parallel^{Cu_i}$, A_x^{Nj}, A_y^{Nj}, $A_\parallel^{Nj}$, and A_x^{H}, A_y^{H}, $A_\parallel^{H}$; where $A_\parallel^{Cu_i}$, $A_\parallel^{Nj}$, and $A_\parallel^{H}$ are defined as $A_z^{Cu_i}$, A_z^{Nj}, and A_z^{H}, respectively. For CuP, $A_x^{Cu_i}$, $A_y^{Cu_i}$, $A_\parallel^{Cu_i}$ and A_x^{Nj}, A_y^{Nj}, $A_\parallel^{Nj}$ are the hfc's of a single ^{63}Cu and four equivalent ^{14}N, respectively. For Cu_2FP $A_x^{Cu_i}$, $A_y^{Cu_i}$, $A_\parallel^{Cu_i}$ are the hfc's of two equivalent ^{63}Cu $g_\perp$ was calculated as $[(g_x^2 + g_y^2)/2]^{1/2}$

[c] Not resolved in the spectrum.

XP spectroscopic measurements, including analysis of the high-resolution copper 2p region, provide additional confirmation that both metal centers of the fused porphyrin are in the +2 oxidation state (Figure 5.3).

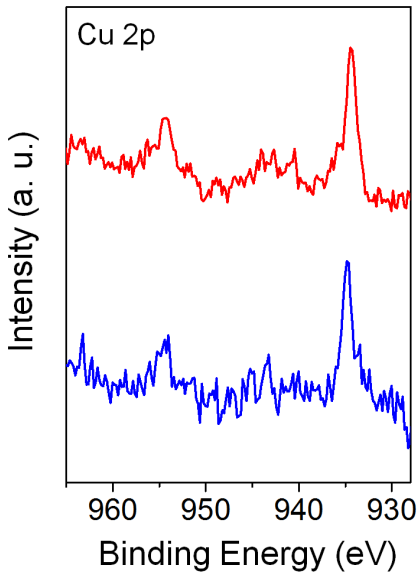

Figure 5.3. High-energy resolution core level XP spectra of Cu 2p region recorded using samples of Cu_2FP (blue) or CuP (red) dropcasted onto a glassy carbon disk.

5.2.3 Electrochemical Studies

Further information on the electronic properties of Cu_2FP is obtained from electrochemical analysis. Cyclic voltammograms recorded at scan rates ranging from 50-500 mV s^{-1} using Cu_2FP dissolved in 0.1 M tetrabutylammonium hexafluorophosphate ($TBAPF_6$) dichloromethane solutions show the presence of two quasi-reversible redox features with midpoint potentials ($^{I}E_{1/2}$ and $^{II}E_{1/2}$) equal to -1.27 and -1.53 volts versus the ferrocenium/ferrocene (V vs Fc^+/Fc) redox couple (Figures 5.4). These results are in stark contrast to those obtained using solutions of CuP in dichloromethane, where under otherwise similar experimental conditions a single quasi-reversible redox feature is observed at a potential that is significantly more negative [$^{I}E_{½}$ = -1.84 V vs Fc^+/Fc, with shifts ($\Delta^{I}E_{½}$ and $\Delta^{II}E_{½}$) of 570 and 310 mV with respect to the first or second reduction feature of Cu_2FP, respectively] (Tables 5.2).

Table 5.2 Midpoint Potentials for the Reduction and Oxidation of CuP and Cu_2FP Complexes as Determined by Cyclic Voltammetry in Dichloromethane.

Compound	^{III}E (V vs Fc^+/Fc)			
	^{II}E (ΔE_p, mV)	^{I}E (ΔE_p, mV)	^{ii}E (ΔE_p, mV)	^{i}E (ΔE_p, mV)
Cu_2FP	-1.53 (105)	-1.27 (102)	+0.27 (69)	+0.56 (77)
CuP	N/A	-1.84 (92)	+0.44 (90)	+0.85 (96)

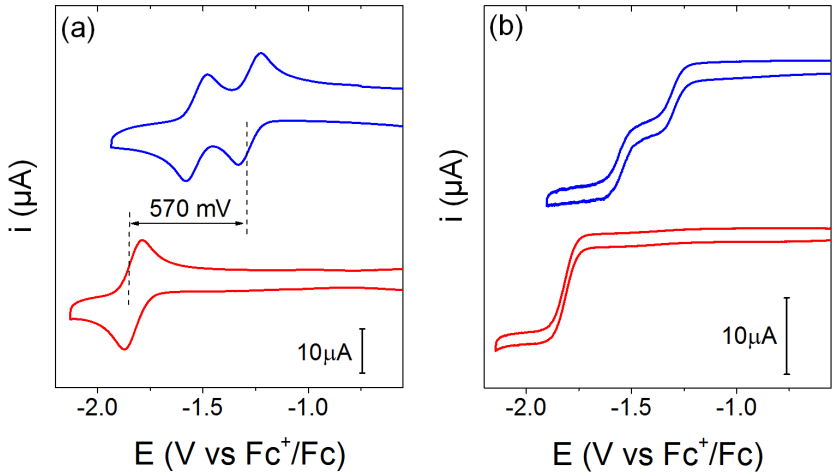

Figure 5.4. Cyclic voltammograms of Cu_2FP (blue) and CuP (red) recorded in a 0.1 M tetrabutylammonium hexafluorophosphate dichloromethane solution using a 3 mm diameter glassy carbon electrode and a scan rate of 500 mV s^{-1} under (a) non-rotating conditions and 0.34 mM in porphyrin and (b) rotating (1000 RPM) conditions and 0.1 mM in porphyrin.

This difference in redox potentials between fused and monomeric porphyrin species is attributed to enhanced electronic delocalization resulting from the extended aromaticity of fused architectures.[16-21] Differential pulse voltammetry experiments performed using equimolar concentrations of Cu_2FP or CuP show the amount of charge passed for each reductive wave of Cu_2FP and CuP are approximately equal (Figure 5.5). Given the single reduction feature observed for CuP can be attributed to a one-electron process, and the interfacial rates of electron transfer from the electrode surface to the complexes dissolved in solution are approximately equal, the two reduction events observed for Cu_2FP are assigned as two separate one-electron reduction processes, i.e., $Cu_2FP + e^- \rightarrow Cu_2FP^{1-}$ and $Cu_2FP^{1-} + e^- \rightarrow Cu_2FP^{2-}$. Distinguishing ligand-based reductions from those that are

metal-centered can be difficult, and reductive processes of metalloporphyrins have been ascribed to both innocent and non-innocent ligand chemistry.[22-26]

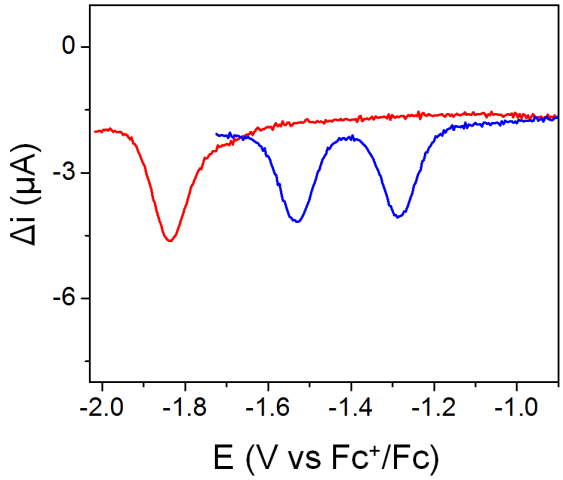

Figure 5.5. Differential pulse voltammetry data recorded using Cu_2FP (0.1 mM) (blue) or CuP (0.1 mM) (red) in a 0.1 M $TBAPF_6$ dichloromethane solution under argon. All measurements were recorded using a 3 mm diameter glassy carbon working electrode at room temperature and the ferrocenium/ferrocene redox couple as an internal reference.

5.2.4 UV-Vis-NIR-SEC and IR-SEC Measurements

Nonetheless, the use of UV-Vis-NIR and infrared spectroelectrochemistry (UV-Vis-NIR-SEC and IR-SEC) permits comparison of the changes in electronic and vibrational structure following reduction of the monomeric or fused copper(II) porphyrin macrocycles. The absorption spectrum of Cu_2FP is significantly altered as compared to the spectrum of CuP (Figure 5.6).

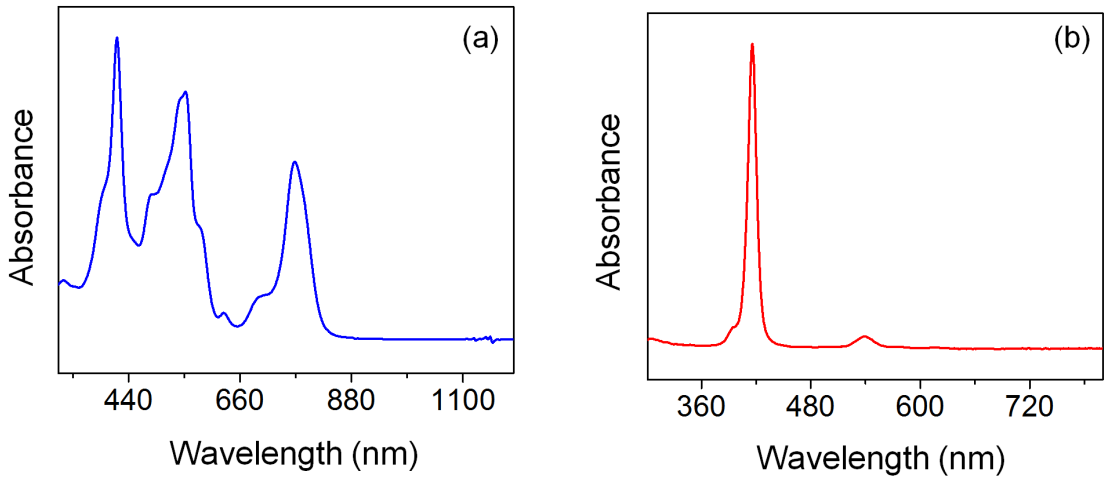

Figure 5.6. Absorption spectra of (a) Cu_2FP and (b) CuP recorded in dichloromethane.

In general, fused porphyrins exhibit three absorption bands (I-III). For Cu_2FP the band at 421 nm (band I) corresponds to a Soret transition, occurring at an energy equivalent to that measured in spectra of the monomeric reference, CuP. The transitions occurring at 557 nm (band II) can be ascribed to a red-shifted (with respect to CuP) Soret transition; and the band at 776 nm (band III) corresponds to a Q-band-like transition that is significantly red-shifted compared to the Q-band transitions observed in spectra of CuP at 541 and 619 nm.

UV-Vis-NIR-SEC measurements show that a one-electron reduction of Cu_2FP, forming Cu_2FP^{1-}, results in a bathochromic shift of the three absorption bands with the new transitions occurring at 430, 607, and 875 nm (Figure 5.7). Further reduction to form the dianionic species, Cu_2FP^{2-}, results in additional bathochromic shifting of the Soret bands (moving to 442 nm and 615 nm), and a Q-band transition that undergoes a hypsochromic shift with respect to the intermediate monoanionic species (moving to 861 nm). The presence of well-defined isosbestic points at 377, 429, 468, 571, 675, and 819 nm during

the conversion of Cu_2FP to Cu_2FP^{1-}, and at 439, 495, 573, and 861 nm during the conversion of Cu_2FP^{1-} to Cu_2FP^{2-} are consistent with stable conversion from one redox state to the next without the formation of intermediates or decomposition products. For comparison, UV-Vis-NIR-SEC data obtained using solutions of CuP are included as well in Figure 5.8.

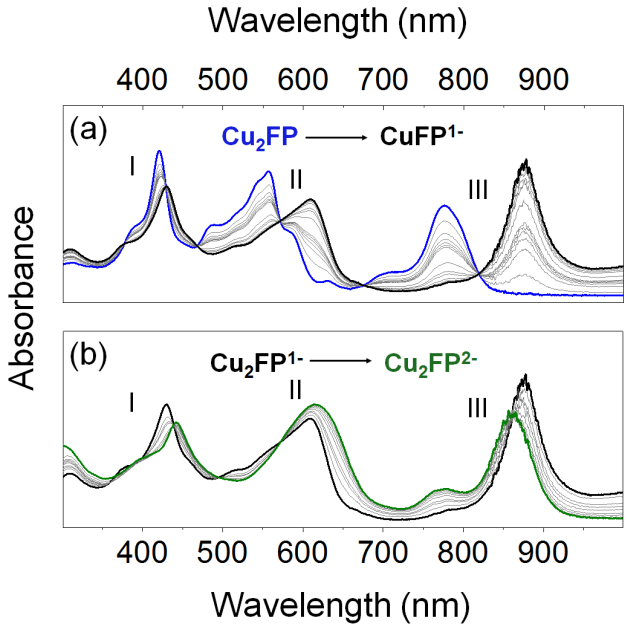

Figure 5.7. (a and b) UV−Vis-NIR absorption spectra of Cu_2FP (6.5 μM) recorded in a 0.1 M $TBAPF_6$ benzonitrile solution polarized at potentials to generate Cu_2FP (blue), Cu_2FP^{1-} (black), and Cu_2FP^{2-} (green).

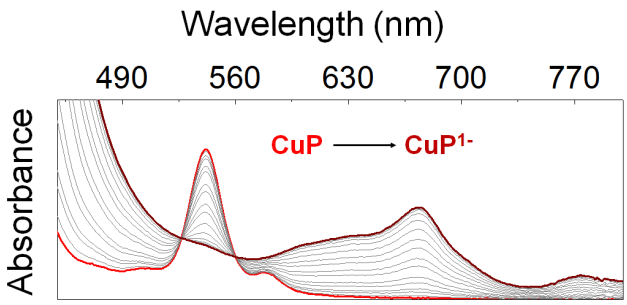

Figure 5.8. UV–Vis absorption spectra of CuP (25 μM) recorded in a 0.1 M $TBAPF_6$ benzonitrile solution polarized at potentials to generate CuP (red) and CuP^{1-} (dark red).

IR-SEC measurements performed using dichloromethane solutions containing Cu_2FP or CuP reveal distinct changes in the vibrational frequency characteristic of an in-plane porphyrin deformation ($\nu_{Cu\text{-}N}$, where ν is the vibrational frequency) following reduction of these complexes. This mode is particularly sensitive to the nature of the porphyrin metal center and its local coordination environment.[27-31] For the monomeric copper(II) porphyrin species, one-electron reduction results in a displacement of $\nu_{Cu\text{-}N}$ from 1003 cm^{-1} to 1009 cm^{-1} ($\Delta\nu$ = 6 cm^{-1}) (Figure 5.9).

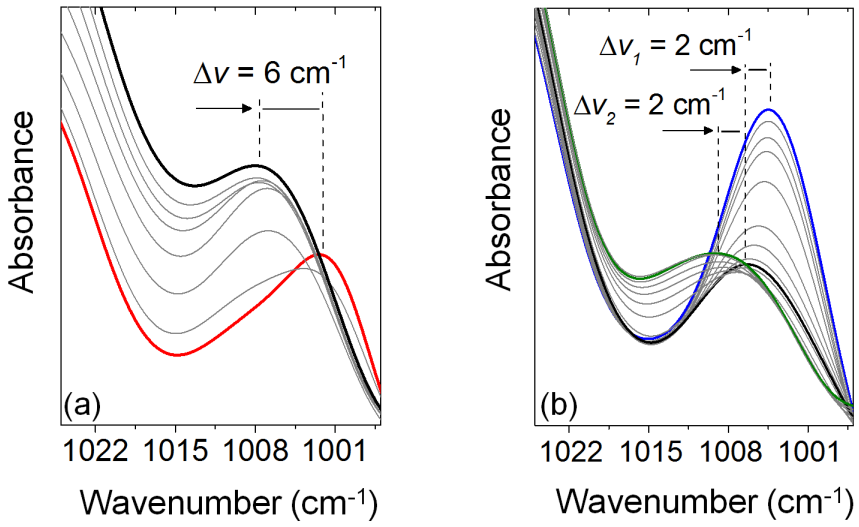

Figure 5.9. FTIR absorption spectra of (c) CuP (0.4 mM) polarized at potentials to generate CuP (red) and CuP^{1-} (black) as well as (d) Cu_2FP (0.4 mM) polarized at potentials to generate Cu_2FP (blue), Cu_2FP^{1-} (black), and Cu_2FP^{2-} (green) collected in a 0.1 M $TBAPF_6$ dichloromethane solution.

By contrast, one-electron reduction of Cu_2FP forming Cu_2FP^{1-}, occurs with a more conservative shift in $\nu_{Cu\text{-}N}$, shifting the band from 1005 cm^{-1} to 1007 cm^{-1} ($\Delta\nu$ = 2 cm^{-1}). Further reduction to form the doubly reduced species, Cu_2FP^{2-}, yields an additional 2 cm^{-1} offset of $\nu_{Cu\text{-}N}$, resulting in a vibrational frequency of 1009 cm^{-1}, a value identical to that measured for the singly reduced monomeric species, CuP^{1-} (Figure 5.9). The initial difference in frequency associated with the in-plane deformation vibrations measured for Cu_2FP and CuP suggests a more rigid structure associated with the extended macrocycle, consistent with the relative downfield shift of the endocyclic pyrrolic N-H proton signal observed in the ^1H NMR spectrum of the free-base fused porphyrin, FBFP, complex (where $\Delta\delta_{N\text{-}H} \sim$ 3.5 ppm with respect to $\delta_{N\text{-}H}$ of the free-base monomeric porphyrin, TTP, and the shift to higher frequency is ascribed to ring current effects resulting from the rigid

π-extended framework imposed by the fused macrocycle architecture) (Figure 6.12). In the IR-SEC data, the presence of well-defined isosbestic points at 997, 1015, and 1181 cm^{-1} during the conversion of Cu_2FP to Cu_2FP^{1-}, and at 997, 1122, and 1159 cm^{-1} during the conversion of Cu_2FP^{1-} to Cu_2FP^{2-} are again consistent with stable conversion from one redox state to the next without the formation of intermediates or decomposition products.

5.2.5 Electrocatalytic Activity for HER

The electrocatalytic HER activity of Cu_2FP was investigated using TFA as a proton source in solutions of dichloromethane with 0.1 M $TBAPF_6$ as a supporting electrolyte. All measurements were performed using an electrochemical cell equipped with a glassy carbon working electrode wired in a three-electrode configuration. Voltammograms recorded using 0.01 mM solutions of Cu_2FP in the presence of TFA at concentrations ranging from 16.25 mM up to 84.5 mM display an irreversible cathodic wave followed by a more intense catalytic feature associated with hydrogen evolution at more negative potentials (Figures 5.9 and 6.13).

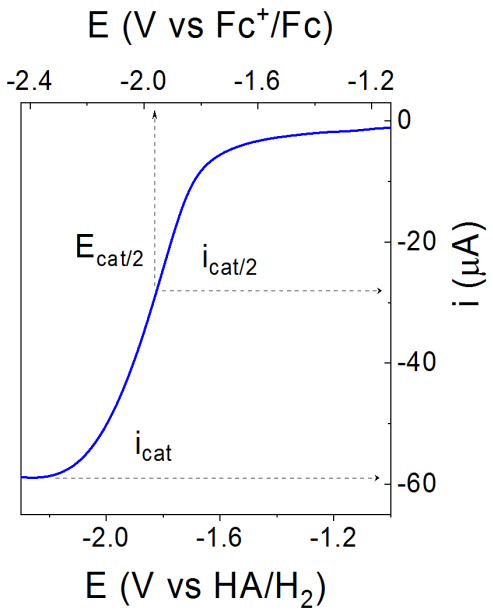

Figure 5. 10. Voltammogram of 0.01 mM Cu_2FP in a 0.1 M $TBAPF_6$ dichloromethane solution with 65 mM TFA recorded at 600 mV s^{-1}. All potentials are reported versus the HA/H_2 equilibrium potential in dichloromethane, calculated using the open circuit potential method developed by Bullock and Roberts.[32]

The S-shape of the voltammograms recorded at relatively high concentrations of acid (≥ 19.5 mM TFA), and at scan rates ≥ 600 mV s^{-1} (Figures 5.11 and 6.14), are consistent with HER activity limited only by the kinetics of the catalytic reaction, as opposed to diffusion of substrate protons. Under these conditions, the fraction of activated catalysts at the electrode surface is near unity and the substrate concentration at the electrode surface is approximately equal to the bulk concentration.

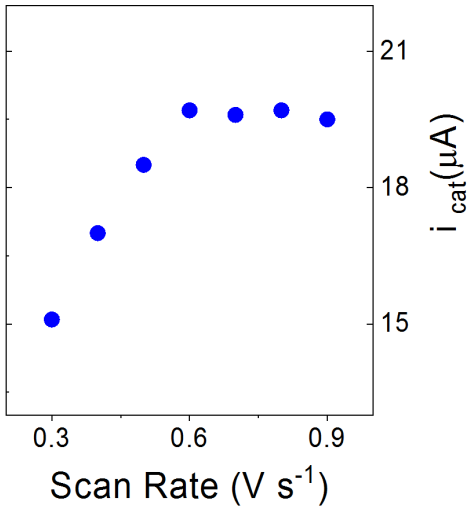

Figure 5.11. Plot of i_{cat} versus the scan rate for 0.01 mM Cu_2FP in a 0.1 M $TBAPF_6$ dichloromethane solution with 19.5 mM TFA.

Further, the plateau currents (i_{cat}) of the S-shaped catalytic waves, measured at concentrations of acid ranging from 19.5 mM up to 65 mM in TFA, are scan rate independent and proportional to the square root of the concentration of acid, indicating a first-order rate dependence in acid. At concentrations of TFA > 65 mM (a more than 6500-fold excess in acid with respect to the amount of catalyst), this proportionality no longer holds and increasing the concentration of TFA has little to no effect on the value of i_{cat}, indicating a zero-order rate dependence in acid has been reached (Figure 5.12).

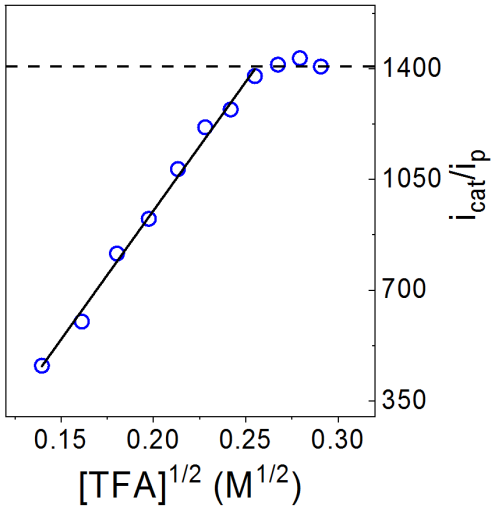

Figure 5.12. Plot of i_{cat}/i_p versus the square root of the concentration of TFA. The plateau currents are taken from cyclic voltammograms recorded at 600 mV s^{-1} using 0.01 mM Cu_2FP in a 0.1 M $TBAPF_6$ dichloromethane solution with 19.5−84.5 mM TFA.

In these experiments, the concentration of acid and catalyst is related to i_{cat} by Eq. 1:

$$i_{cat} = nFAC\sqrt{Dk[H^+]^x} \qquad \text{Eq. 1}$$

where n represents the number of electrons involved in the catalytic process (in this case 2), F is the Faraday constant, A is the electrode surface area, C is the concentration of catalyst, D is the diffusion coefficient for Cu_2FP, k is a rate constant, and x is the order of the reaction with respect to the concentration of acid.[1-4] Eq. 1 can be divided by the Randles-Sevcik equation (Eq. 2), which describes the dependence of peak current (i_p) on the scan rate (v) for a reversible redox process. In the Randles-Sevcik equation, n' represents the number of electrons involved in the redox event (in this case 1).

$$i_p = 0.44n'FAC\sqrt{\frac{n'FvD}{RT}} \qquad \text{Eq. 2}$$

The resulting ratio of i_{cat}/i_p allows determination of the observed rate constant (k_{obs}) (Eq. 3 and Eq. 4) without independent measurement of the diffusion coefficient.[1-4]

$$\frac{i_{cat}}{i_p} = \frac{n}{0.446}\sqrt{\frac{RT}{Fv}k[H^+]^x} \qquad \text{Eq. 3}$$

$$k_{obs} = k[H^+]^x = 1.94V^{-1}v(\frac{i_{cat}}{i_p})^2 \qquad \text{Eq. 4}$$

Under the solution conditions where i_{cat} is scan rate independent and proportional to the square root of the TFA concentration, k_{obs} is directly proportional to the concentration of TFA, per Eq. 1 and Eq. 3, and is thus first order with respect to the concentration of acid (Figure 5.13). (The data points used to calculate k_{obs} are the i_{cat}/i_p values from the plot of i_{cat}/i_p versus the square root of the concentration of TFA shown in Figure 5.10. The last two data points, in which k_{obs} is independent of the acid concentration are omitted. R^2 = 0.993. Slope = 4.43 x10^7.)

Upon reaching conditions where i_{cat} no longer changes with respect to the concentration of TFA, k_{obs} becomes zero-order with respect to the concentration of acid and has a value of approximately 2.2 x 10^6 s^{-1}

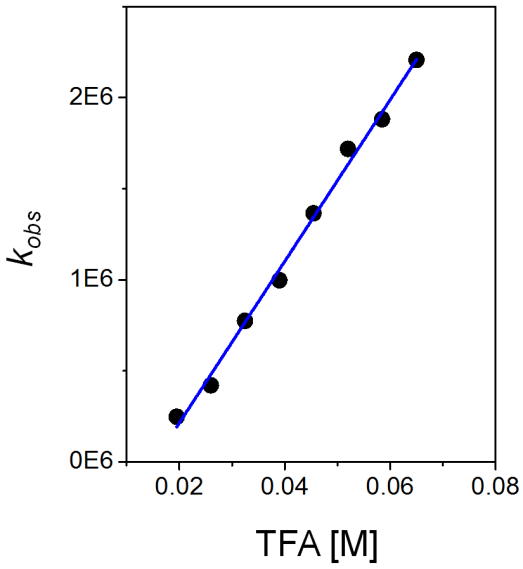

Figure 5.13. Plot of k_{obs} versus the concentration of TFA. The data points used to calculate are the i_{cat}/i_p values from the plot of i_{cat}/i_p versus the square root of the concentration of TFA shown in Figure 5.12.

Following linear sweep voltammetry experiments under the conditions used to obtain the data shown in Figure 5.10, the glassy carbon working electrode was rinsed with dichloromethane to remove physisorbed Cu_2FP species and placed into a fresh 65 mM TFA dichloromethane solution containing 0.1 M $TBAPF_6$ and no Cu_2FP. The lack of current above the background in the linear sweep voltammogram of the glassy carbon working electrode obtained under these conditions is consistent with the absence of active catalysts deposited onto the electrode surface (Figure 6.15). Electrolysis measurements conducted with and without the presence of a mercury pool also show no significant difference in measured current densities, consistent with the notion that catalytic nanoparticles subject to mercury poisoning are not formed during catalysis.[33-35]

Additionally, control electrochemical experiments conducted using a glassy carbon counter electrode in the place of a platinum counter electrode showed no significant differences in the voltammograms recorded under these conditions (Figures 6.16 and 6.17), indicating leached platinum particles are not responsible for the HER activity measured using solutions of Cu_2FP.[36]

Limitations of the dichloromethane solvent window and the significantly negative potentials required to reduce CuP as compared to Cu_2FP, prohibit observation of S-shaped catalytic waves in studies using CuP as the catalyst. However, comparison of the potentials required to achieve an equivalent catalytic current for each compound under the same concentrations of catalyst (0.01 mM) and acid (16.25 mM or 32.5 mM) indicate the solutions of Cu_2FP produce a 5 µA current at potentials 170 mV more positive of that measured using the solutions of CuP (Figures 5.14 a and 6.18).

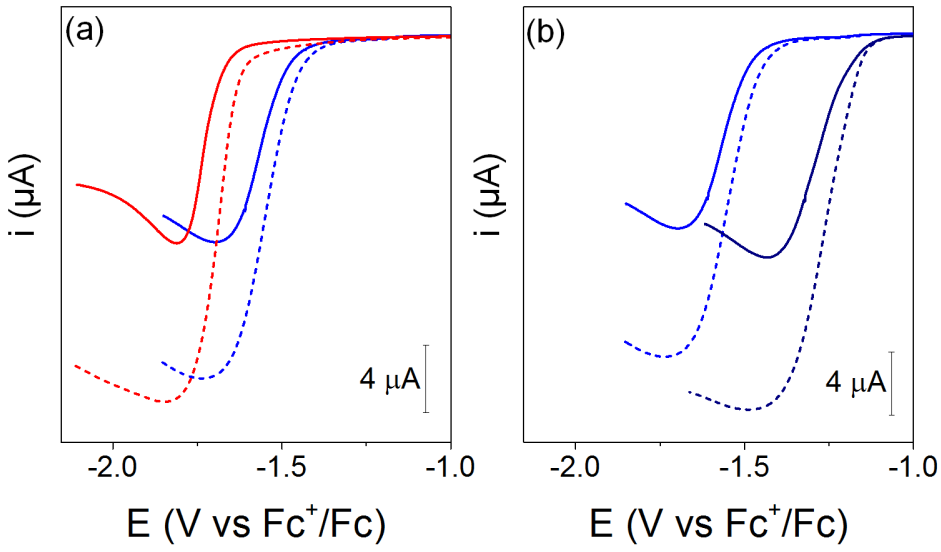

Figure 5.14. Voltammograms of (a) 0.01 mM Cu_2FP (blue) and 0.01 mM CuP (red) as well as (b) 0.01 mM (blue) and 0.1 mM (dark blue) Cu_2FP recorded in a 0.1 M $TBAPF_6$

dichloromethane solution using a 1 mm diameter glassy carbon electrode and a scan rate of 100 mV s^{-1} in the presence of 16.25 (solid) or 32.5 (dash) mM TFA.

Since Cu_2FP consists of two monomeric copper porphyrins fused together, we also compared the potentials required to achieve an equivalent catalytic current for each compound when using 0.02 mM CuP versus 0.01 mM Cu_2FP solutions. In the presence of 16.25 mM or 32.5 mM TFA the solutions of Cu_2FP produce a 5 μA current at potentials 140 mV and 160 mV more positive of the higher concentration solutions of CuP, respectively (Figure 6.19 and 6.20).

Finally, we note that the peak current of the irreversible cathodic wave occurring at less negative potentials using 0.01 mM solutions of Cu_2FP containing TFA is greater than the peak current of the first redox wave recorded in the absence of acid (Figure 5.15). This observation is consistent with catalytic activity occurring at potentials positive of those associated with the more intense catalytic feature, and likely via an alternate mechanism.

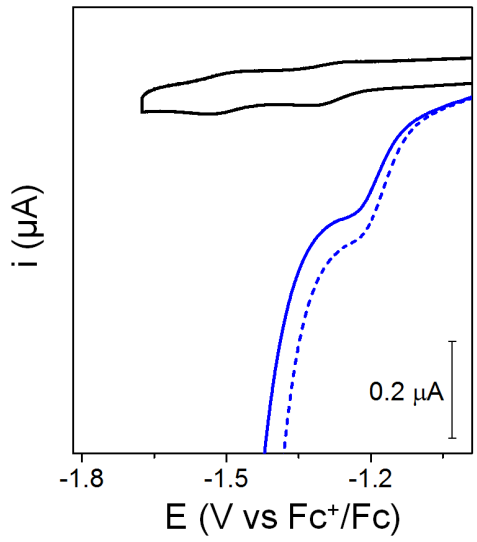

Figure 5.15. Voltammograms of 0.01 mM Cu_2FP recorded in a 0.1 M $TBAPF_6$ dichloromethane solution at a scan rate of 100 mV s^{-1} with either 0 mM (black solid), 16.25 mM (blue solid), or 32.5 mM (blue dashed) mM TFA.

The activity at these lower potentials is also more pronounced in voltammograms recorded using higher concentrations of Cu_2FP, which may indicate the existence of a homolytic pathway (Figures 5.14 b).[37] Comparison of voltammograms recorded using Cu_2FP and CuP at this higher concentration (0.1 mM) and in the presence of 16.25 mM or 32.5 mM TFA indicates the Cu_2FP species achieves a 5 μA current at potentials 330 mV and 380 mV more positive of that measured using the solutions of CuP, respectively (Figure 6.21).

A kinetic analysis of the Cu_2FP data recorded at higher concentrations of catalyst is not presented in this study, as interpretations are complicated by the notion that separate HER pathways could be contributing to hydrogen production. Likewise, obtaining S-shaped wave conditions required for the analysis used in this report is disfavored at higher

concentrations of catalyst,[1-4] where the local substrate concentration at the electrode can vary from the concentration of the bulk. All kinetic analysis presented in this report thus pertains to data collected using 0.01 mM solutions of Cu_2FP.

5.2.6 Hydrogen Detection via Rotating Ring-Disk

Generation of hydrogen was confirmed using rotating ring-disk electrode (RRDE) analysis (Figures 5.16). These experiments provide *in operando* monitoring of product formation under experimental conditions relevant to those used in this report. This can be especially useful in the study of homogeneous catalysis when on longer time-scales, fouling of the electrode or catalyst decomposition during prolonged bulk electrolysis can complicate interpretation of results. In this study, RRDE measurements were performed using either a 0.01 mM or a 0.1 mM solution of Cu_2FP in a 0.1 M $TBAPF_6$ dichloromethane solution (see Chapter 6 for details).

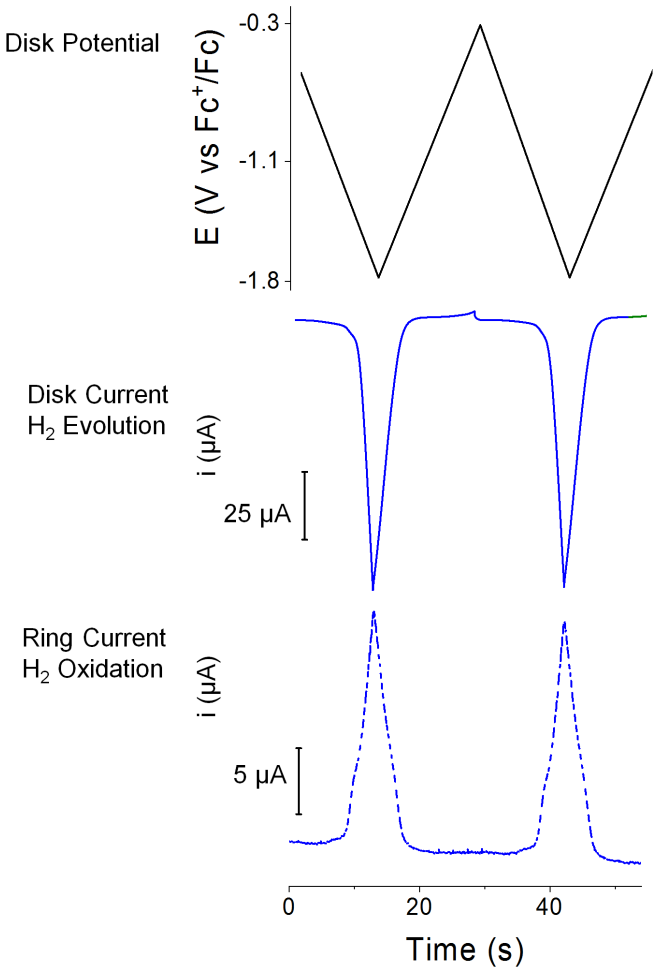

Figures 5.16. Rotating ring-disk measurements (100 mV s^{-1}) of hydrogen evolution using 0.01 mM of Cu_2FP in a dichloromethane solution with 0.1 M $TBAPF_6$ electrolyte and 2.6 mM TFA at a glassy carbon electrode. (Top) GC disk potential. (Middle) GC disk current. (Bottom) Pt-ring current (the Pt ring was held at 0.79 V vs Fc^+/Fc).

The addition of TFA (2.6 mM) confirms that hydrogen can be generated and detected at a concentric platinum ring polarized at 0.79 V vs Fc^+/Fc. In these experiments, the Faradaic efficiency was measured from the ring current collected while the disk electrode was held at a current density of approximately 0.5 mA cm^{-2}. Under these conditions, the Faradaic

efficiency of Cu_2FP, ε, is proportional to the ratio of the ring to the disk current, as shown in Eq. 5:[38]

$$\varepsilon = \frac{i_r}{i_d N} \qquad \text{Eq. 5}$$

In this equation i_r is the measured ring current, i_d is the disk current, and N is the collection efficiency of the RRDE assembly. The collection efficiency was independently determined to be N = 22.1 (±0.4)% yielding a Faradaic efficiency of 88 (±4)% and 90 (±6)% for experiments recorded using either a 0.01 or 0.1 mM solution of Cu_2FP, respectively.

5.2.7 Acid Stability

The stability of Cu_2FP in solutions of TFA (up to a 7000-fold excess in acid) in dichloromethane and benzonitrile was monitored via UV-Vis-NIR spectroscopy over the course of 4 h (Figure 5.17).

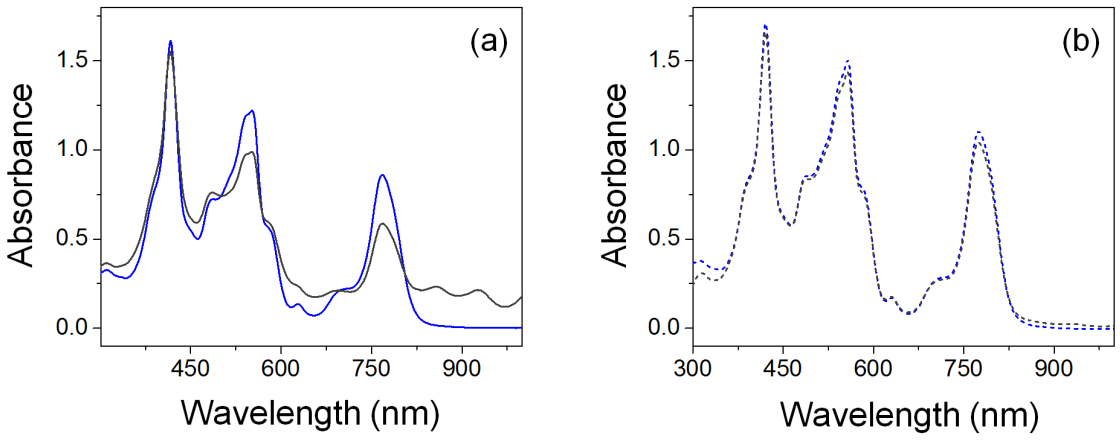

Figures 5.17. Absorption spectra of Cu_2FP (12.5 µM) recorded in (a) dichloromethane or (b) benzonitrile in the absence (blue) or presence (black) of TFA (87.5 mM) after 4 h.

These results indicate the fused porphyrin metal centers remain intact under the conditions studied, showing no detectable signals associated with demetallated species (see Chapter 6 for details). In addition, mass spectrometry analysis of solutions of Cu_2FP containing a 7000-fold excess of TFA also show no indication of a demetallated species, or other degradation products (Figure 6.22). Instead a single isotopic cluster is observed with mass to charge ratios anticipated for intact Cu_2FP.

5.3 Conclusions

Fused bimetallic copper porphyrins are shown to be highly active HER catalysts. In comparison with the non-fused copper porphyrin monomeric complex, the fused ligand scaffold permits access to reduced species at significantly less negative applied bias potentials ($\Delta E_{½}$ of ~ 570 mV for the first reduction process), offering an alternative strategy, compared to the use of electron-withdrawing functional groups, to adjust redox properties of a molecular catalyst for fuel production. Kinetic analysis of the fused bimetallic Cu(II) porphyrin complex under pure kinetic conditions in organic solvents using TFA as a proton source yields an observed rate constant above 2,000,000 s^{-1}. This global rate constant is among the highest reported in the literature. Consistent with the ease of reduction over the analogous non-fused copper porphyrin, the fused bimetallic copper porphyrin also shows significant improvement in the overpotential required to achieve a given turnover frequency. Although activation of the complex requires a substantial bias [half-wave potential ($E_{cat/2}$) = -1.80 V vs HA/H_2], the favorable catalytic properties of the fused porphyrin architecture, over those of the analogous non-fused porphyrin, demonstrate the promise of extended macrocycles as a design element and structural motif for preparing electrocatalysts. The enhanced activity and improved

catalytic parameters of the binuclear copper fused porphyrin architecture indicate a promising avenue for catalyst design, warranting further analysis.

5.4 References

(1) Artero, V.; Savéant, J.-M. Toward the Rational Benchmarking of Homogeneous H_2- evolving Catalysts. *Energy Environ. Sci.* **2014**, *7* (11), 3808–3814.

(2) Costentin, C.; Savéant, J. M. Multielectron, Multistep Molecular Catalysis of Electrochemical Reactions: Benchmarking of Homogeneous Catalysts. *ChemElectroChem*. **2014**, *1* (7), 1226−1236.

(3) Rountree, E. S.; McCarthy, B. D.; Eisenhart, T. T. Dempsey, J. L. Evaluation of Homogeneous Electrocatalysts by Cyclic Voltammetry. *Inorg. Chem.* **2014**, *53* (19), 9983−10002.

(4) Lee, K. J.; Elgrishi, N.; Kandemir, B.; Dempsey, J. L. Electrochemical and Spectroscopic Methods for Evaluating Molecular Electrocatalysts. *Nat. Rev. Chem.* **2017**, *1*, 0039

(5) Roberts, E. M.; Koski, W. S. An Electron Spin Resonance Study of Copper Etioporphyrin II. *J. Am. Chem. Soc.* **1960**, *82* (12), 3006−3010.

(6) Blumberg, W. E.; Peisach, J. An Electron Spin Resonance Study of Copper Uroporphyrin III and Other Touraco Feather components. *J. Biol. Chem*. **1965**, *240* (2), 870−876.

(7) Assour, J. M. Electron Spin Resonance of Tetraphenylporphine Chelates. *J. Chem. Phys.* **1965**, *43* (7), 2477−2489.

(8) Gurd, F. R. N.; Falk, K. E.; Malmström, B. G.; Vänngård, T. A Magnetic Resonance Study of Sperm Whale Ferrimyoglobin and its Complex with 1 Cupric Ion. *J. Biol. Chem*. **1967**, *242* (24), 5724−5730.

(9) Bemski, G.; Arends, T.; Blanc, G. Electron Spin Resonance of Cu (II) in Copper-Hemoglobin Complexes. *Biochem. Biophys. Res. Commun*. **1969**, *35* (5), 599−605.

(10) Hsu, Y. EPR Studies of Three Cupric Complexes with Nitrogenous Ligands. *Molec. Phys.* **1971**, *21* (6), 1087−1103.

(11) Clark, C. O.; Poole, J. C. P.; Farach, H. A. An Electron Spin Resonance Study of Copper (II) Tetraphenyl Porphyrins. *J. Phys. C: Solid State Phys*. **1978**, *11* (4), 769−774.

(12) Solomon, E. I.; Heppner, D. E.; Johnston, E. M.; Ginsbach, J. W.; Cirera, J.; Qayyum, M.; Kieber-Emmons, M. T.; Kjaergaard, C. H.; Hadt, R. G.; Tian, L. Copper Active Sites in Biology. *Chem. Rev*. **2014**, *114* (7), 3659−3853.

(13) Peisach, J.; Blumberg, W. E. Structural Implications Derived from the Analysis of Electron Paramagnetic Resonance Spectra of Natural and Artificial Copper Proteins. *Arch. Biochem. Biophys.* **1974**, *165* (2), 691−708.

(14) Toyama, N.; Asano-Someda, M.; Kaizu, Y. EPR Spectra of Gable-type Copper (II) Porphyrin Dimers in Fluid Solution: Extraction of Exchange Interaction in Weakly Coupled Doublet Pairs. *Mol. Phys*. **2003**, *101* (6), 733−742.

(15) Wang, R.; Brugh, A. M.; Rawson, J.; Therien, M. J.; Forbes, M. D. E. Alkyne-Bridged Multi [Copper (II) Porphyrin] Structures: Nuances of Orbital Symmetry in Long-Range, Through-Bond Mediated, Isotropic Spin Exchange Interactions. *J. Am. Chem. Soc*. **2017**, *139* (29), 9759−9762.

(16) Tsuda, A.; Osuka, A. Discrete Conjugated Porphyrin Tapes with an Exceptionally Small Bandgap. *Adv. Mater.* **2002**, *14* (1), 75−79.

(17) Cho, H. S.; Jeong, D. H.; Cho, S.; Kim, D.; Matsuzaki, Y.; Tanaka, K.; Tsuda, A.; Osuka, A. Photophysical Properties of Porphyrin Tapes. *J. Am. Chem. Soc.* **2002**, *124* (49), 14642−14654.

(18) Ouyang, Q.; Zhu, Y-Z.; Zhang, C-H.; Yan, K-Q.; Li, Y-C.; Zheng, J-Y. An Efficient PIFA-Mediated Synthesis of Fused Diporphyrin and Triply-Singly Interlacedly Linked Porphyrin Array. *Org. Lett.* **2009**, *22* (11), 5266−5269.

(19) Bonifazi, D.; Accorsi, G.; Armaroli, N.; Song, F.; Palkar, A.; Echegoyen, L.; Scholl, M.; Seiler, P.; Jaun, B.; Diederich, F. Oligoporphyrin Arrays Conjugated to [60]Fullerene: Preparation, NMR Analysis, and Photophysical and Electrochemical Properties. *Helvetica Chimica Acta*, **2005**, *88* (7), 1839−1884.

(20) Cheng, F.; Zhang, S.; Adronov, A.; Echegoyen, L.; Diederich, F. Triply Fused Zn^{II}–Porphyrin Oligomers: Synthesis, Properties, and Supramolecular Interactions with Single-Walled Carbon Nanotubes (SWNTs). *Chem. Eur. J.* **2006**, *12* (23), 6062−6070.

(21) Fendt, L-A.; Fang, H.; Plonska-Brzezinska, M. E.; Zhang, S.; Cheng, F.; Braun, C.; Echegoyen, L.; Diederich, F. *meso*, *meso*-Linked and Triply Fused Diporphyrins with Mixed-Metal Ions: Synthesis and Electrochemical Investigations. *Eur. J. Org. Chem.* **2007**, *2007* (28), 4659−4673.

(22) Kadish, K. M.; Van Caemelbecke, E. Electrochemistry of Porphyrins and Related Macrocycles. *J. Solid State Electrochem.* **2003**, *7* (5), 254−258.

(23) Sun, H.; Smirnov, V. V.; DiMagno, S. G. Slow Electron Transfer Rates for Fluorinated Cobalt Porphyrins: Electronic and Conformational Factors Modulating Metalloporphyrin ET. *Inorg. Chem.* **2003**, *42* (19), 6032−6040.

(24) Lyaskovskyy, V.; de Bruin, B. Redox Non-Innocent Ligands: Versatile New Tools to Control Catalytic Reactions. *ACS Catal.* **2012**, *2* (2), 270−279.

(25) Luca, O. R.; Crabtree, R. H. Redox-Active Ligands in Catalysis. *Chem. Soc. Rev.* **2013**, *42* (4), 1440−1459.

(26) Wu, Y.; Jiang, J.; Weng, Z.; Wang, M.; Broere, D. L.; Zhong, Y.; Brudvig, G. W.; Feng, Z.; Wang, H. Electroreduction of CO_2 Catalyzed by a Heterogenized Zn–Porphyrin Complex with a Redox-Innocent Metal Center. *ACS Cent. Sci.* **2017**, *3* (8), 847−852.

(27) Azcarate, I.; Costentin, C.; Robert, M.; Savéant, J. M. Through-Space Charge Interaction Substituent Effects in Molecular Catalysis Leading to the Design of the Most Efficient Catalyst of CO_2-to-CO Electrochemical Conversion. *J. Am. Chem. Soc.* **2016**, *138* (51), 16639−16644.

(28) Lee, C. H.; Dogutan, D. K.; Nocera, D. G. Hydrogen Generation by Hangman Metalloporphyrins. *J. Am. Chem. Soc.* **2011**, *133* (23), 8775−8777.

(29) Boucher, L. J.; Katz, J. J. The Infrared Spectra of Metalloporphyrins (4000-160 Cm^{-1}). *J. Am. Chem. Soc.* **1967**, *89* (6), 1340−1345.

(30) Kincaid, J.; Nakamoto, K. Vibrational Spectra of Transition Metal Complexes of Tetraphenylporphine. *J. Inorg. Nucl. Chem.* **1975**, *37* (1), 85−89.

(31) Khusnutdinova, D.; Beiler, A. M.; Wadsworth, B. L.; Nanyangwe, S. K.; Moore, G. F. Vibrational Structure Analysis of Cobalt Fluoro-Porphyrin Surface Coatings on Gallium Phosphide. *J. Porphyrins Phthalocyanines* **2018**, *22* (6), 461−466.

(32) Roberts, J. A.; Bullock, R. M. Direct Determination of Equilibrium Potentials for Hydrogen Oxidation/Production by Open Circuit Potential Measurements in Acetonitrile. *Inorg. Chem.* **2013**, *52* (7), 3823−3835.

(33) Crabtree, R. H. Resolving Heterogeneity Problems and Impurity Artifacts in Operationally Homogeneous Transition Metal Catalysts. *Chem. Rev.* **2011**, *112* (3), 1536−1554.

(34) Artero, V.; Fontecave, M. Solar Fuels Generation and Molecular Systems: is it Homogeneous or Heterogeneous Catalysis? *Chem. Soc. Rev.* **2013**, *42* (6), 2338−2356.

(35) Widegren, J. A.; Finke, R. G. A Review of the Problem of Distinguishing True Homogeneous Catalysis from Soluble or Other Metal-Particle Heterogeneous Catalysis Under Reducing Conditions. *J. Mol. Catal. A: Chem.* **2003**, *198* (1-2), 317−341.

(36) Chen, J. G.; Jones, C. W.; Linic, S; Stamenkovic, V. R. Best Practices in Pursuit of Topics in Heterogeneous Electrocatalysis. *ACS Catal.* **2017**, *7* (9), 6392−6393.

(37) Costentin, C.; Dridi, H.; Savéant, J. M. Molecular Catalysis of H_2 Evolution: Diagnosing Heterolytic versus Homolytic Pathways. *J. Am. Chem. Soc.* **2014**, *136* (39), 13727−13734.

(38) McCrory, C. C.; Jung, S.; Peters, J. C.; Jaramillo, T. F. Benchmarking Heterogeneous Electrocatalysts for the Oxygen Evolution Reaction. *J. Am. Chem. Soc.* **2013**, *135* (45), 16977−16987.

CHAPTER 6 EXPERIMENTAL PROCEDURES

6.1 General Experimental Methods

UV-Vis

Ultraviolet−visible (UV−Vis) optical spectra were recorded on a Shimadzu SolidSpec-3700 spectrometer with a D2 (deuterium) lamp for the ultraviolet range and a WI (halogen) lamp for the visible and near-infrared. Transmission and reflectance measurements were performed with an integrating sphere.

Mass Spectra

Mass spectra of all compounds were obtained with Voyager DE STR matrix-assisted laser desorption/ionization time-of-flight spectrometer (MALDI-TOF) mass spectrometer in positive ion mode employing a trans, trans–1,4–diphenyl–1,3–butadiene matrix (unless otherwise noted). The reported mass is for the most abundant isotopic ratio observed (obsd.). To facilitate comparison, calculated values of the anticipated most abundant isotopic ratio (calcd.) are listed before the experimental result.

NMR

Nuclear magnetic resonance (NMR) spectra were recorded on a Varian NMR spectrometer operating at 400 MHz. Unless otherwise stated, all spectra were collected at room temperature.

FTIR

Grazing angle attenuated total reflection Fourier transform infrared (GATR-FTIR) spectroscopy was performed using a VariGATR accessory (Harrick Scientific) with a Ge crystal plate installed in a Bruker Vertex 70. A minimum of two individual wafers were tested for each sample. Samples were pressed against the Ge crystal to ensure effective optical coupling. Spectra (256 scans) were collected under a dry nitrogen purge with a 4 cm^{-1} resolution, GloBar MIR source, a broadband KBr beamsplitter, and a liquid

nitrogen cooled MCT detector. Background measurements (256 scans) were obtained from the bare Ge crystal and the data were processed using OPUS software. GATR-FTIR measurements were baseline corrected for rubberband scattering. Spectra of model compounds in pressed KBr pellets were acquired with the same settings but using transmission mode.

XPS

X-ray photoelectron (XP) spectroscopy was performed using a monochromatized Al Kα source (hν = 1486.6 eV), operated at 63 W, on a Kratos system at a takeoff angle of 0° relative to the surface normal and a pass energy for narrow scan spectra of 20 eV at an instrument resolution of approximately 700 meV. Survey spectra (40 scans) were collected with a pass energy of 150 eV. A minimum of two wafers were analyzed for each sample. Spectral fitting was performed using Casa XPS analysis software and all spectra were calibrated by adjusting C 1s core level position to 284.8 eV. Curves were fit with quasi-Voigt lines following Shirley background subtraction.

6.2 Experimental Procedures for Chapter 2

Materials

All compounds were synthesized from commercially available starting materials Chloroform, $BF_3(OEt)_2$, 2,3-dichloro-5,6-dicyano-1,4-benzoquinone, triethylamine, pyridine, *N*-bromosuccinamide, tetrakis(triphenylphosphine)palladium(0), sodium sulfate, cobalt (II) acetate were purchased from Aldrich. Solvents were obtained from Aldrich or Mallinckrodt. Dichloromethane, hexanes, toluene and *p*-tolyl aldehyde were freshly distilled before use. Milli-Q water (18.2 MΩ·cm) was used to prepare all aqueous solutions. The synthetic scheme used to prepare the target compounds is shown in Figure 6.1.

GaP(100) wafers

Single crystalline p-type gallium phosphide wafers were purchased from University Wafers. The material is single side polished to an epi-ready finish. The p-type Zn-doped GaP(100) wafers have a resistivity of 0.2 Ω·cm, a mobility of 66 cm^2 V^{-1} s^{-1}, and a carrier concentration of 4.7 x 10^{17} cm^{-3}, with an etch pit density of less than 8 x 10^4 cm^{-2}.

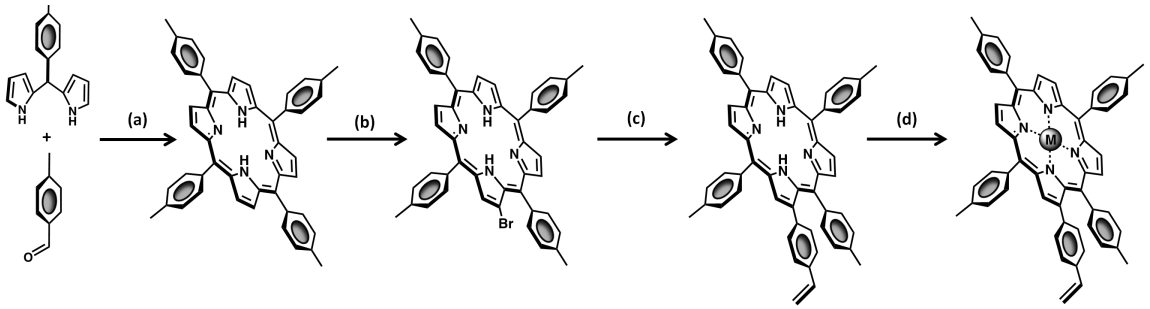

Figure 6.1. Synthetic scheme used to prepare 1 or 2 where (a) $BF_3(OEt)_2$, $CHCl_3$, DDQ, Ar; (b) NBS, $CHCl_3$, Ar, reflux; (c) 4-VPBA, K_2CO_3, $Pd(Ph_3)_4$, reflux; (d) $Co(Ace)_2*4H_2O$ or $Fe(Cl)_3*3H_2O$, DMF, reflux.

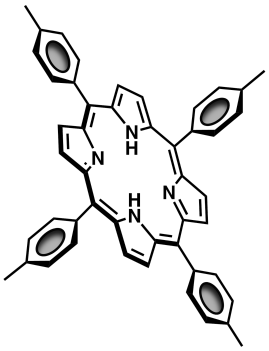

5,10,15,20-tetra *p*-tolylporphyrin (TTP). A similar method was previously reported.[1] A solution of 5-(4-methylphenyl)dipyrromethane (880 mg, 6 mmol) and *p*-tolyl aldehyde (890 mL, 6 mmol) in chloroform (600 mL) was purged for 15 min with argon before adding $BF_3(OEt)_2$ (33 μL of 2.5 M stock solution in chloroform, 3.3 mM). After stirring

for 12 h, 2,3-dichloro-5,6-dicyano-1,4-benzoquinone (DDQ) (2.04 g, 9 mmol) was added and the mixture was stirred for an additional 3 h before adding 7.5 mL of triethylamine. The mixture was filtered through an alumina pad and the solvent was evaporated at reduced pressure. The crude product was purified by column chromatography on silica using a mixture of 2:1 chloroform and hexanes as the eluent to yield the desired product (45%). ^{1}H NMR (400 MHz, $CDCl_3$): δ –2.77 (2H, s, NH), 2.70 (12H, s, CH_3), 7.55 (8H, d, J = 7.8 Hz, ArH), 8.09 (8H, d, J = 7.8 Hz, ArH) 8.85 (8H, s, βH); MALDI-TOF-MS *m/z*. calcd. for $C_{48}H_{38}N_4$ 670.31, obsd. 670.46; UV-Vis (Toluene) 420, 516, 550, 593, 651 nm.

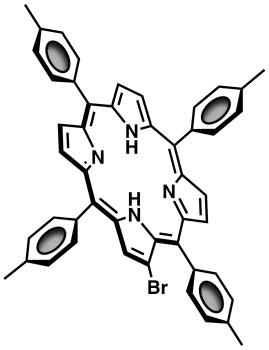

β-bromo-5,10,15,20-tetra-*p*-tolylporphyrin. A similar method was previously reported.[2] 5,10,15,20-tetra-*p*-tolylporphyrin (120 mg, 0.179 mmol) and pyridine (2 mL) were dissolved in chloroform (120 mL) and the solution was stirred and heated to reflux. After 15 min, a solution of *N*-bromosuccinamide (64 mg, 0.358 mmol, dissolved in 30 mL chloroform) was added dropwise over 45 min to the refluxing mixture. The reaction mixture was quenched with acetone (20 mL), and the solvent evaporated at reduced pressure. The crude residue was purified by column chromatography on silica using a mixture of 1:1 cyclohexanes and chloroform as the eluent to give the desired product (45%). ^{1}H NMR (400 MHz, $CDCl_3$): δ –2.85 (2H, s, NH), 2.70 (12H, s, CH_3), 7.58-7.50

(8H, m, ArH), 7.95 (2H,d, J = 7.8 Hz, ArH), 8.10 (2H, d, J = 7.8 Hz, ArH) 8.10 (2H, d, J = 7.5 Hz, ArH), 8.10 (2H, d, J = 7.3 Hz, ArH), 8.93-8.74 (7H, m, βH); MALDI-TOF-MS *m/z*. calcd. for $C_{48}H_{37}BrN_4$ 748.22 (750.22), obsd. 750.64 (748.65); UV-Vis (Toluene) 422, 519, 554, 595, 651 nm.

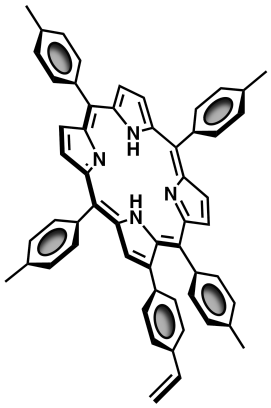

5,10,15,20-tetra-*p*-tolyl-2-(4-vinylphenyl)porphyrin (5). 4-vinylphenylboronic acid (4-VPBA) (89 mg, 0.6 mmol), potassium carbonate (138 mg, 1.2 mmol) and tetrakis(triphenylphosphine)palladium(0) (16 mg, 0.012 mmol) were added to a solution containing β-bromo-5,10,15,20-tetra-*p*-tolylporphyrin (90 mg, 0.12 mmol) dissolved in toluene (35 mL) and under an argon atmosphere. The reaction mixture was heated to reflux and the progress of the reaction was monitored via thin-layer chromatography (TLC). The reaction was stopped following consumption of the porphyrin staring material (~3-5 h) and the mixture was washed with a saturated solution of aqueous sodium bicarbonate then a saturated solution of aqueous sodium chloride. The organic phase was dried over sodium sulfate, filtered, and the solvent evaporated at reduced pressure. The residue was purified by column chromatography on silica using a mixture of 1:1 dichloromethane and hexanes as the eluent to yield the desired product (68%). ^{1}H NMR (400 MHz, $CDCl_3$) δ –2.63 (2H, s, NH), 2.38 (3H, s, CH_3), 2.67 (3H, s, CH_3), 2.70

(6H, s, CH_3), 5.25 (1H, d, *J* = 11.1 Hz, CH), 5.78 (1H, d, *J* = 17.7 Hz, CH), 6.76 (1H, dd, *J* = 17.6 Hz, *J* = 10.87 Hz, CH), 7.01 (2H, d, *J* = 7.7 Hz, ArH), 7.18 (2H, d, *J* = 8.1 Hz, ArH), 7.25 (2H, d, *J* = 7.9 Hz, ArH), 7.51 (2H, d, *J* = 7.8 Hz, ArH), 7.54 (2H, d, *J* = 7.6 Hz, ArH), 7.56 (2H, d, *J* = 7.6 Hz, ArH), 7.73 (2H, d, *J* = 7.9 Hz, ArH), 8.09 (2H, d, *J* = 7.8 Hz, ArH), 8.10 (2H, d, *J* = 7.8 Hz, ArH), 8.10 (2H, d, *J* = 7.8 Hz, ArH), 8.87-8.74 (7H, m, βH); MALDI-TOF-MS *m/z*. calcd. for $C_{56}H_{44}N_4$ 772.36, obsd. 772.42. UV-Vis (Toluene) 424, 520, 554, 597, 653 nm.

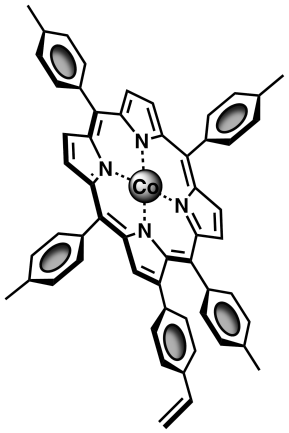

Cobalt(II) 5,10,15,20-tetra-*p*-tolyl-2-(4-vinylphenyl)porphyrin (1). A mixture containing 5,10,15,20-tetra-*p*-tolyl-2-(4-vinylphenyl)porphyrin (23 mg, 0.03 mmol) and cobalt (II) acetate (53 mg, 0.3 mmol) in dimethylformamide (35 mL) was stirred at reflux for 20 min. Upon cooling, the solvent was removed at reduced pressure. The residue was purified by column chromatography on alumina using dichloromethane as eluent. Recrystallization from dichloromethane/methanol gave the target compound (98%). UV-Vis (Toluene) 421, 535 nm; MALDI-TOF-MS *m/z*. calcd. for $C_{56}H_{42}CoN_4$ 829.27, obsd. 829.15.

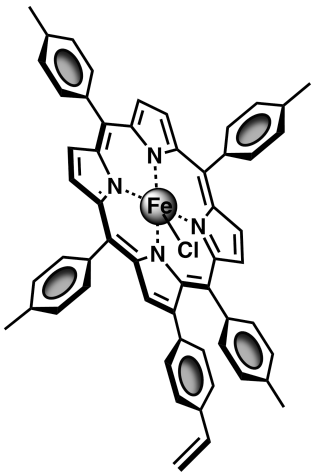

Iron(III) 5,10,15,20-tetra-*p*-tolyl-2-(4-vinylphenyl)porphyrin chloride (2). 5,10,15,20-tetra-*p*-tolyl-2-(4-vinylphenyl)porphyrin (32 mg, 0.04 mmol) was dissolved in dimethylformamide (18 mL) and the mixture was stirred and heated to reflux . Upon reaching reflux, $FeCl_2$*$4H_2O$ (49 mg, 0.25 mmol) was added to the solution in three approximately equivalent portions over 30 min. Upon cooling, the solvent was evaporated at reduced pressure and the brown residue was purified on alumina column using dichloromethane as eluent. The green colored fractions obtained from chromatography were concentrated and washed with an aqueous 6M HCl solution. The organic solvent was removed under reduced pressure and the brown residue was recrystallized from methanol to give the target compound (98%). UV-Vis (Toluene) 423, 513, 578, 668, 699 nm; MALDI-TOF-MS *m/z*. calcd. for $C_{56}H_{42}ClFeN_4$ 861.24, obsd. 863.18.

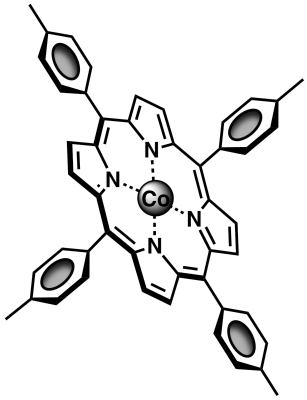

Cobalt(II) 5,10,15,20-tetra-*p*-tolylporphyrin (3). A similar method was previously reported.[3] 5,10,15,20-tetra-*p*-tolylporphyrin (25 mg, 0.03 mmol) and a solution of cobalt (II) acetate (53 mg, 0.3 mmol) were dissolved in dimethylformamide (35 mL) and brought to reflux. The mixture was refluxed for 20 min before evaporating the solvent at reduced pressure. The product was purified on an alumina column using dichloromethane as eluent and recrystallized from dichloromethane/methanol to give a desired product (98%). UV-Vis (Toluene) 416, 530 nm.

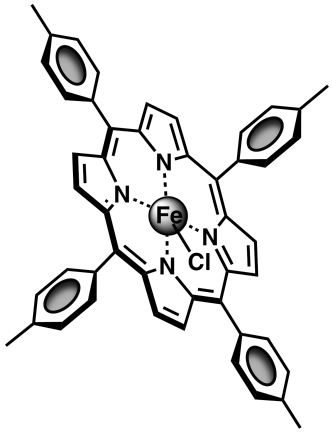

Iron(III) 5,10,15,20-tetra-*p*-tolylporphyrin chloride (4). A similar method was previously reported.[4] 5,10,15,20-tetra-*p*-tolylporphyrin (35 mg, 0.04 mmol) was dissolved in dimethylformamide (18 mL) and the mixture was stirred and heated to

reflux. Upon reaching reflux, $FeCl_2*4H_2O$ (49 mg, 0.25 mmol) was added to the solution in approximately three equivalent portions over 30 min. Upon cooling, the solvent was evaporated at reduced pressure and the brown residue was purified on an alumina column using dichloromethane as eluent. The green colored fractions obtained from chromatography were concentrated and washed with an aqueous 6M HCl solution. The organic solvent was removed under reduced pressure and the brown residue was recrystallized from methanol to give the target compound (98%). UV-Vis (Toluene) 421, 509, 571, 668, 691 nm.

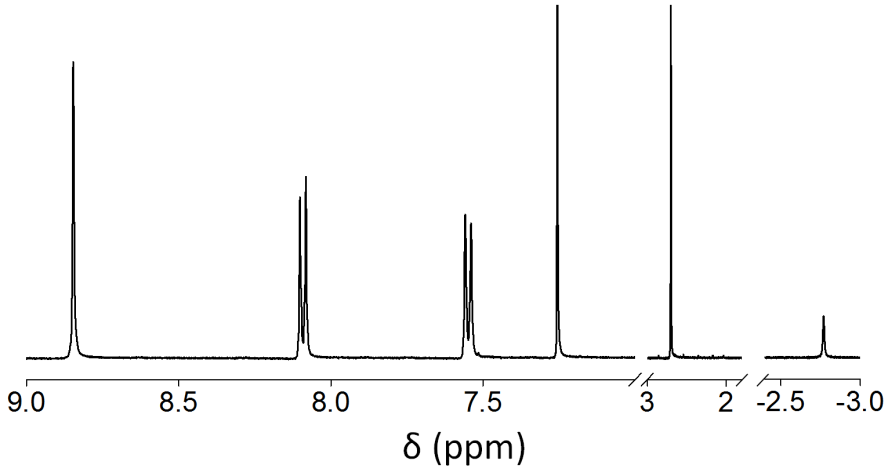

Figure 6.2. 400 MHZ ^{1}H NMR spectrum of 5,10,15,20-tetra-*p*-tolylporphyrinrecorded in chloroform-d. ^{1}H NMR (400 MHz, $CDCl_3$): δ –2.77 (2H, s, NH), 2.70 (12H, s, CH_3), 7.55 (8H, d, J = 7.8 Hz, ArH), 8.09 (8H, d, J = 7.8 Hz, ArH) 8.85 (8H, s, βH).

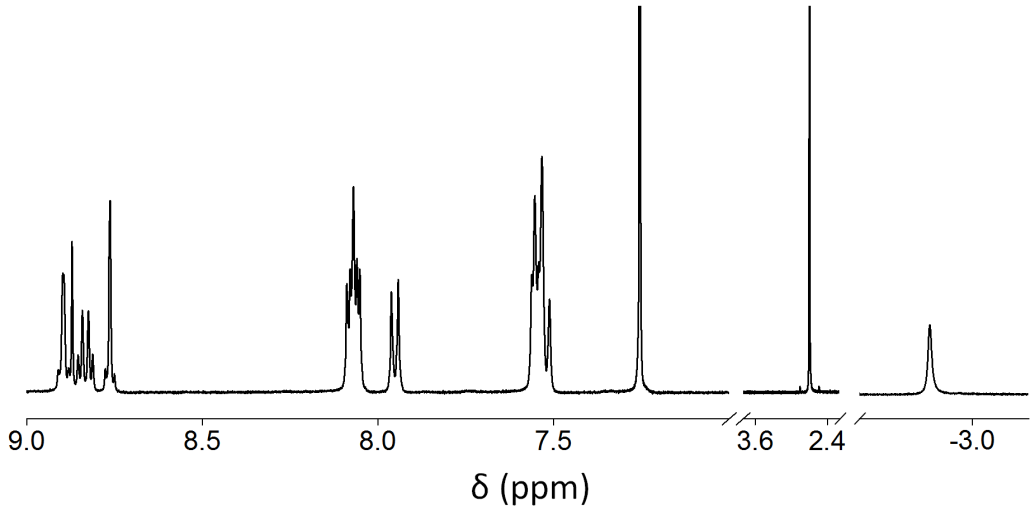

Figure 6.3. 400 MHZ ^{1}H NMR spectrum of *β*-bromo-5,10,15,20-tetra-*p*-tolylporphyrin recorded in chloroform-d. ^{1}H NMR (400 MHz, $CDCl_3$): δ –2.85 (2H, s, NH), 2.70 (12H, s, CH_3), 7.58-7.50 (8H, m, ArH), 7.95 (2H,d, *J* = 7.8 Hz, ArH), 8.10 (2H, d, *J* = 7.8 Hz, ArH) 8.10 (2H, d, *J* = 7.5 Hz, ArH), 8.10 (2H, d, *J* = 7.3 Hz, ArH), 8.93-8.74 (7H, m, βH).

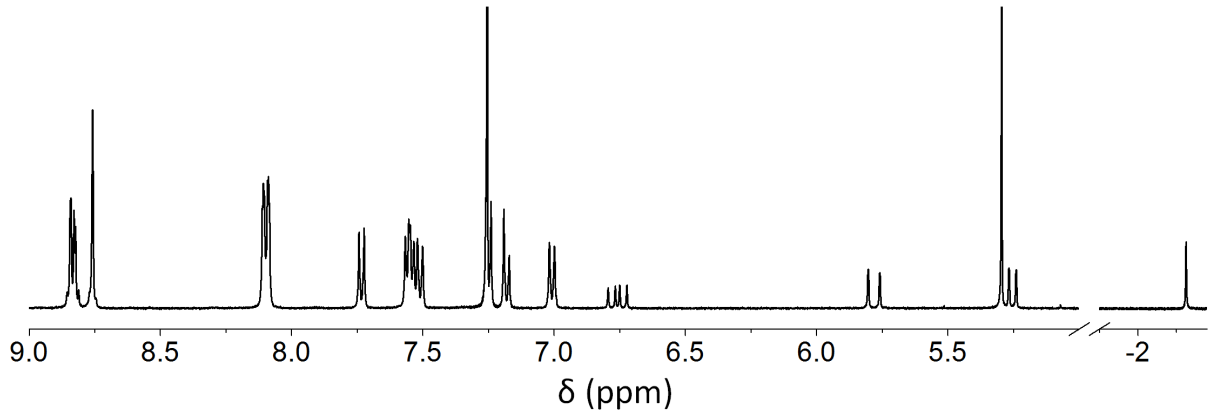

Figure 6.4. 400 MHZ ^{1}H NMR spectrum of 5,10,15,20-tetra-*p*-tolyl-2-(4-vinylphenyl)porphyrin recorded in chloroform-d. ^{1}H NMR (400 MHz, $CDCl_3$) δ –2.63 (2H, s, NH), 2.38 (3H, s, CH_3), 2.67 (3H, s, CH_3), 2.70 (6H, s, CH_3), 5.25 (1H, d, *J* = 11.1 Hz, CH), 5.78 (1H, d, *J* = 17.7 Hz, CH), 6.76 (1H, dd, *J* = 17.6 Hz, *J* = 10.87 Hz, CH), 7.01 (2H, d, *J* = 7.7 Hz, ArH), 7.18 (2H, d, *J* = 8.1 Hz, ArH), 7.25 (2H, d, *J* = 7.9 Hz, ArH), 7.51 (2H, d, *J* = 7.8 Hz, ArH), 7.54 (2H, d, *J* = 7.6 Hz, ArH), 7.56 (2H, d, *J* = 7.6 Hz, ArH), 7.73 (2H, d, *J* = 7.9 Hz, ArH), 8.09 (2H, d, *J* = 7.8 Hz, ArH), 8.10 (2H, d, *J* = 7.8 Hz, ArH), 8.10 (2H, d, *J* = 7.8 Hz, ArH), 8.87-8.74 (7H, m, βH).

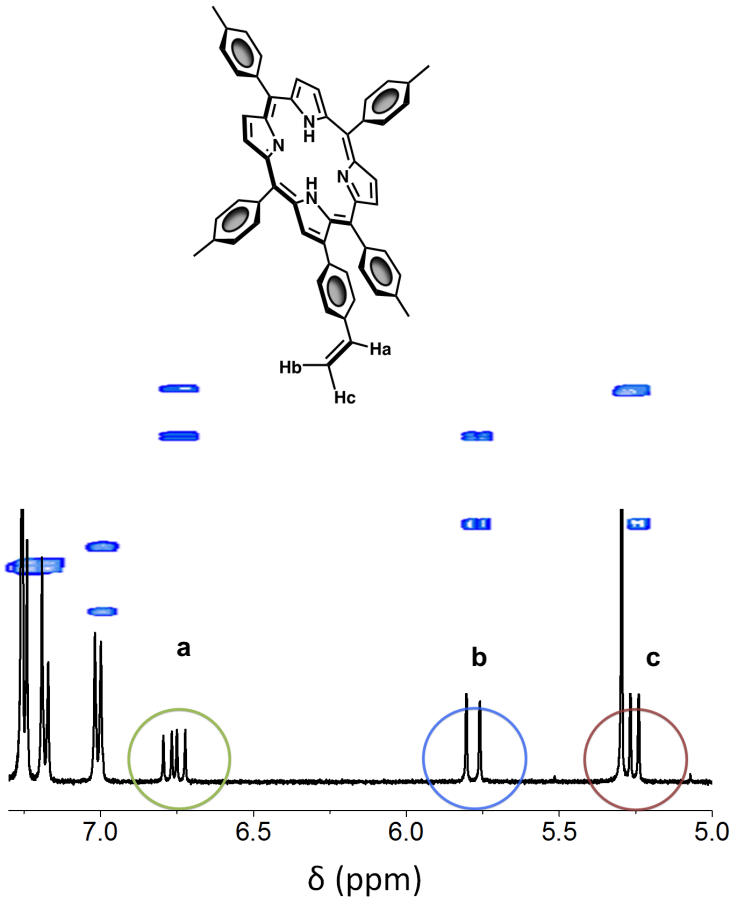

Figure 6.5. 400 MHZ ^{1}H NMR spectra (black) with overlaid gCOSY (aromatic region) of 5,10,15,20-tetra-*p*-tolyl-2-(4-vinylphenyl)porphyrin recorded in chloroform-d.

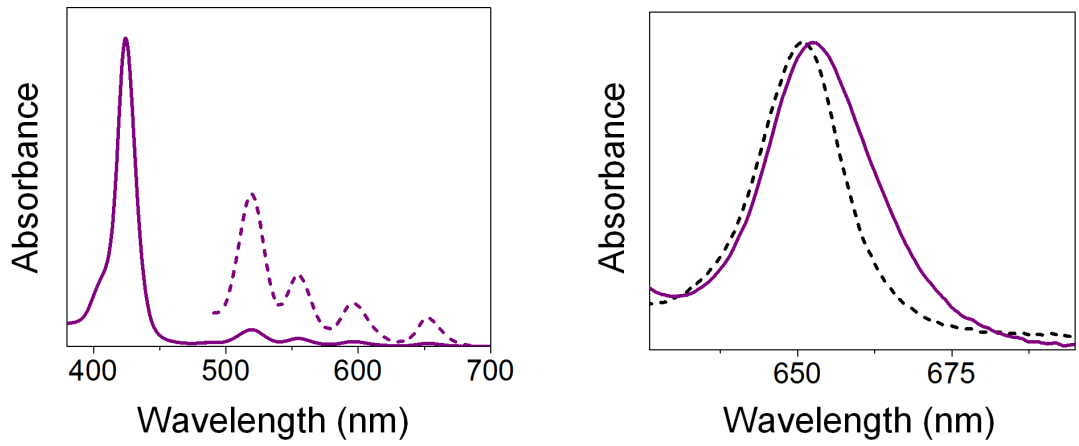

Figure 6.6. (left) Absorption spectra of 5,10,15,20-tetra-*p*-tolyl-2-(4-vinylphenyl)porphyrin recorded in toluene showing the Soret band normalized to 1 (solid) and the highest energy Q-band normalized to 0.5 (dashed). (right) Normalized absorbance spectra showing the lowest energy Q-bands of the model compound 5,10,15,20-tetra-*p*-tolylporphyrin (dashed) and 5,10,15,20-tetra-p-tolyl-2-(4-vinylphenyl)porphyrin (solid) are included for comparison.

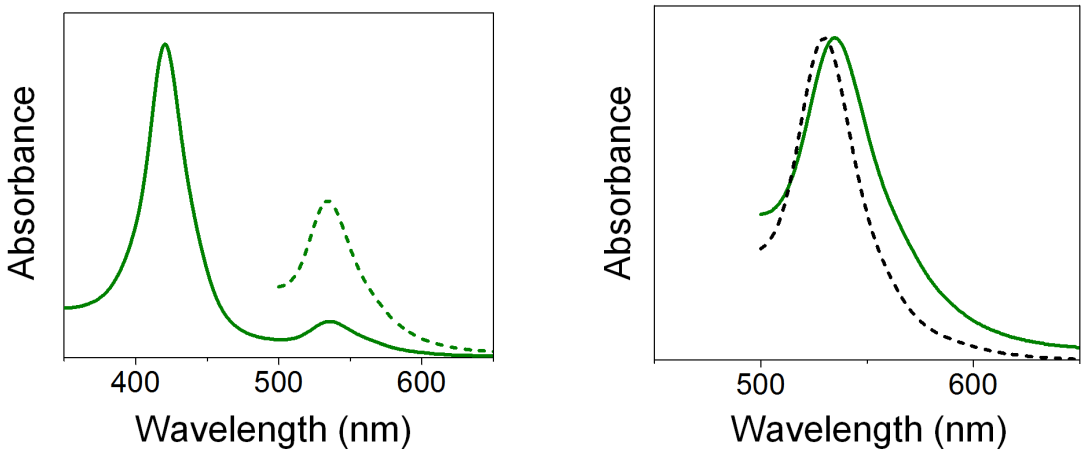

Figure 6.7. (left) Absorbance spectra of 1 recorded in toluene showing the Soret band normalized to 1 (solid) and the highest energy Q-band normalized to 0.5 (dashed). (right) Normalized absorbance spectra showing the lowest energy Q-bands of the model compound 3 (dashed) and 1 (solid) are included for comparison.

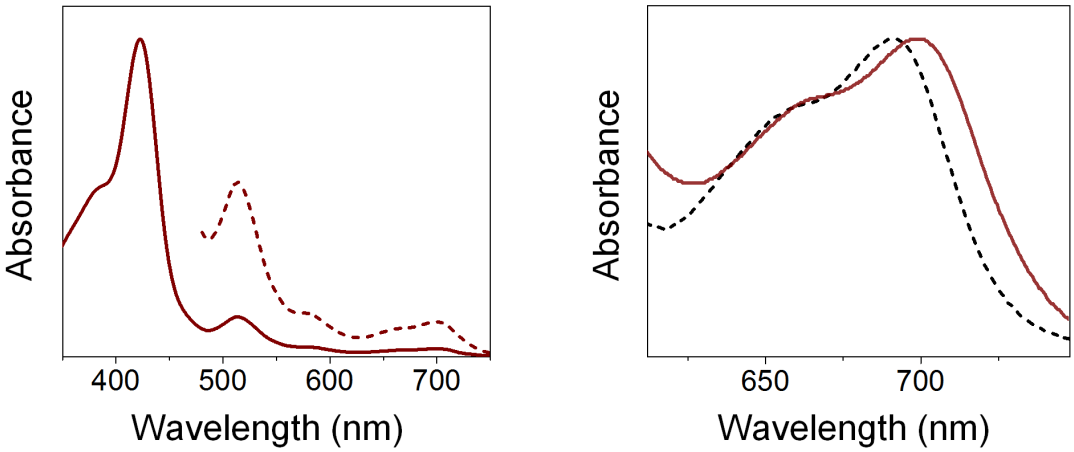

Figure 6.8. (left) Absorbance spectra of 2 recorded in toluene showing the Soret band normalized to 1 (solid) and the highest energy Q-band normalized to 0.5 (dashed). (right) Normalized absorbance spectra showing the lowest energy Q-bands of the model compound 4 (dashed) and 2 (solid) are included for comparison.

GATR-FTIR

Grazing angle attenuated total reflection Fourier transform infrared spectroscopy (GATR-FTIR) was performed using a VariGATR accessory (Harrick Scientific) with a Ge crystal plate installed in a Bruker Vertex 70. A minimum of 4 individual wafers were tested for each sample. Samples were pressed against the Ge crystal to ensure effective optical coupling. Spectra were collected under a dry nitrogen purge with a 4 cm^{-1} resolution, GloBar MIR source, a broadband KBr beamsplitter, and a liquid nitrogen cooled MCT detector. Background measurements were obtained from the bare Ge crystal and the data were processed using OPUS software. Spectra from model compounds in pressed KBr pellets were acquired with the same settings but using transmission mode. GATR measurements were baseline corrected for rubberband scattering.

ICP-MS

Inductively coupled plasma mass spectroscopy (ICP-MS) was performed on a Thermo-Finnigan Neptune ICP-MS. The samples were run in kinetic-energy discrimination (KED) mode. The ICP-MS samples were prepared by immersing a CoP|GaP wafer into 1000 μL of concentrated Omni trace H_2SO_4 solution and heating the solution at 60 ºC for 20 min, followed by sonicating the solution for 1 h. The solution was then diluted to 0.5 M H_2SO_4 by taking 108 μL of the 1000 μL solution and diluting to 4000 μL. Three different wafers of CoP|GaP were analyzed. Unfunctionalized GaP substrates were analyzed as controls. The trace amounts of cobalt in these controls were averaged and subtracted from the CoP|GaP cobalt concentrations.

Electrochemical Measurements

Cyclic voltammetry was performed with a Biologic potentiostat using a glassy carbon (3 mm diameter) disk, a platinum counter electrode, and a silver wire pseudoreference

electrode in a conventional three-electrode cell at a scan rate of 250 mV s^{-1}. Anhydrous dimethylformamide or butyronitrile (Aldrich) was used as the solvent for electrochemical measurements. The supporting electrolyte was 0.1 M tetrabutylammonium hexafluorophosphate. The solution was sparged with argon. The working electrode was cleaned between experiments by polishing with alumina (50 nm diameter) slurry, followed by solvent rinses.

Photoelectrochemical Studies

Photoelectrochemical (PEC) measurements were performed using 100 mW cm^{-2} illumination from a 100 W Oriel Solar Simulator equipped with an AM1.5 filter. Linear sweep voltammetry and three-electrode electrolysis (chronoamperometry) were performed with a Biologic potentiostat using a platinum coil counter electrode, a Ag/AgCl, NaCl (3 M) reference electrode (0.21 V vs NHE), and GaP working electrodes (including GaP following buffered HF treatment, cobalt porphyrin-modified GaP, and iron porphyrin-modified GaP) in a modified cell containing a quartz window. A minimum of four individual wafers were tested for each sample. The supporting electrolyte was 0.1 M phosphate buffer (pH 7). Linear sweep voltammograms were recorded at sweep rates of 100 mV s^{-1} under a continuous flow of 5% hydrogen in nitrogen. Open-circuit photovoltages were determined by the zero current value in the linear sweep voltammograms. Chronoamperometry was performed with the working electrode polarized at 0 V vs RHE, where E vs RHE = E vs NHE + 0.05916 V x pH = E vs Ag/AgCl + 0.05916 V x pH + 0.21 V.

Product Detection

Gas analysis was performed via gas chromatography (GC) using an Agilent 490 Micro GC equipped with a 5 Å MolSieve column at a temperature of 80 °C and argon as the

carrier gas. Gas samples were syringe injected using 5 mL aliquots of headspace gas collected with a gas-tight Hamilton syringe from a sealed PEC cell both prior to and following 30 min of three-electrode photoelectrolysis using a cobalt porphyrin-modified working electrode polarized at 0 V vs RHE or following 6 min of three-electrode photoelectrolysis using an iron porphyrin-modified working electrode polarized at 0 V vs RHE. Prior to the experiment the cell was purged for 30 min with argon before sealing. The retention time of hydrogen was confirmed using a known source of hydrogen obtained from a standard lecture bottle containing a hydrogen and argon mixture. In Figure 2.13, the relative signal intensity is based on the ratio of total hydrogen molecules produced to half the number of net electrons passed from the counter to the working electrode. Thus, the signal areas are representative of the relative Faradaic efficiencies for hydrogen production.

6.3 Experimental Procedures for Chapter 3

Materials

All reagents and solvents including N-bromosuccinamide, acetone, 4-vinylphenyl boronic acid, potassium carbonate, tetrakis(triphenylphosphine)palladium(0), cobalt(II) acetate were purchased from Aldrich. Dichloromethane, methanol, hexanes, dimethylformamide and toluene were freshly distilled before use. Reactions were performed under argon atmosphere unless otherwise stated. Milli-Q water (18.2 MΩ·cm) was used to prepare all aqueous solutions.

Synthesis

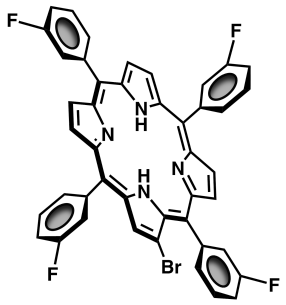

2-bromo-5,10,15,20-tetrakis(3-fluorophenyl) porphyrin (7). 5,10,15,20-tetrakis(3-fluorophenyl) porphyrin (80 mg, 0.12 mmol) was dissolved in a mixture of dichloromethane and methanol (9/1, v/v, 20 mL) and the solution was stirred and heated to reflux. After 25 min, a solution of N-bromosuccinamide (23 mg, 1.28 mmol, dissolved in 20 mL of a mixture of dichloromethane and methanol (9/1, v/v) was added dropwise over 35 min to the refluxing mixture. The reaction was quenched with acetone (10 mL), and the solvent evaporated at reduced pressure. The crude residue was purified by column chromatography on silica using a mixture of 3:2 hexanes and chloroform as the eluent to give the desired product (45%). ^{1}H NMR (400 MHz, $CDCl_3$): δ –2.94 (2H, s, NH), 7.47–7.57 (4H, m, ArH), 7.64–7.76 (4H, m, ArH), 7.78–8.01 (8H, m, ArH), 8.75–8.95 (7H, m, βH); UV-Vis (CH_2Cl_2) 419, 515, 548, 590, 645 nm; MALDI-TOF-MS *m/z* calcd. for $C_{44}H_{25}BrF_4N_4$ 764.12 and 766.12 obsd. 763.83 and 765.89.

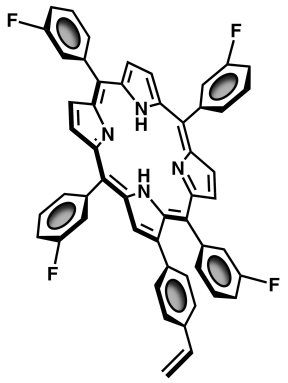

5,10,15,20-tetrakis(3-fluorophenyl)-2-(4-vinylphenyl) porphyrin (8). 4-vinylphenyl boronic acid (4-VPBA) (71 mg, 0.5 mmol), potassium carbonate (133 mg, 1 mmol) and tetrakis(triphenylphosphine)palladium(0) (11 mg, 0.01 mmol) were added to a solution containing 2-bromo-5,10,15,20-tetrakis(3-fluorophenyl)porphyrin (73 mg, 0.1 mmol) dissolved in toluene (25 mL) under an argon atmosphere. The reaction was heated to reflux and the progress of the reaction was monitored via thin-layer chromatography. The reaction was stopped following consumption of the porphyrin starting material (4 h) and the mixture was washed with a saturated solution of aqueous sodium bicarbonate then a saturated solution of aqueous sodium chloride. The organic phase was dried over sodium sulfate, filtered, and the solvent evaporated at reduced pressure. The residue was purified by column chromatography on silica using a mixture of 1:1 dichloromethane and hexanes as the eluent to yield the desired product (58%). ^{1}H NMR (400 MHz, $CDCl_3$): δ –2.72 (2H, s, NH), 5.30 (1H, d, *J* = 12 Hz, CH), 5.78 (1H, d, *J* = 20 Hz, CH), 6.76 (1H, dd, *J* = 20 Hz, *J* = 12 Hz, CH) 7.02 (1H, td, *J* = 8 Hz, *J* = 2 Hz, ArH), 7.20 (1H, q, ArH), 7.26 (2H, d, *J* = 8 Hz, ArH), 7.33 (2H, d, *J* = 8 Hz, ArH), 7.44–7.62 (4H, m, ArH), 7.64–7.77 (4H, m, ArH), 7.90–8.04 (6H, m, ArH), 8.69–8.90 (7H, m, βH);
UV-Vis (CH_2Cl_2) 419, 516, 550, 591, 647 nm; MALDI-TOF-MS *m/z* calcd. for $C_{52}H_{32}F_4N_4$ 788.26 obsd. 788.00.

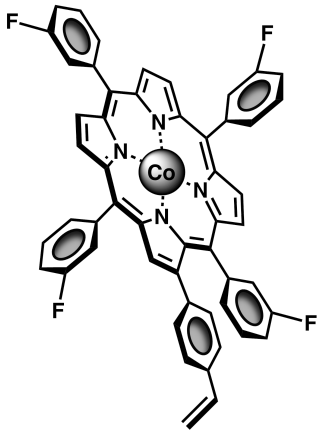

Cobalt(II) 5,10,15,20-tetrakis(3-fluorophenyl)-2-(4- vinylphenyl)porphyrin (9). A mixture containing 5,10,15,20-tetrakis(3-fluorophenyl)-2-(4-vinylphenyl) porphyrin (15 mg, 0.02 mmol) and cobalt(II) acetate (34 mg, 0.2 mmol) in dimethylformamide (23 mL) was stirred at reflux for 20 min. Upon cooling, the mixture was washed with a saturated solution of aqueous sodium bicarbonate then a saturated solution of aqueous sodium chloride and extracted with dichloromethane. The organic phase was dried over sodium sulfate, filtered, and the solvent evaporated at reduced pressure. The residue was purified by column chromatography on alumina using dichloromethane as eluent to give the desired product (98%). UV-Vis (CH_2Cl_2) 412, 532 nm; MALDI-TOF-MS *m/z* calcd. for $C_{52}H_{30}CoF_4N_4$ 845.17 obsd. 844.96; EPR (CH_2Cl_2): (g_x = 2.081, g_y = 2.020, g_z = 1.966). FTIR (KBr): 936, 955, 1004, 1077, 1111, 1151, 1168, 1185, 1200, 1264, 1304, 1330, 1347, 1401, 1430, 1444, 1480, 1583, 1610 cm^{-1}.

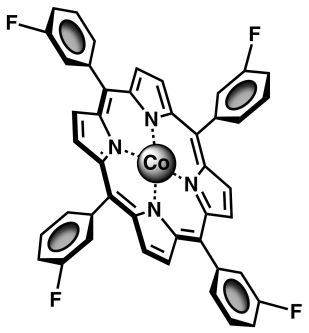

Cobalt(II) 5,10,15,20-tetrakis(3-fluorophenyl)porphyrin (10). A mixture containing 5,10,15,20-tetrakis(3-fluorophenyl) porphyrin (50 mg, 0.073 mmol) and cobalt(II) acetate (129 mg, 0.73 mmol) in dimethylformamide (70 mL) was stirred at reflux for 20 min. Upon cooling, the mixture was washed with a saturated solution of aqueous sodium bicarbonate then with a saturated solution of aqueous sodium chloride and extracted with dichloromethane. The organic phase was dried over sodium sulfate, filtered, and the solvent evaporated at reduced pressure. The residue was purified by column chromatography on alumina using dichloromethane as eluent. Recrystallization from dichloromethane/hexanes gave the target compound (96%). UV-Vis (CH_2Cl_2) 408, 527 nm; MALDI-TOF-MS *m/z* calcd. for $C_{44}H_{24}CoF_4N_4$ 743.13 obsd. 742.79.

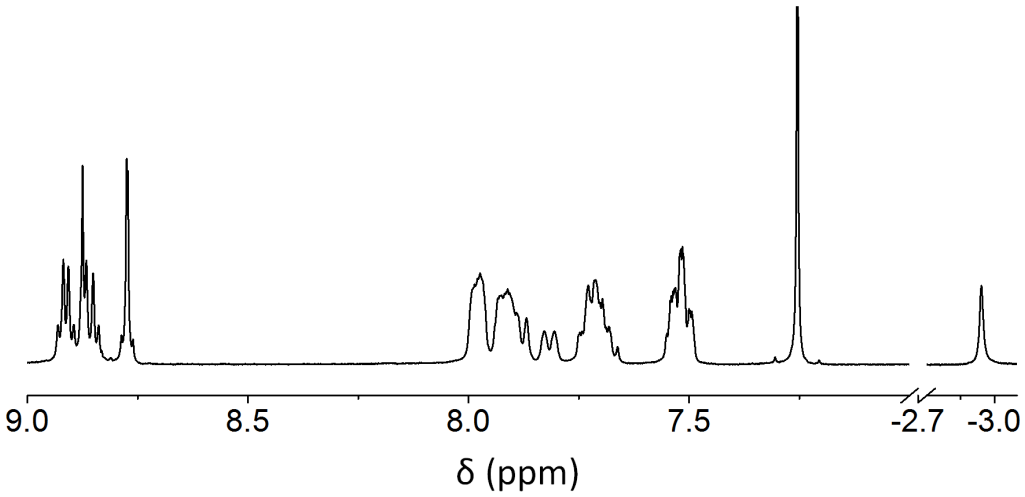

Figure 6.9. 400 MHZ ^{1}H NMR spectrum of 2-bromo-5,10,15,20-tetrakis(3-fluorophenyl) porphyrin (7) recorded in chloroform-d. ^{1}H NMR (400 MHz, $CDCl_3$): δ –2.94 (2H, s, NH), 7.47–7.57 (4H, m, ArH), 7.64–7.76 (4H, m, ArH), 7.78–8.01 (8H, m, ArH), 8.75–8.95 (7H, m, βH).

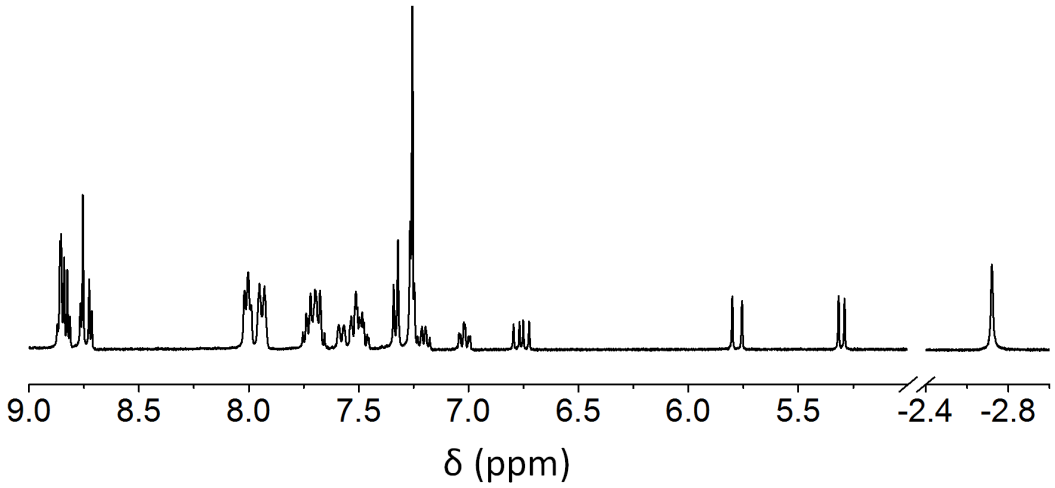

Figure 6.10. 400 MHZ ^{1}H NMR spectrum of 5,10,15,20-tetrakis(3-fluorophenyl)-2-(4-vinylphenyl) porphyrin (8) recorded in chloroform-d. ^{1}H NMR (400 MHz, $CDCl_3$): δ – 2.72 (2H, s, NH), 5.30 (1H, d, *J* = 12 Hz, CH), 5.78 (1H, d, *J* = 20 Hz, CH), 6.76 (1H, dd, *J* = 20 Hz, *J* = 12 Hz, CH) 7.02 (1H, td, *J* = 8 Hz, *J* = 2 Hz, ArH), 7.20 (1H, q, ArH), 7.26 (2H, d, *J* = 8 Hz, ArH), 7.33 (2H, d, *J* = 8 Hz, ArH), 7.44–7.62 (4H, m, ArH), 7.64–7.77 (4H, m, ArH), 7.90–8.04 (6H, m, ArH), 8.69–8.90 (7H, m, βH).

NMR

^{1}H, ^{13}C, and ^{19}F nuclear magnetic resonance spectra were recorded on a *Varian* NMR spectrometer operating at 400 MHz at room temperature. All ^{1}H and ^{13}C NMR chemical shifts (ppm) are reported relative to $Si(CH_3)_4$ as an internal standard. ^{19}F data are reported relative to $C_6H_5CF_3$ (–63.77 ppm).

Electrochemical Analysis

Cyclic voltammetry measurements were performed with a *Biologic* potentiostat using a glassy carbon (3 mm diameter) disk, a platinum counter electrode, and a silver wire pseudo-reference electrode in a conventional three-electrode cell at a scan rate of 500 mV s^{-1} at room temperature under argon. Anhydrous n-butyronitrile (*Aldrich*) was used as the solvent for electrochemical measurements. The supporting electrolyte was 0.1 M tetrabutylammonium hexafluorophosphate. The potential of the pseudo reference electrode was determined using the ferrocenium/ferrocene redox couple as an internal standard with $E_{1/2}$ taken as 0.48 V vs SCE.[5]

EPR

Electron paramagnetic resonance (EPR) studies were performed at the EPR Facility of Arizona State University. Continuous wave EPR spectra were recorded using an *ELEXSYS E580 CW X-band* spectrometer (*Bruker*, Rheinstetten, Germany) equipped with a *Model 900 EPL* liquid helium cryostat. For the measurements of 9, the magnetic field modulation frequency was 100 kHz, the amplitude was 1 mT, the microwave power was 0.25 mW, the microwave frequency was 9.44 GHz, the sweep time was 84 s, and the temperature was 4 K. The EPR spectrum was simulated using *EasySpin* (*version 5.1.10*), a computational package developed by Stoll and Schweiger (2006) and based on *Matlab* (*The MathWorks*, Massachusetts, USA). The model used for the EPR simulations

considered a low-spin ^{59}Co(II) ion (S = 1/2, I = 7/2). The fitting parameters were the *g*-values (g_x, g_y, and g_z) and the line widths (ΔB_x, ΔB_y, and ΔB_z). The fitting procedure was similar to the one previously described by Flores and coworkers.[6]

6.4 Experimental Procedures for Chapter 4

Materials

All reagents were purchased from Sigma-Aldrich. Dichloromethane, methanol, and toluene were freshly distilled before use. All semiconductors were purchased from University Wafers. Milli-Q water (18.2 MΩ·cm) was used to prepare all aqueous solutions.

The preparation of porphyrins used in this study, including cobalt(II) 5,10,15,20-tetrakis(3-fluorophenyl)porphyrin (10), cobalt(II) 5,10,15,20-tetrakis(3-fluorophenyl)-2-(4-vinylphenyl)porphyrin (9), cobalt(II) 5,10,15,20-tetra-*p*-tolylporphyrin (3), and cobalt(II) 5,10,15,20-tetra-*p*-tolyl-2-(4-vinylphenyl)porphyrin (1) described in Chapters 2 and 3.

GaP(100) wafers

The semiconductor supports used in this work are single crystalline p-type Zn-doped gallium phosphide (100) wafers that are single side polished to an epi-ready finish. The wafers have a resistivity of 0.16 Ω·cm, a mobility of 69 $cm^2\ V^{-1}\ s^{-1}$, and a carrier concentration of $4.5 \times 10^{17}\ cm^{-3}$, with an etch pit density of less than $5 \times 10^4\ cm^{-2}$.

Sample preparation

Diced gallium phosphide samples were etched with buffered hydrofluoric acid and dried under nitrogen prior to wet chemical treatment with an argon-sparged solution of the neat monomer 4-vinylpyridine or 1 mM of 5,10,15,20-tetrakis(3-fluorophenyl)-2-(4-

vinylphenyl)porphyrin, 9, under UV-light (254 nm) for 2 h. The samples were rinsed with methanol and dried under argon to yield samples of PVP|GaP and CoT3FPP|GaP, respectively. PVP|GaP samples were exposed to a 1 mM solution of cobalt(II) 5,10,15,20-tetrakis(3-fluorophenyl)porphyrin, 10, in toluene for 12 h to yield CoT3FPP|PVP|GaP samples that were rinsed with toluene and dried under nitrogen.

6.5 Experimental Procedures for Chapter 5

Materials

All reagents and solvents including, acetone, chloroform, methanol, sodium bicarbonate, sodium chloride, copper(II) acetate were purchased from Aldrich. Dichloromethane, methanol, hexanes, dimethylformamide and toluene were freshly distilled before use. Reactions were performed under argon atmosphere unless otherwise stated. Milli-Q water (18.2 MΩ·cm) was used to prepare all aqueous solutions.

Synthesis

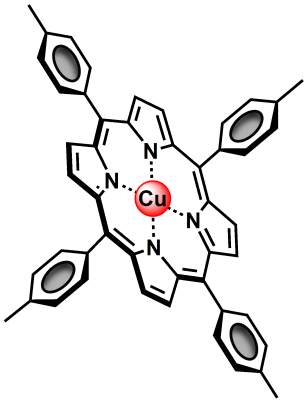

Copper(II) 5,10,15,20-tetra-*p*-tolylporphyrin (CuP). CuP was prepared following a modified version of previously reported procedures.[7-9] A mixture containing 5,10,15,20-tetra-*p*-tolylporphyrin (50 mg, 0.075 mmol) and copper(II) acetate (95 mg, 0.53 mmol) in a solution of chloroform (35 mL) and methanol (5 mL) was stirred at reflux for 15 h. Upon cooling, the mixture was washed with a saturated solution of aqueous sodium bicarbonate, then with a saturated solution of aqueous sodium chloride, before extracting with dichloromethane. The organic phase was dried over sodium sulfate, filtered, and the solvent evaporated at reduced pressure. The residue was purified by column chromatography on alumina using dichloromethane as the eluent. Recrystallization from dichloromethane/methanol gave the target compound (96%).

Fourier transform infrared (FTIR), electron paramagnetic resonance (EPR), and UV–Vis absorption spectroscopies coupled with mass spectrometry confirm successful synthesis of the target compounds and the data obtained using these methods are in agreement with previous reports.[7-9]

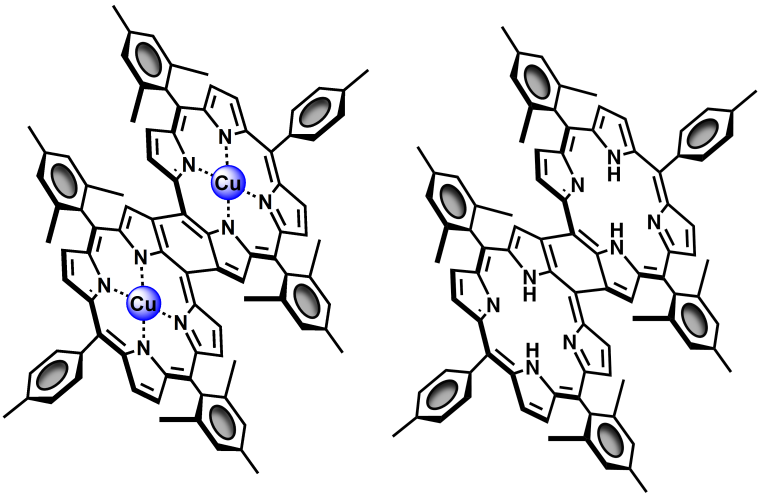

Bicopper(II) *meso*-β doubly-fused 5,24-di(*p*-tolyl)-10,19,29,38-tetramesitylporphyrin (Cu_2FP) (left) and ***meso*-β doubly-fused 5,24-di(*p*-tolyl)-10,19,29,38-tetramesitylporphyrin (FBFP)** (right) were prepared using previously reported methods.[10]

Nuclear magnetic resonance (NMR) and UV–Vis absorption spectroscopies coupled with mass spectrometry confirm successful synthesis of the target compounds and the data obtained using these methods are in agreement with previous reports. Additional characterization of Cu_2FP was performed using Fourier transform infrared and electron paramagnetic resonance spectroscopies.

FTIR (KBr): 1610, 1506, 1450, 1379, 1358, 1327, 1230, 1209, 1182, 1161, 1065, 1003 cm^{-1}. EPR (CH_2Cl_2) (g_x= 2.021).

UV-Vis-NIR and UV-Vis-NIR-SEC

All ultraviolet-visible-near-infrared (UV-Vis-NIR) spectra were recorded on a Shimadzu SolidSpec-3700 spectrometer with a deuterium lamp for the ultraviolet range and a WI (halogen) lamp for the visible and near-infrared. Ultraviolet-visible-near-infrared

spectroelectrochemistry (UV-Vis-NIR-SEC) measurements were performed in benzonitrile using a Biologic potentiostat. Measurements of the Cu_2FP and CuP complexes were recorded in anhydrous benzonitrile using a Pt honeycomb design working electrode, a Pt counter electrode, and a silver wire pseudoreference electrode. The supporting electrolyte was 0.1 M $TBAPF_6$. The solution was sparged with argon. Thin layer constant potential electrolysis was monitored via UV-Vis-NIR as the working electrode was polarized in a stepwise manner (i.e. an incrementally increasing bias potential versus the silver wire reference). Before changing the electrode polarization, absorption spectra were continuously collected at each applied potential until there were no significant changes in the resulting absorption spectra. This procedure was repeated until increasing the polarization no longer resulted in significant changes between UV-Vis-NIR spectra collected prior to and following the potential step. The Pt honeycomb electrode was cleaned between experiments by collecting cyclic voltammograms in 0.1 M H_2SO_4, followed by rinsing with 18.2 MΩ·cm water and then acetone. The potential of the pseudoreference electrode was determined by measuring the ferrocenium/ferrocene redox couple under identical solvent conditions before and after completion of the measurements.

FTIR and IR-SEC

All Fourier transform infrared (FTIR) spectroscopy was performed using a Bruker Vertex 70. Spectra were collected (64 scans) with a 4 cm^{-1} resolution, GloBar MIR source, a broadband KBr beamsplitter, and a liquid nitrogen cooled MCT detector.

Infrared spectroelectrochemistry (IR-SEC) measurements were performed in dichloromethane using a Biologic potentiostat connected to a custom optically

transparent thin-layer electrochemical cell (pathlength : 0.2 mm) equipped with NaCl optical windows and purchased from professor Frantisek Hartl, University of Reading. The cell contained a Pt mesh counter electrode, a silver wire pseudoreference electrode, and a Pt mesh working electrode. The Pt mesh working electrode was positioned within the light path of the IR spectrophotometer. The cell and its contents were sealed under an argon atmosphere prior to all measurements, and thin layer constant potential electrolysis was monitored via FTIR as the working electrode was polarized in a step-wise manner (i.e. an incrementally increasing bias potential versus the silver wire reference). Before changing the electrode polarization, absorption spectra were continuously collected at each applied potential until there were no significant changes in the resulting absorption spectra. This procedure was repeated until increasing the polarization no longer resulted in significant changes between FTIR spectra collected prior to and following the potential step. The cell was disassembled and cleaned between experiments by rinsing the cell components first with water, followed by acetone, and finally dichloromethane. A drop of nitric acid was placed on the Pt mesh working electrode for approximately 5-10 min before rinsing with water.

EPR

Electron paramagnetic resonance (EPR) studies were performed at the EPR Facility of Arizona State University Continuous wave (CW) EPR spectra were recorded using an ELEXSYS E580 CW X-band spectrometer (Bruker, Rheinstetten, Germany) equipped with a Model 900 EPL liquid helium cryostat (Oxford Instruments, Oxfordshire, UK). For the measurements of monomeric copper(II) porphyrin, the magnetic field modulation frequency was 100 kHz, the amplitude was 0.5 mT, the microwave power was 1 mW, the microwave frequency was 9.44 GHz, the sweep time was 168 s, and the temperature was

30 K. For the fused copper(II) porphyrins, the experimental spectra were measured using a magnetic field modulation amplitude of 1 mT and a microwave power of 64 μW at a temperature of 40 K.

Spin Hamiltonian. The EPR spectrum of the monomeric Cu porphyrin was analyzed considering a single Cu(II) ion (S = 1/2). Thus, the EPR data was fit using a spin Hamiltonian, *H*, containing the electron Zeeman interaction with the applied magnetic field B_o, and the hyperfine coupling (hfc) interactions with one ^{63,65}Cu (I = 3/2), four equivalent ^{14}N (I = 1) and one ^{1}H (I = 1/2):[11]

$$H = \beta_e S.g.\mathrm{B}_o + h\,S.A^{Cu}.I^{Cu} + \sum_{i=1}^{4} h\,S.A^{N_i}.I^{N_i} + h\,S.A^{H}.I^{H} \qquad \text{Eq. 1}$$

where S is the electron spin operator, I^{Cu}, I^{N_i} and I^{H} are the nuclear spin operators of a ^{63,65}Cu, four equivalent ^{14}N and a ^{1}H, respectively, A^{Cu}, A^{N_i} and A^{H} are the corresponding hfc tensors in frequency units, g is the electronic *g*-tensor, β_e is the electron magneton, and *h* is Planck's constant.

The EPR spectrum of the fused copper(II) porphyrins was analyzed considering two equivalent Cu(II) ions (S = 1/2) interacting with two equivalent ^{63}Cu nuclei. In this case, only the electron Zeeman term and the hfc interactions with two equivalent ^{63}Cu (I = 3/2) nuclei were included in the spin Hamiltonian since hfc interactions with ^{14}N and ^{1}H are not resolved in the spectrum.

Fitting of EPR spectra. To quantitatively compare experimental and simulated spectra, we divided the spectra into N intervals, i.e., we treated the spectrum as an N-dimensional vector R. Each component R_j has the amplitude of the EPR signal at a magnetic field B_j, with j varying from 1 to N. The amplitudes of the experimental and simulated spectra

were normalized so that the span between the maximum and minimum values of R_j is 1. We compared the calculated amplitudes R_j^{calc} of the signal with the observed values R_j defining a root-mean-square deviation σ by:

$$\sigma(p_1, p_2, \ldots, p_n) = [\sum_j (R_j^{calc}(p_1, p_2, \ldots, p_n) - R_j^{exp})^2/N]^{1/2} \quad \text{Eq. 2}$$

where the sums are over the N values of j, and p's are the fitting parameters that produced the calculated spectrum. For our simulations, N was set equal to 2048. The EPR spectra were simulated using EasySpin (version 5.1.10), a computational package developed by Stoll and Schweiger[12] and based on Matlab (The MathWorks, Massachusetts, USA). EasySpin calculates EPR resonance fields using the energies of the states of the spin system obtained by direct diagonalization of the spin Hamiltonian (see Eq. 1). The EPR fitting procedure used a Monte Carlo type iteration to minimize the root-mean-square deviation, σ (see Eq. 2) between measured and simulated spectra. We searched for the optimum values of the following parameters: the principal components of g (i.e., g_x, g_y, and g_z), the principal components of the hfc tensors A^{Cu} (i.e., A_x^{Cu}, A_y^{Cu}, A_z^{Cu}), A^{N_i} (i.e., $A_x^{N_i}$, $A_y^{N_i}$, $A_z^{N_i}$) and A^H (i.e., A_x^H, A_y^H, A_z^H), and the peak-to-peak line-widths (ΔB_x, ΔB_y and ΔB_z).

Electrochemistry

All voltammetry measurements were performed with a Biologic potentiostat using a glassy carbon (3 mm or 1 mm diameter) disk, a platinum counter electrode, and a silver wire pseudoreference electrode in a conventional three-electrode cell at scan rates between 50-900 mV s^{-1} at room temperature under argon. The argon gas stream

(ultrahigh purity) was introduced to the electrochemical cell using PEEK tubing connected to a pre-bubbler containing dichloromethane, saturating the inert gas with solvent vapors. The potential of the pseudoreference electrode was determined using the ferrocenium/ferrocene redox couple as an internal standard. Dichloromethane (distilled over CaH_2) and anhydrous benzonitrile (Aldrich) were used as solvents for electrochemical measurements. Electrochemical analysis grade $TBAPF_6$ electrolyte was obtained from Aldrich and stored in a desiccator containing $CaSO_4$ as a desiccant. The supporting electrolyte concentration for all electrochemical measurements was 0.1 M $TBAPF_6$.

Determination of HA/H_2 via OCP Measurements. All measurements were conducted following a previously reported procedure and experimental setup.[13]

Rotating Ring-Disk Experiment

All measurements were performed in a cell sparged for 20 min with argon, and then blanketed with argon throughout the experiments. Before any ring currents were measured, the Pt ring was polished by hand with a 3 μm followed by a 1 μm diamond slurry on a Nylon polishing cloth, and then again with a 1 μm diamond slurry on a Microcloth polishing pad, followed by rinsing and sonication in 18.2 MΩ·cm water. The collection efficiency was independently determined by oxidizing $K_4FeII(CN)_6$ at the glassy carbon working electrode (5 mm diameter) and reducing $K_4FeIII(CN)_6$ at the platinum ring.

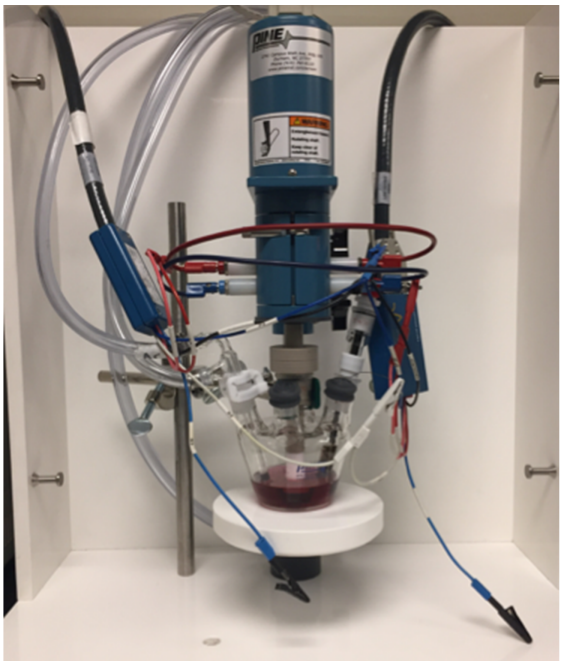

Figure 6.11. Photograph of the electrochemical setup used for rotating ring-disk experiments.

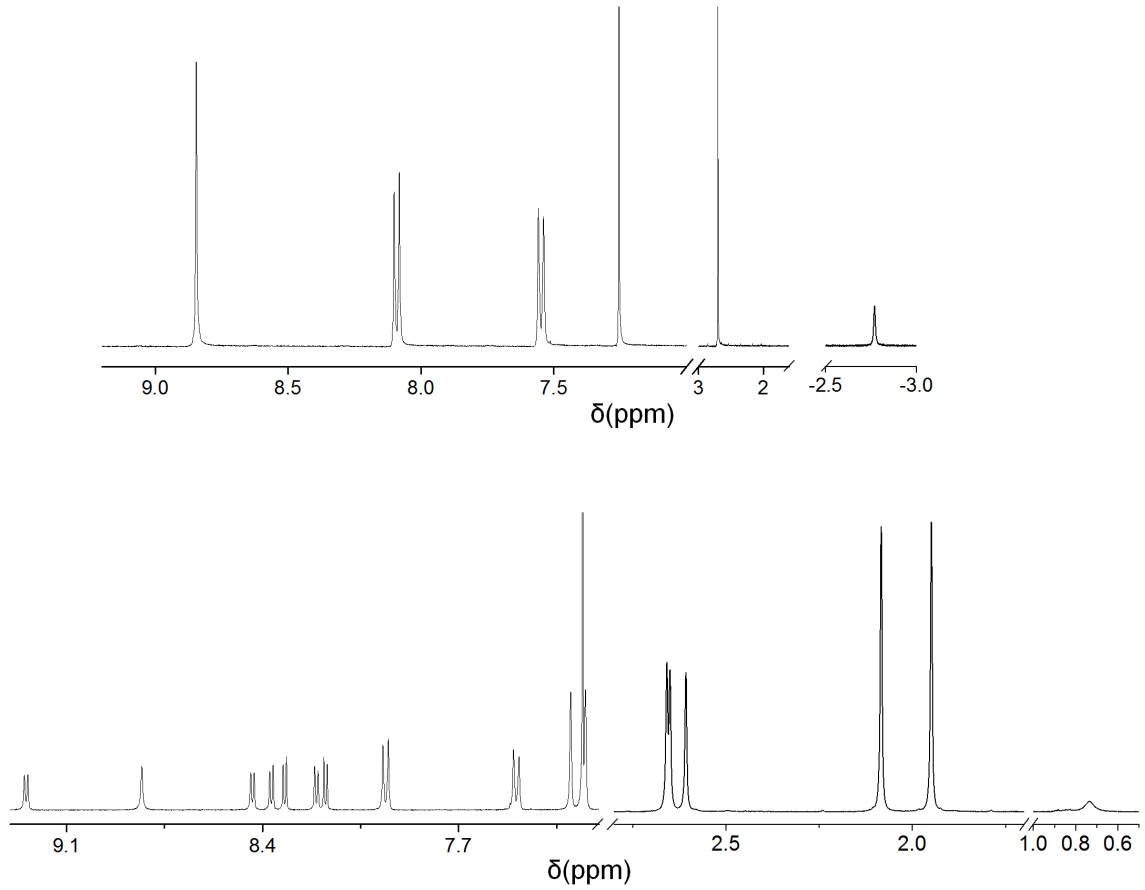

Figure 6.12. ^{1}H NMR spectra of (top) 5,10,15,20-tetra-*p*-tolylporphyrin and (bottom) *meso*-β doubly-fused 5,24-di(*p*-tolyl)-10,19,29,38-tetramesitylporphyrin in chloroform-d.

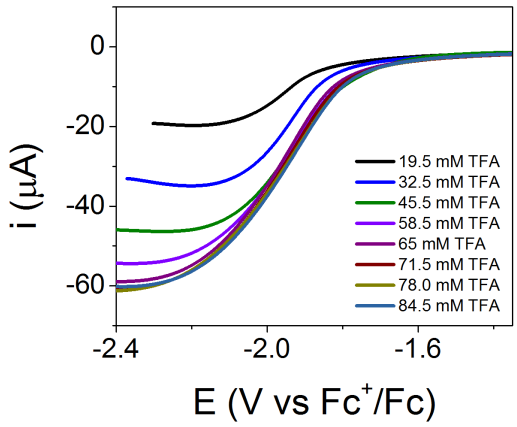

Figure 6.13. Voltammograms of Cu_2FP (0.01 mM) collected in a 0.1 M $TBAPF_6$ dichloromethane solution under argon with an increasing amount of TFA (19.5–84.5 mM) and at a scan rate of 600 mV s^{-1}.

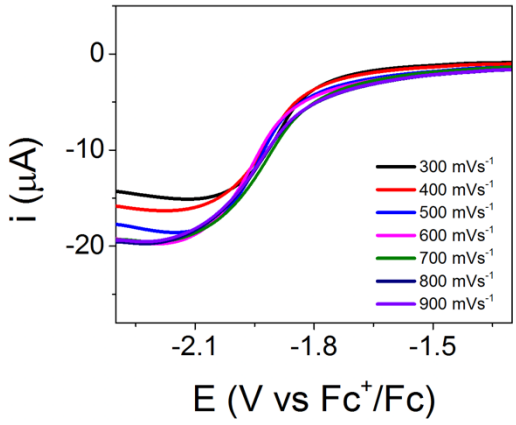

Figure 6.14. Voltammograms of Cu_2FP (0.01 mM) collected in a 0.1 M $TBAPF_6$ dichloromethane solution under argon with TFA (19.5 mM) and at scan rates of 300–900 mV s^{-1}.

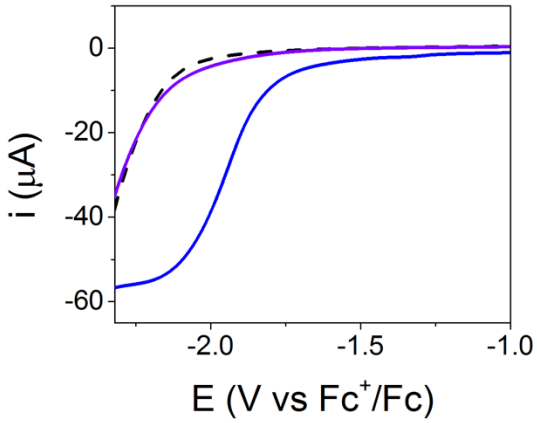

Figure 6.15. Linear sweep voltammograms recorded using a glassy carbon working electrode in a 0.01 mM Cu_2FP solution (blue solid) or in a solution without Cu_2FP present, following collection of the blue linear sweep voltammogram and rinsing the electrode surface with fresh dichloromethane (purple solid).

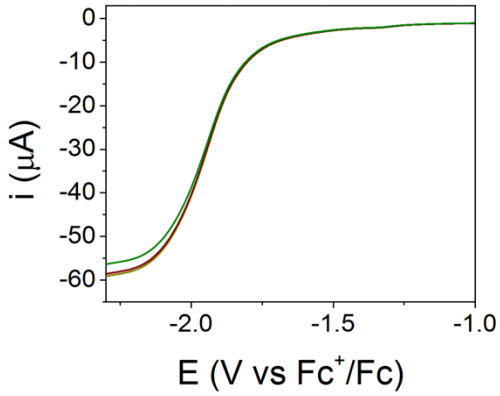

Figure 6.16. Voltammograms of 0.01 mM Cu_2FP recorded in a 0.1 M $TBAPF_6$ dichloromethane solution at a scan rate of 600 mV s^{-1} with 65 mM TFA using either a 3 mm glassy carbon disk (yellow) or a platinum wire (maroon and green) as the counter electrode.

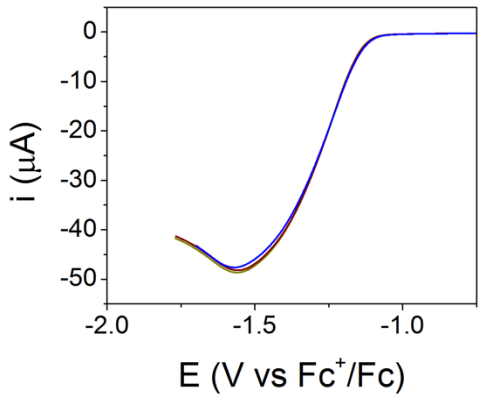

Figure 6.17. Voltammograms of 0.1 mM Cu_2FP recorded in a 0.1 M $TBAPF_6$ dichloromethane solution at a scan rate of 600 mV s^{-1} with 65 mM TFA using either a 3 mm glassy carbon disk (yellow) or a platinum wire (maroon and blue) as the counter electrode.

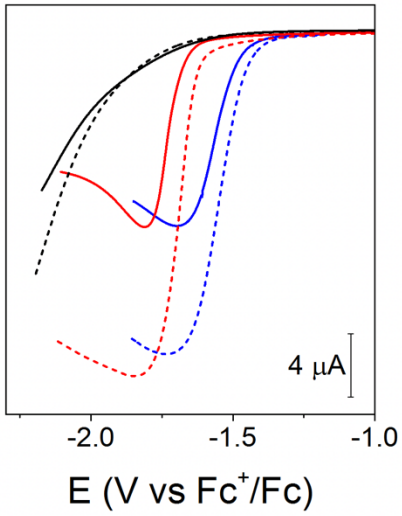

Figure 6.18. Voltammograms of 0.01 mM Cu_2FP (blue) and 0.01 mM CuP (red) recorded in a 0.1 M $TBAPF_6$ dichloromethane solution at a scan rate of 100 mV s^{-1} with either 16.25 mM (solid) or 32.5 mM (dashed) TFA. Voltammograms recorded using porphyrin-free solutions of 0.1 M $TBAPF_6$ in dichloromethane at a scan rate of 100 mV s^{-1} (black), with either 16.25 mM (solid) or 32.5 mM (dashed) TFA, are included for comparison. All voltammograms were recorded using a 1 mm diameter glassy carbon

working electrode at room temperature and the ferrocenium/ferrocene redox couple as an internal reference.

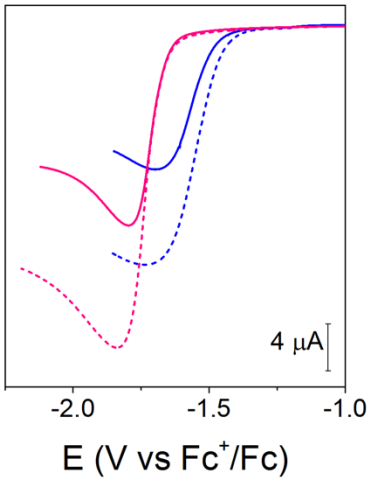

Figure 6.19. Voltammograms of 0.01 mM Cu_2FP (blue) and 0.02 mM CuP (pink) recorded in a 0.1 M $TBAPF_6$ dichloromethane solution at a scan rate of 100 mV s^{-1} with either 16.25 mM (solid) or 32.5 mM (dashed) TFA.

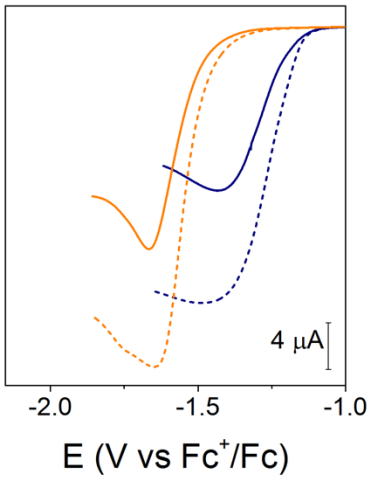

Figure 6.20. (b) Voltammograms of 0.1 mM Cu_2FP (dark blue) and 0.2 mM CuP (orange) recorded in a 0.1 M $TBAPF_6$ dichloromethane solution at a scan rate of 100 mV s^{-1} with either 16.25 mM (solid) or 32.5 mM (dashed) TFA.

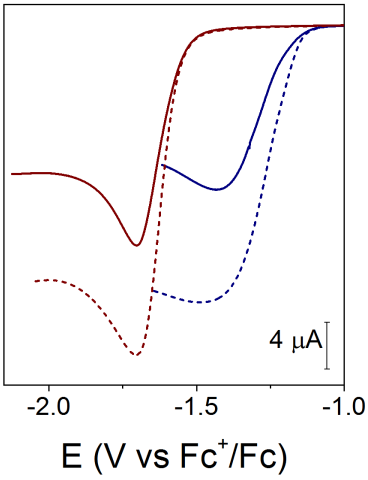

Figure 6.21. Voltammograms of 0.1 mM Cu_2FP (dark blue) and 0.1 mM CuP (dark red) recorded in a 0.1 M $TBAPF_6$ dichloromethane solution at a scan rate of 100 mV s^{-1} with either 16.25 mM (solid) or 32.5 mM (dashed) TFA.

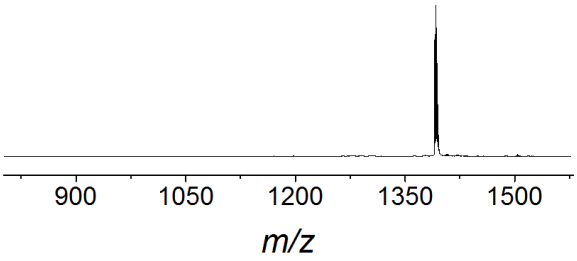

Figures 6.22. MALDI-TOF MS data collected using samples of Cu_2FP following 4 h of exposure to a solution of 87.5 mM TFA (7000 equivalents of TFA with respect to the concentration of Cu_2FP used in these experiments / 12.5 μM in Cu_2FP) in dichloromethane.

6.6 References

(1) Lee, C. H; Lindsey, J. S. One-Flask Synthesis of Meso-Substituted Dipyrromethanes Their Application in the Synthesis of Trans-Substituted Porphyrin Building Blocks. *Tetrahedron* **1994**, *50* (39), 11427–11440.

(2) Gao, G. Y.; Ruppel, J. V.; Allen, D. B.; Chen, Y.; Zhang, X. P. Synthesis of β-Functionalized Porphyrins via Palladium- Catalyzed Carbon - Heteroatom Bond Formations : Expedient Entry into β -Chiral Porphyrins. *JOC Artic*. **2007**, *7 2*(6), 906–9066.

(3) Chizhova, N. V.; Kumeev, R. S.; Mamardashvili, N. Zh. Synthesis and Spectral Properties of Cobalt (II) and Cobalt (III) Tetraarylporphyrinates. *Russ. J. Inorg. Chem*. **2013**, *58* (6), 740–743.

(4) Sun, Z.-C.; She, Y.-B.; Zhou, Y.; Song, X.-F.; Li, Kai. Synthesis, Characterization and Spectral Properties of Substituted Tetraphenylporphyrin Iron Chloride Complexes. *Molecules* **2011**, *16* (4), 2960–2970.

(5) Gobi, K. V.; Tokuda, K.; Ohsaka, T. Electrochemical and Spectroscopic Studies on Nickel(II/III) Complexes with Novel 14-membered Hexaaza Macrocycle Functionalized with Propenyl Groups. *Electrochim. Acta* **1998***, 43* (9), 1013–1022.

(6) Flores, M.; Isaacson, R.; Abresch, E.; Calvo, R.; Lubitz, W.; Feher, G. Protein-Cofactor Interactions in Bacterial Reaction Centers from *Rhodobacter sphaeroides* R-26: II. Geometry of the Hydrogen Bonds to the Primary Quinone Q_A^- by ^1H and ^2H ENDOR Spectroscopy. *Biophys. J.* **2007**, *92* (2), 671–682.

(7) Hariprasad, G.; Dahal, S.; Maiya, B. G. *Meso*-Substituted Octabromoporphyrins: Synthesis, Spectroscopy, Electrochemistry and Electronic Structure. *J. Chem. Soc., Dalton Trans.* **1996**, *16*, 3429–3436.

(8) Gervaldo, M.; Fungo, F.; Durantini, E. N.; Silber, J. J.; Sereno, L.; Otero, L. Carboxyphenyl Metalloporphyrins as Photosensitizers of Semiconductor Film Electrodes. A Study of the Effect of Different Central Metals. *J. Phys. Chem. B* **2005**, *109* (44), 20953–20962.

(9) Ye, L.; Ou, Z.; Fang, Y.; Xue, S.; Song, Y.; Wang, L.; Wang, M; Kadish, K. M. Electrochemistry of Nonplanar Copper(II) Tetrabutano- and Tetrabenzotetraarylporphyrins in Nonaqueous Media. *RSC Adv.* **2015**, *5* (94), 77088–77096.

(10) Brennan, B. J.; Arero, J.; Liddell, P. A.; Moore, T. A.; Moore, A. L.; Gust, D. Selective Oxidative Synthesis of *Meso*-beta Fused Porphyrin Dimers. *J. Porphyrins Phthalocyanines* **2013**, *17* (4), 247–251.

(11) Weil, J. A.; Bolton, J. R. Electron Paramagnetic Resonance: Elementary Theory and Practical Applications. *John Wiley & Sons*. **2007**.

(12) Stoll, S.; Schweiger, A. J. EasySpin, a Comprehensive Software Package for Spectral Simulation and Analysis in EPR. *Magn. Reson*. **2006**, *178* (1), 42–55.

(13) Roberts, J. A.; Bullock, R. M. Direct Determination of Equilibrium Potentials for Hydrogen Oxidation/Production by Open Circuit Potential Measurements in Acetonitrile. *Inorg. Chem.* **2013**, *52* (7), 3823−3835.

COMPLITE BIBLIOGRAPHY

(1) *IPCC* 5th Assessment Report, Geneva, Switzerland, **2014**.

(2) Faunce, T. A.; Lubitz, W.; Rutherford, A. W.; MacFarlane, D.; Moore, G. F.; Yang, P.; Nocera, D. G.; Moore, T. A.; Gregory, D. H.; Fukuzumi, S.; et al. Energy and Environment Policy Case for a Global Project on Artificial Photosynthesis. *Energy Environ. Sci.* **2013**, *6* (3), 695–698.

(3) Rockström, J.; Steffen, W.; Noone, K.; Persson A.; Chapin, F. S.; Lambin, E. F.; Lenton, T. M.; Scheffer, m.; Folke, C.; Schellnhuber, H. J.; Nykvist, B. A Safe Operating space for Humanity. *Nature* **2009**, *461*, 472–475.

(4) Steffen, W.; Richardson, K.; Rockström, J.; Cornell, S. E.; Fetzer, I.; Bennett, E. M.; Biggs, R.; Carpetner, S. R.; de Vries, W.; de Wit, C. A.; Folke, C.; Gerten, D.; Heinke, J.; Mace, G. M.; Persson, L. M.; Ramanathan, V.; Reyers, B.; Sörlin, S. Planetary Boundaries: Guiding Human Development on a Changing Planet. *Science* **2015**, *347* (6223), 736–746.

(5) Ardo, S.; Rivas, D. F.; Modestino, M. A.; Greiving, V. S.; Abdi, F. F.; Llado, E. A.; Artero, V.; Ayers, K.; Battaglia, C.; Becker, J-P.; et al. Pathways to Electrochemical Solar-Hudrogen Technologies. *Energy Environ. Sci.* **2018**, *11* (10), 2768–2783.

(6) Vesborg, P. C.; Jaramillo, T. F. Addressing the Terawatt Challenge: Scalability in the Supply of Chemical Elements for Renewable Energy. *RSC Adv.* **2012**, *2* (21), 7933−7947.

(7) The Role of the Chemical Sciences in Finding Alternatives to Critical Resources: A Workshop Summary. National Research Council. National Academies Press. **2012**.

(8) Auwärter, W.; Écija, D.; Klappenberger, F.; Barth, J. V. Porphyrins at Interface. *Nat. Chem.* **2015**, *7*, 105−120.

(9) Morris, A. J.; Meyer, G. J.; Fujita, E. Molecular Approach to the Photocatalytic reduction of Carbon Dioxide for Solar Fuels. *Acc. Chem. Res*. **2009**, *42* (12), 1983−1994.

(10) Lin, S.; Diercks, C. S.; Zhang, Y.-B.; Kornienko, N.; Nichols, E. M.; Zhao, Y.; Paris, A. R.; Kim, D.; Yang, P.; Yaghi, O. M.; Chang, C. J. Covalent Organic Frameworks Comprising Cobalt Porphyrins for Catalytic CO_2 Reduction in Water. *Science* **2015**, *349* (6253), 1208−1213.

(11) Rigsby, M. L.; Wasylenko, D. J.; Pegis, M. L.; Mayer, J. M. Medium Effect Are as Important as Catalyst Design for Selectivity in Electrocatalytic Oxygen reduction by Iron-Porphyrin Complexes. *J. Am. Chem. Soc*. **2015**, *137* (13), 4296−4299.

(12) Swierk, J. R.; Méndez- Hernández, D. D.; McCool, N. S.; Liddell, P.; Terazono, Y.; Pahk, I.; Tomlin, J. J.; Oster, N. V.; Moore, T. A.; Moore, A. L.; Gust, D.; Mallouk, T. E. Metal-Free Organic Sensitizers for Use in Water-Splitting Dye-Sensitized Photoelectrochemical Cells. *Proc. Natl. Acad. Sci. U. S. A.* **2015**, *112* (6), 1681−1686.

(13) Costentin, C.; Robert, M.; Savéant, J.-M. Current Issues in Molecular Catalysis Illustrated by Iron Porphyrins as Catalysts of the CO_2-to-CO Electrochemical Conversion. *Acc. Chem. Res.* **2015**, *48* (12), 2996−3006.

(14) Ahrenholtz, S. R.; Epley, C. C.; Morris, A. J. Solvothermal Preparation of an Electrocatalytic Metalloporphyrin MOF Thin Film and its Redox Hopping Charge-Transfer Mechanism. *J. Am. Chem. Soc.* **2014**, *136* (6), 2464−2472.

(15) Yao, S. A.; Ruther, R. E.; Zhang, L.; Franking, R. A.; Hamers, R. J.; Berry, J. F. Covalent Attachment of Catalyst Molecules to Conductive Diamond: CO2 Reduction Using "Smart" Electrodes. *J. Am. Chem. Soc.*, **2012**, *134* (38) 15632−15635.

(16) Lindsey, J. S.; Bocian, D. F. Molecules for Charge-Based Information Storage. *Acc. Chem. Res.*, **2011**, *44* (8) 638−650.

(17) Civic, M. R.; Dinolfo, P. H. Electrochemical Rectification of Redox Mediators Using Porphyrin-Based Molecular multilayered Films on ITO electrodes. *ACS Appl. Mater. Interfaces* **2016**, *8* (31), 20465−20473.

(18) *Basic Research Needs for Catalysis Science to Transform Energy Technologies*, U.S. Department of Energy: Basic Energy Science Workshop Report; U.S. Government Printing Office: Washington, DC, 2017.

(19) Grunes, J.; Zhu, J.; Somorjai, G. A. Catalysis and Nonoscience. *Chem. Commun*. **2003**, *18*, 2257−2260.

(20) Kamat, P. V.; Tvrdy, K.; Baker, D. R.; Radich, J. G. Beyond Photovoltaics: Semiconductor Nanoarchitectures for Liquid-Junction Solar Cells. *Chem. Rev.* **2010**, *110* (11), 6664–6688.

(21) Nocera, D. G. Solar Fuels and Solar Chemicals Industry. *Acc. Chem. Res.* **2017**, *50* (3), 616–619.

(22) Hambourger, M.; Moore, G. F.; Kramer, D. M.; Gust, D.; Moore, A. L.; Moore, T. A. Biology and Technology for Photochemical Fuel Production. *Chem. Soc. Rev.* **2009**, *38* (1), 25–35.

(23) Moore, G. F.; Brudvig, G. W. Energy Conversion in Photosynthesis: A Paradigm for Solar Fuel Production. *Annu. Rev. Condens. Matter Phys.* **2011**, *2* (1), 303–327.

(24) Benson, E. E.; Kubiak, C. P.; Sathrum, A. J.; Smeieja, J. M. Electrocatalytic and Homogeneous Approaches to Conversion of CO_2 to Liquid Fuels. *Chem. Soc. Rev.* **2009**, *38* (1), 89–99.

(25) Kumar, B.; Llorente, M.; Froehlich, J.; Dang, T.; Sathrum, A.; Kubiak, C. P. Photochemical and Photoelectrochemical Reduction of CO_2. *Annu. Rev. Phys. Chem.* **2012**, *63*, 541–569.

(26) Ye, R.; Zhao, J.; Wickemeyer, B. B.; Toste, F. D.; Somorjai, G. A. Foundations and Strategies of the Construction of Hybrid Catalysts for Optimized Performance. *Nat. Catal.* **2018**, *1* (5), 318–325.

(27) Wang, M.; Yang, Y.; Shen, J.; Jiang, J.; Sun, L. Visible-Light-Absorbing Semiconductor/Molecular Catalyst Hybrid Photoelectrodes for H_2 or O_2 Evolution: Recent Advances and Challenges. *Sustain. Energy Fuels* **2017**, *1* (8), 1641–1663.

(28) Queyriaux, N.; Kaeffer, N.; Morozan, A.; Chavarot-Kerlidou, M.; Artero, V. Molecular Cathode and Photocathode Materials for Hydrogen Evolution in Photoelectrochemical Devices. *J. Photochem. Photobiol. C Photochem. Rev.* **2015**, *25*, 90–105.

(29) Wen, F.; Li, C. Hybrid Artificial Photosynthetic Systems Comprising Semiconductors as Light Harvesting and Biomimetic Complexes as Molecular Cocatalysts. *Acc. Chem. Res.* **2013**, *46* (11), 2355–2364.

(30) Bullock, R. M.; Das, A. K.; Appel, A. M. Surface Immobilization of Molecular Electrocatalysts for Energy Conversion. *Chem. - A Eur. J.* **2017**, *23* (32), 7626–7641.

(31) Jiao, J.; Yu, M.; Holten, D.; Lindsey, J. S.; Bocian, D. F. Characterization of Hydroporphyrins Covalently Attached to Si(100). *J. Porphyrins and Phthalocyanines* **2017**, *21*, 453–464.

(32) McKone, J. R.; Marinescu, S. C.; Brunschwig, B. S.; Winkler, J. R.; Gray, H. B. Earth-Abundant Hydrogen Evolution Electrocatalysts. *Chem. Sci.* **2014**, *5*, 865–878.

(33) Mizuno, N.; Misono, M. Heterogeneous Catalysis. *Chem. Rev.* **1998**, *98* (1), 199–218.

(34) Armstrong, F. A.; Hirst, J. Reversibility and Efficiency in Electrocatalytic Energy Conversion and Lessons From Enzymes. *Proc. Natl. Acad. Sci. U. S. A.* **2011**, *108* (34), 14049–14054.

(35) Rakowski DuBois, M.; Dubois, D. L. The Role of the First and Second Coordination Spheres in the Design of Molecular Catalysts for H_2 Production and Oxidation. *Chem. Soc. Rev.* **2009**, 38, 62–72.

(36) Cracknell, J. A.; Vincent, K. A.; Armstrong, F. A. Enzymes as Working or Inspirational Electrocatalysts for Fuel Cells and Electrolysis. *Chem. Rev.* **2008**, *108* (7), 2439–2461.

(37) Helm, M. L.; Stewart, M. P.; Bullock, R. M.; DuBois, M. R.; DuBois, D. L. A Synthetic Nickel Electrocatalyst with a Turnover Frequency Above 100,000 s^{-1} for H_2 Production. *Science* **2011**, *333* (6044), 863–866.

(38) Ginovska-Pangovska, B.; Dutta, A.; Reback, M. L.; Linehan, J. C.; Shaw, W. J. Beyond the Active Site: The Impact of the Outer Coordination Sphere on Electrocatalysts for Hydrogen Production and Oxidation. *Acc. Chem. Res.* **2014**, *47* (8), 2621–2630.

(39) Bacchi, M.; Berggren, G.; Niklas, J.; Veinberg, E.; Mara, M. W.; Shelby, M. L.; Poluektov, O. G.; Chen, L. X.; Tiede, D. M.; Cavazza, C.; Field, M. J.; Fontecave, M.; Artero, V. Cobaloxime-Based Artificial Hydrogenases. *Inorg. Chem.* **2014**, *53* (15), 8071–8082.

(40) Dutta, A.; Ginovska, B.; Raugei, S.; Roberts, J. A.; Shaw, W. J. Optimizing Conditions for Utilization of an H_2 Oxidation Catalyst with Outer Coordination Sphere Functionalities. *Dalton Trans.* **2016**, *45*, 9786–9793.

(41) Wiese, S.; Kilgore, U. J.; Ho, M.-H.; Raugei, S.; DuBois, D. L.; Bullock, R. M.; Helm, M. L. Hydrogen Production Using Nickel Electrocatalysts with Pendant Amines: Ligand Effects on Rates and Overpotentials. *ACS Catal.* **2013**, *3* (11), 2527–2535.

(42) Tsay, C.; Yang, J. Y. Electrocatalytic Hydrogen Evolution Under Acidic Aqueous Conditions and Mechanistic Studies of a Highly Stable molecular Catalyst. *J. Am. Chem. Soc.* **2016**, *138* (43), 14174–14177.

(43) Maher, A. G.; Passard, G.; Dogutan, D. K.; Halbach, R. L.; Anderson, B. L.; Gagliardi, C. J.; Taniguchi, M.; Lindsey, J. S.; Nocera, D. G. Hydrogen Evolution Catalysis by a Sparsely Substituted Cobalt Chlorin. *ACS Catal.* **2017**, *7* (5), 3597–3606.

(44) McCrory, C. C. L.; Uyeda, C.; Peters, J. C. Electrocatalytic Hydrogen Evolution in Acidic Water with Molecular Cobalt Tetraazamacrocycles. *J. Am. Chem. Soc.* **2012**, *134* (6), 3164–3170.

(45) Du, P.; Eisenberg, R. Catalysts Made of Earth-abundant Elements (Co, Ni, Fe) for Water Splitting: Recent Progress and Future Challenges. *Energy Environ. Sci.* ***2012***, *5* (3), 6012–6021.

(46) Karunadasa, H. I.; Chang, C. J.; Long, J. R. A Molecular Molybdenum-oxo Catalyst for Generation Hydrogen from Water. *Nature* **2010**, *464*, 1329–1333.

(47) Artero, V.; Savéant, J.-M. Toward the Rational Benchmarking of Homogeneous H_2- evolving Catalysts. *Energy Environ. Sci.* **2014**, *7* (11), 3808–3814.

(48) Kellet, R. M.; Spiro, T. G. Cobalt(I) Porphyrin Catalysis of Hydrogen Production from Water. *Inorg. Chem.* **1985**, *24* (15), 2373–2377.

(49) Behar, D.; Dhanasekaran, T.; Neta, P.; Hosten, C. M.; Ejeh, D.; Hambright, P.; Fujita, E. Cobalt Porphyrin Catalyzed Reduction of CO2. Radiation Chemical, Photochemical, and Electrochemical Studies. *J. Phys. Chem. A* **1998**, *102* (17), 2870–2877.

(50) Bhugun, I.; Lexa, D.; Savéant, J.-M. Homogeneous Catalysis of Electrochemical Hydrogen Evolution by Iron(0) Porphyrins. *J. Am. Chem. Soc.* **1996**, *118* (16), 3982–3983.

(51) Tsuda, A.; Osuka, A. A Fully Conjugated Porphyrin Tapes with Electronic Absorption Bands that Reach into Infrared. *Science* **2001**, *293* (5527), 79–82.

(52) Tsuda, A.; Furuta, H; Osuka, A. Syntheses, Structural Characterizations, and Optical and Electrochemical Properties of Directly Fused Diporphyrins. *J. Am. Chem. Soc.* **2001**, *123* (42), 10304−10321.

(53) Kim, D.; Osuka, A. Photophysical Properties of Directly Linked Linear Porphyrin Arrays. *J. Phys. Chem. A* **2003**, *107* (42), 8791−8816.

(54) Cheng, F.; Zhang, S.; Adronov, A.; Echegoyen, L.; Diederich, F. Triply Fused ZnII–Porphyrin Oligomers: Synthesis, Properties, and Supramolecular Interactions with Single-Walled Carbon Nanotubes (SWNTs). *Chem. - Eur. J.* **2006**, *12* (23), 6062−6070.

(55) Brennan, B. J.; Arero, J.; Liddell, P. A.; Moore, T. A.; Moore, A. L.; Gust, D. Selective Oxidative Synthesis of Meso-Beta Fused Porphyrin Dimers. *J. Porphyrins Phthalocyanines* **2013**, *17* (4), 247−251.

(56) Lin, S. Y.; DiMagno S. G.; Therien M. J. Highly Conjugated, Acetylenyl Bridged Porphyrins: New Models for Light-Harvesting Antenna Systems. *Science* **1994**, *264* (5162), 1105−1111.

(57) Anderson H. L. Building Molecular Wires from the Colours of Life: Conjugated Porphyrin Oligomers. *Chem. Commun*. **1999**, *23*, 2323−2330.

(58) Costentin, C.; Savéant, J. M. Towards an Intelligent Design of Molecular Electrocatalysts. *Nat. Rev. Chem.* **2017**, *1*, 0087.

(59) Pegis, M. L.; McKeown, B. A.; Kumar, N.; Lang, K.; Wasylenko, D. J.; Zhang, X. P.; Raugei, S.; Mayer, J. M. Homogeneous Electrocatalytic Oxygen Reduction Rates Correlate with Reaction Overpotential in Acidic Organic Solutions. *ACS Cent. Sci*. **2016**, *2* (11), 850−856.

(60) Bard, A.; Fox, M. A. Artificial Photosynthesis: Solar Splitting of Water to Hydrogen and Oxygen. *Acc. Chem. Res.* **1995**, *28* (3), 141–145.

(61) Blankenship, R. E.; Tiede, D. M.; Barber, J.; Brudvig, G. W.; Fleming, G.; Ghirardi, M.; Gunner, M. R.; Junge, W.; Kramer, D. M.; Melis, A.; et al. Comparing Photosynthetic and Photovoltaic Efficiencies and Recognizing the Potential for Improvement. *Science* **2011**, *332* (6031), 805–809.

(62) Tran, P. D.; Wong, L. H.; Barber, J.; Loo, J. S. C. Recent Advances in Hybrid Photocatalysts for Solar Fuel Production. *Energy Environ. Soc. Rev.* **2012**, *5* (3), 5902–5918.

(63) Swierk, J. R.; Mallouk, T. E. Design Development of Photoanodes for Water- splitting Dye-sensitized Photoelectrochemical Cells. *Chem. Soc. Rev.* **2013**, *42* (6), 2357–2387.

(64) Walter, M. G.; Warren, E. L.; McKone, J. R.; Boettcher, S. W.; Mi, Q.; Santori, E. a.; Lewis, N. S. Solar Water Splitting Cells. *Chem. Rev.* **2010**, *110* (11), 6446–6473.

(65) Downes, C. A.; Marinescu, S. C. Efficient Electrochemical and Photoelectrochemical H 2 Production from Water by a Cobalt Dithiolene One-Dimensional Metal–Organic Surface. *J. Am. Chem. Soc.* **2015**, jacs.5b07020.

(66) Krawicz, A.; Yang, J.; Anzenberg, E.; Yano, J.; Sharp, I. D.; Moore, G. F. Photofunctional Construct That Interfaces Molecular Cobalt-Based Catalysts for H2 Production to a Visible-Light-Absorbing Semiconductor. *J. Am. Chem. Soc.* **2013**, *135*, 11861–11868.

(67) Cedeno, D.; Krawicz, A.; Doak, P. Using Molecular Design to Control the Performance of Hydrogen-Producing Polymer-Brush-Modified Photocathodes. *J. Phys. Chem. Lett.* **2014**, *5* (18), 3222–3226.

(68) Kim, H. J.; Seo, J.;Rose, M. J. H_2 Photogeneration Using a Phosphonate-anchored Ni-PNP Catalyst on a Band-edge-modified p-Si(111)IAZO Construct. *ACS Appl. Mater. Interfaces*, **2016**, *8* (2), 1061–1066.

(69) Gu, J.; Yan, Y.; Young, J. L.; Steirer, K. X.; Neale, N. R.; Turner, J. A. Water Reduction by a P-$GaInP_2$ Photoelectrode Stabilized by an Amorphous TiO_2 Coating and a Molecular Cobalt Catalyst. *Nat. Mater.* **2016**, *15* (4), 456–460.

(70) Beiler, A. M.; Khusnutdinova, D.; Jacob, S. I.; Moore, G. F. Chemistry at the Interface: Polymer-Functionalized GaP Semiconductors for Solar Hydrogen Production. *Ind. Eng. Chem. Res.* **2016**, *55* (18), 5306–5314.

(71) Beiler, A. M.; Khusnutdinova, D.; Jacob, S. I.; Moore, G. F. Solar Hydrogen Production Using Molecular Catalysts Immobilized on Gallium Phosphide (111)A and (111)B Polymer-Modified Photocathodes. *ACS Appl. Mater. Interfaces* **2016**, *8* (15), 10038–10047.

(72) Kellett, R. M.; Spiro, T. G. Cobalt Porphyrin Electrode Films as H_2 Evolution Catalysts. *Inorg. Chem.* **1985**, *24* (15), 2378–2382.

(73) Maurin, A.; Robert, M. Noncovalent Immobilization of a Molecular Iron-based Electrocatalyst on Carbon Electrodes for Selective, Efficient CO_2-to-CO Conversion in Water. *J. Am. Chem. Soc.* **2016**, *138* (8), 2492–2495.

(74) Maurin, A.; Robert, M. Catalytic CO2-to-CO Conversion in Water by Covalently Functionalized Carbon Nanotubes with a Molecular Iron Catalyst. *Chem.Commun*. **2016**, *52* (81), 12084–12087.

(75) Weng, Z.; Jiang, J.; Wu, Y.; Wu, Z.; Guo, X.; Materna, K. L.; Liu, W.; Batista, V. S.; Brudvig, G. W.; Wang, H. Electrochemical CO_2 Reduction to Hydrocarbons on a Heterogeneous molecular Cu Catalyst in Aqueous Solution. *J. Am. Chem. Soc.* **2016**, *138* (26), 8076–8079.

(76) Beiler, A. M.; Khusnutdinova, D.; Wadsworth, B. L.; Moore, G. F. Cobalt Porphyrin-Polypyridyl Surface Coatings for Photoelectrosynthetic Hydrogen Production. *Inorg. Chem.* **2017**, *56* (20), 12178–12185.

(77) Rosenthal, J.; Luckett, T. D.; Hodgkiss, J. M.; Nocera, D. G. Photocatalytic Oxidation of Hydrocarbons by a Bis-iron(III)-μ-oxo Pacman Porphyrin Using O_2 and Visible Light. *J. Am. Chem. Soc.* **2006**, *128* (20), 6546–6547.

(78) Berben, L. A.; Peters, J. C. Hydrogen Evolution by Cobalt Tetraimine Catalysts Adsorbed on Electrode Surfaces. *Chem. Commun.* **2010**, *46* (3), 398–400.

(79) Rose, M. J.; Gray, H. B.; Winkler, J. R. Hydrogen Generation Catalyzed by Fluorinated Diglyoxime-iron Complexes at Low Overpotentials. *J. Am. Chem. Soc.* **2012**, *134* (20), 8310–8313.

(80) Dhanasekaran, T. Grodkowski, J.; Neta, P.; Hambright, P.; Fujita, E. p-Terphenyl-sensitized Photoreduction of CO_2 with Cobalt and Iron Porphyrins. Interaction between CO and Reduced Metalloporphyrins. *J. Phys. Chem. A*, **1999**, *103* (38), 7742–7748.

(81) Gooding, J. J.; Ciampi, S. The Molecular Level Modification of Surfaces: from Self-assembled Monolayers to Complex Molecular Assemblies. *Chem. Soc. Rev*. **2011**, *40* (5), 2704–2718.

(82) Vilan, A.; Cahen, D. Chemical Modification of Semiconductor Surfaces for Molecular Electronic. *Chem. Rev*. **2017**, *117* (5), 4624–4666.

(83) Forbes, M. D. E. What We Talk About When We Talk About Light. *ACS Cent. Sci.* **2015**, *1* (7), 354–363.

(84) Halmann, M. Photoelectrochemical Reduction of Aqueous Carbon Dioxide on P-Type Gallium Phosphide in Liquid Junction Solar Cells. *Nature* **1978**, *275*, 115–116.

(85) Grätzel, M. Photoelectrochemical Cells. *Nature* **2001**, *414*, 338–344.

(86) Liu, C.; Dasgupta, N. P.; Yang, P. Semiconductor Nanowires for Artificial Photosynthesis. *Chem. Mater.* **2014**, *26* (1), 415–422.

(87) Kaiser, B.; Fertig, D.; Ziegler, J.; Klett, J.; Hoch, S.; Jaegermann, W. Solar Hydrogen Generation with Wide-Band-Gap Semiconductors: GaP(100) Photoelectrodes and Surface Modification. *Chem. Phys. Chem* **2012**, *13* (12), 3053–3060.

(88) Barton, E. E.; Rampulla, D. M.; Bocarsly, A. B. Selective Solar-Driven Reduction of CO_2 to Methanol Using a Catalyzed. *J. Am. Chem. Soc.* **2008**, *130* (20), 6342–6344.

(89) Price, M. J.; Maldonado, S. Macroporous N-GaP in Nonaqueous Regenerative Photoelectrochemical Cells. *J. Phys. Chem. C* **2009**, *113* (28), 11988–11994.

(90) Liu, C.; Sun, J.; Tang, J.; Yang, P. Zn-Doped p-Type Gallium Phosphide Nanowire Photocathodes from a Surfactant-Free Solution Synthesis. *Nano Lett.* **2012**, *12* (10), 5407–5411.

(91) Standing, A.; Assali, S.; Gao, L.; Verheijen, M. A.; van Dam, D.; Cui, Y.; Notten, P. H. L.; Haverkort, J. E. M.; Bakkers, E. P. A. M. Efficient Water Reduction with Gallium Phosphide Nanowires. *Nature Communication.* **2015**, *6*, 7824–7831.

(92) Li, B.; Franking, R.; Landis, E. C.; Kim, H.; Hamers, R. J. Photochemical Grafting and Patterning of Biomolecular Layers onto TiO_2 Thin Films. *ACS Appl. Mater. Interfaces* **2009**, *1* (5), 1013–1022.

(93) Moore, G. F.; Sharp, I. D. A Noble-Metal-Free Hydrogen Evolution Catalyst Grafted to Visible Light-Absorbing Semiconductors. *J. Phys. Chem. Lett.* **2013**, *4* (4), 568–572.

(94) Richards, D.; Zemlyanov, D.; Ivanisevic, A. Assessment of the Passivation Capabilities of Two Different Covalent Chemical Modifications on GaP(100). *Langmuir* **2010**, *26* (11), 8141–8146.

(95) Seifert, M.; Koch, A. H. R.; Deubel, F.; Simmet, T.; Hess, L. H.; Stutzmann, M.; Jordan, R.; Garrido, J. A.; Sharp, I. D. Functional Polymer Brushes on Hydrogenated Graphene. *Chem. Mater.* **2013**, *25* (3), 466–470.

(96) Steenackers, M.; Gigler, A. M.; Zhang, N.; Deubel, F.; Seifert, M.; Hess, L. H.; Lim, C. H.; Loh, K. P.; Garrido, J. A.; Jordan, R.; et al. Polymer Brushes on Graphene. *J. Am. Chem. Soc.* **2011**, *133* (27), 10490–10498.

(95) Cicero, R. L.; Linford, M. R.; Chidsey, C. E. D. Photoreactivity of Unsaturated Compounds with Hydrogen-Terminated Silicon(111). *Langmuir* **2000**, *16* (13), 5688–5695.

(96) Sun, Z.-C.; She, Y.-B.; Zhou, Y.; Song X.-F.; Li, K. Synthesis, Characterization and Spectral Properties of Substituted Tetraphenylporphyrin Iron Chloride Complexes. *Molecules* **2011**,*16* (4), 2960–2970.

(97) Lu, X.; Geng, Z.; Wang, Y.; Lv, B.; Kang, J. Synthesis and Characterization of Three New Unsymmetrical Porphyrins and Their Cobalt Complexes. *Synth. React. Inorg. Met. Org. Chem.* **2002**, *32* (5), 843–851.

(98) Costa, A. A.; Ghesti, G. F.; Macedo, J. L.; Braga V. S.; Santos, M. M., Dias, J. A., Dias, S. L. Immobilization of Fe, Mn and Co Tetraphenylporphyrin Complexes in MCM-41 and their Catalytic Activity in Cyclohexene Oxidation Reaction by Hydrogen Peroxide. *J. of Mol. Cat. A* **2008**, *282* (1-2), 149–157.

(99) Karweik, D. H.; Winograd, N. Nitrogen Charge Distributions in Free-Base Porphyrins, Metalloporphyrins, and Their Reduced Analogues Observed by X-Ray Photoelectron Spectroscopy. *Inorg. Chem.* **1976**,*15* (10), 2336–2342.

(100) Flechtner, K.; Andreas Kretschmann, A.; Steinrück, H.-P.; Gottfried, J. M. NO-Induced Reversible Switching of the Electronic Interaction between a Porphyrin-Coordinated Cobalt Ion and Silver Surface. *J. Am. Chem. Soc.* **2007**,*129* (40), 12110–12111.

(101) Lipińska, M. E.; Novais, J. P.; Rebelo, S. L.-H.; Bachiller-Baeza, B.; Rodriguez-Ramos, I.; Guerrero-Ruiz, A.; Freire, C. Microwave Assisted Silylation of Graphite Oxide and Iron (III) Porphyrin Interaction. *Polyhedron* **2014**, *81*, 475–484.

(102) Oveisi, A. R.; Zhang, K.; Khorramabadi-zad, A.; Farha O. K.; Hupp, J. T. Stable and Catalytically Active Iron Porphyrin-Based Porous Organic Polymer: Activity as Both a Redox and Lewis Acid Catalyst. *Sci. Rep*. **2015**, *5*, 10621–10629.

(103) Shin, K.; Kramer, S. K.; Goff, H. M. Base-Promoted Autoreduction of Iron(III) Porphyrins in Dimethyl Sulfoxide Solution: Magnetic Resonance Spectroscopy of Hydroxoiron(II) Porphyrin Complexes. *Inorg. Chem.* **1987**, *26* (24), 4103–4106.

(104) Modi, S.; Shedbalkar, V. P.; Behere, D. V. Kinetics of Autoreduction of Iron(III) Porphyrins by Cyanide Ion. *Inorg. Chim. Acta* **1990**, *173* (1), 9–12.

(105) Balch, A. L.; Noll, B. C.; Olmstead, M. M.; Phillips, S. L. Structural and Spectroscopic Characterization of Iron(III) Dioxoporphodimethene Complexes and Their Autoreduction to an Iron(II) Complex in Pyridine. *Inorg. Chem.* **1996**, *35* (22), 6495–6506.

(106) Claire, T. N. St.; Balch, A. L. *In Situ* Monitoring of the Degradation of Iron Porphyrins by Dioxygen with Hydrazine as Sacrificial Reductant. Detection of Paramagnetic Intermediates in the Coupled Oxidation Process by ^{1}H NMR Spectroscopy. *Inorg. Chem*. **1999**, *38* (4), 684–691.

(107) DuBois, D. L.; Berning, D. E. Hydricity of Transition-Metal Hydrides and Its Role in CO_2 Reduction. *Appl. Organomet. Chem.* **2000**, *14*, 860–862.

(108) Creutz, C.; Chou, M. H. Hydricities of d^6 Metal Hydride Complexes in Water. *J. Am. Chem. Soc.* **2009**, *131* (8), 2794–2795.

(109) Connelly, S. J.; Wiedner, E. S.; Appel, A. M. Predicting the Reactivity of Hydride Donors in Water: Thermodynamic Constants fir Hydrogen. *Dalton Trans.* **2015**, *44*, 5933–5938.

(110) Barroso, M.; Cowan, A. J.; Pendlebury, S. R.; Grätzel, M.; Klug, D. R.; Durrant, J. R. The Role of Cobalt Phosphate in Enhancing the Photocatalytic Activity of α-Fe_2O_3 Toward Water Oxidation. *J. Am. Chem. Soc.* **2011**, *133* (38), 14868–14871.

(111) Lin, F.; Boettcher, S. W. Adaptive Semiconductor/Electrocatalyst Junctions in Water-Splitting Photoanodes. *Nat. Mater.* **2014**, *13* (1), 81–86.

(112) Thorne, J. E.; Li, S.; Du, C.; Qin, G.; Wang, D. Energetics at the Surface of Photoelectrodes and Its Influence on the Photoelectrochemical Properties. *J. Phys. Chem. Lett.* **2015**, *6* (20), 4083–4088.

(113) Klahr, B.; Gimenez, S.; Fabregat-Santiago, F.; Hamann, T.; Bisquert, J. Water Oxidation at Hematite Photoelectrodes: The Role of Surface Stets. *J. Am. Chem. Soc.* **2012**, *134* (9), 4294–4302.

(114) Waegele, M. M.; Chen, X.; Herlihy, D. M.; Cuk, T. How Surface Potential Determines the Kinetic of the First Hole Transfer of Photocatalytic Water Oxidation. *J. Am. Chem. Soc.* **2014**, *136* (30), 10632–10639.

(115) Nozik, A. J. Photoelectrolysis of Water Using Semiconducting TiO_2 Crystals. *Nature* **1975**, *257*, 383–386.

(116) Chen, Z.; Jaramillo, T.F.; Deutsch, T. G.; Kleiman-Shwarsctein, A.; Forman, A. J.; Gaillard, N.; Garland, R.; Takanabe, K.; Heske, C.; Sunkara, M.; et. al. Accelerating materials Development for Photoelectrochemical Hydrogen Production: Standards for Methods, Definitions, and Reporting Protocols. *J. Mater. Res*., **2010**, *25* (1), 3–16.

(117) Khusnutdinova, D.; Beiler, A. M.; Wadsworth B. L.; Jacob S. I.; Moore G. F. Metalloporphyrin-modified Semiconductors for Solar Fuel Production. *Chem. Sci.* **2017**, *8* (1), 253–259.

(118) O´Hagan, D.; Rzepa, H. S. Some Influences of Fluorine in Bioorganic Chemistry. *Chem. Commun.* **1997**, *7*, 645–652. *Nature* **1978**, *275*, 115–116.

(119) Chambers, R. D. Fluorine in Organic Chemistry. *Blackwell Publishing Ltd. Oxford.* **2004.**

(120) Gerig, J. T. Fluorin Magnetic Resonance in Biochemistry. *Biol. Magn. Reson., Springer*, *New York*, **1978**.

(121) Sykes, B. D.; Hull, W. E.; Snyder, G. H. Experimental Evidence for Role of Cross-relaxation in Proton Nuclear Magnetic Resonance Spin Lattice Relaxation Time Measurements in Proteins. *Biophys. J*. **1978**, 21 (2), 137–146.

(122) Toi, H.; Homma, M.; Suzuki, A.; Ogoshi, H. Paramagnetic ^{19}F N.M.R. Spectra of Iron(III) Porphyrins Substituted with CF_3 Groups and Reconstituted Myoglobin. *J. Chem. Soc. Chem. Comm.* **1985**, *24*, 1791–1792.

(123) Dalvit, C.; Vulpetti, A. Fluorine – Protein Interactions and ^{19}F NMR Isotopic Chemical Shifts: an Empirical Correlation with Implication for Drug Design. *Chem. Med. Chem.* **2011**, *6* (1), 104–114.

(124) Tierno, M. E.; Mead, D.; Asato, A. E.; Liu, R. S.; Sekiya, N.; Yoshihara, K.; Chang, C. W.; Nakanishi, K.; Govindjee, R.; Ebrey, T. G. 14-Fluorobacterio-rhodopsin and other Fluorinated and 14-substituted Analogues. An Extra, Unusually Red-shifted Pigment Formed During Dark Adaptation. *Biochemistry* **1990**, *29* (25), 5948–5953.

(125) Kim, C.-Y.; Chang, J. S.; Doyon, J. B.; Baird, T. T.; Fierke, C. A.; Jain, A.; Chrristianson, D. W. Contribution of Fluorine to Protein – Ligand Affinity in the Binding of Fluoro-aromatic Inhibitors to Carbonic Anhydrase II. *J. Am. Chem. Soc.* **2000**, *122* (49), 12125–12134.

(126) Yolder, N. C.; Kumar, K. Fluorinated Amino Acids in Protein Design and Engineering. *Chem. Soc. Rev.* **2002**, *31* (6), 335–341.

(127) Rosenthal ,J.; Luckett, T. D.; Hodgkiss, J. M.; Nocera, D. G. Photocatalytic Oxidation of Hydrocarbons by a Bis-iron(III)-μ-oxo Pacman Porphyrin Using O_2 and Visible Light. *J. Am. Chem. Soc.* **2006**, *128* (20), 6546–6547.

(128) Moore, G. F.; Hambourger, M.; Gervaldo, M.; Poluektov, O. G.; Rajh, T.; Gust, D.; Moore, T.A.; Moore, A. L. A Bioinspired Construct that Mimics the Proton Coupled Electron Transfer between $P680^{*}+$ and the Tyr(Z)-His 190 Pair of Photosystem II. *J. Am. Chem. Soc.* **2008**, *130* (32), 10466–10467.

(129) Moore, G. F.; Konezny, S. J.; Song, H.; Milot, R. L.; Blakemore, J. D.; Minjoo, L. L.; Batista, V. S.; Schmuttenmaer, C. A.; Crabtree, R. H.; Brudvig, G. W. Bioinspired High-potential Porphyrin Photoanodes. *J. Phys. Chem. C* **2012**, *116* (7), 4892–4902.

(130) Najafpour, M. M.; Shen, J.-R.; Barber, J.; Moore, G. F. Running on Sun. *Chem. World* **2012**, 43.

(131) Faunce, T. A.; Styring, S.; Wasielewski, M. R.; Brudvig, G. W.; Rutherford, A. W.; Messinger, J.; Lee, A. F.; Hill, C. L.; DeGroot, H.; Fontecave, M.; et al. Artificial Photosynthesis as a Frontier Technology for Energy Sustainability. *Energy Environ. Sci.* **2013**, *6* (4), 1074.

(132) Hou, H. J. M.; Najafpour, M. M.; Moore, G. F.; Allakhverdiev, S. I. Photosynthesis: Structures, Mechanisms, and Applications. *Springer*, *New York* **2017**, 321–358.

(133) Moore, G. F. Concluding Remarks and Future Perspectives: Looking Back and Moving Forward. *Springer*, *New York* **2017**, 407–414.

(134) Adler, A. D.; Longo, F. R.; Finarelli, J. D.; Goldmacher, J.; Assour, J.; Korsakoff, L.A Simplified Synthesis for Meso-tetraphenylporphyrin. *J. Org. Chem.* **1967**, *32* (2), 476–476.

(135) Tomkowicz, Z.; Rams, M.; Bałanda, M.; Foro, S.; Nojiri, H.; Krupskaya, Y.; Kataev, V.; Büchner, B.; Nayak, S. K.; Yakhni, J. V.; Haase, W. Slow Magnetic Relaxations in Manganese(III) Tetra(*meta*-fluorophenyl)-porphyrin-tetracyanoethenide. Composition with the Relative Single Chain Magnet *ortho* Compound. *Inorg. Chem.* **2012**, *51* (18), 9983–9994.

(136) Alben, J. O.; Choi, S. S.; Adler, A. D.; Caughey, W. S. Infrared Spectroscopy of Porphyrins. *Ann. NY Acad. Sci.* **1973**, *206*, 278–295.

(137) Boucher, L. J.; Katz, J. J. The Infrared Spectra of Metalloporphyrins (4000–160 cm^{-1}). *J. Am. Chem. Soc.* **1967**, *89* (6), 1340–1345.

(138) Kincaid, J.; Nakamoto, K. Vibrational Spectra of Transition Metal Complexes of Tetraphenylporphine. *J. Inorg. Nucl. Chem*. **1975**, *37* (1), 85–89.

(139) Nguyen, K.; Day, P. N.; Pachter, R. Effects of Halogenation on the Ionized and Excited States of Free-base and Zinc Porphyrins. *J. Chem. Phys.* **1999**, *110*, 9135–9144.

(140) Sun, H.; Smirnov, V.; DiMagno, S. G. Slow Electron Transfer Rates for Fluorinated Cobalt Porphyrins: Electronic and Conformational Factors Modulating Metalloporphyrin ET. *Inorg. Chem.* **2003**, *42* (19), 6032–6040.

(141) Słota, R.; Broda, M. A.; Dyrda, G.; Ejsmont, K.; Mele, G. Structural and Molecular Characterization of *meso*-substituted Zinc Porphyrins: a DFT Supported Study. *Molecules* **2011**, *16* (12), 9957–9971.

(142) Kadish, K. M.; Caemelbecke, E. V. Electrochemistry of Porphyrins and Related Macrocycles. *J. Solid State Electrochem.* **2003**, *7* (5), 254–258.

(143) Lyaskovskyy, V.; de Bruin, B. Redox Non-innocent Ligands: Versatile New Tools to Control Catalytic Reactions. *ACS Catal.* **2012**, *2* (2), 270–279.

(144) Luca, O. R.; Crabtree, R. H. Redox-active Ligands in Catalysis. *Chem. Soc. Rev.* **2013**, *42* (4), 1440–1459.

(145) Chapman, R. D.; Fleischer, E. B. Direct Measurement of Electron Self-exchange Rates of Cobalt Porphyrins. 1. Outer-sphere Exchange. *J. Am. Chem. Soc.* **1982**, *104* (6), 1575–1582.

(146) Milosevic, M; Milosevic, V.; Berets, S.L. Grazing Angle Attenuated Total Reflection Spectroscopy: Fields at the Interface and Source of the Enhancement. *Appl. Spectrosc.* **2007**, *61*, 530–536.

(147) Milosevic, M. Internal Reflection and ATR Spectroscopy. *Applied Spectroscopy Reviews* **2004**, *39* (3), 365−384.

(148) Mulcahy, M. E.; Berets, S. L.; Milosevic, M.; Michl, J. Enhanced Sensitivity in Single-reflection Spectroscopy of Organic Monolayers on Metal Substrates (Pseudo-ATR). *J. Phys. Chem. B* **2004**, *108* (5), 1529–1521.

(149) O'Leary, L. E.; Johansson, E.; Brunschwig, B.S.; Lewis, N.S. Synthesis and Characterization of Mixed Methyl/Allyl Monolayers on Si(111). *J. Phys. Chem. B* **2010**, *114* (45), 14298–14302.

(150) Johansson, E.; Hurley, P. T.; Brunschwig, B. S.; Lewis, N. S. Infrared Vibrational Spectroscopy of Isotopically Labeled Ethyl-Terminated Si(111) Surfaces Prepared Using a Two-Step Chlorination/Alkylation Procedure. *J. Phys. Chem. B* **2009**, *113* (34), 15239–152455.

(151) Lummerstorfer, T.; Hoffmann, H. IR Reflection Spectra of Monolayer Films Sandwiched between Two High Refractive Index Materials. *Langmuir* **2004**, *20* (16), 6542–6545.

(152) Lummerstorfer, T.; Hoffmann, H. Click Chemistry on Surfaces: 1,3-Dipolar Cycloaddition Reactions of Azide-Terminated Monolayers on Silica. *J. Phys. Chem. B* **2004**, *108* (13), 3963–3966

(153) Lummerstorfer, T.; Kattner, J.; Hoffmann, H. Monolayers at Solid–solid Interfaces Probed with Infrared Spectroscopy. *Anal. Bioanal. Chem.* **2007**, *388* (1), 55–64.

(154) Wadsworth, B. L.; Beiler, A. M.; Khusnutdinova, D.; Jacob, S. I.; Moore, G. F. Electrocatalytic and Optical Properties of Cobaloxime Catalysts Immobilized at a Surface-Grafted Polymer Interface. *ACS Catal.* **2016**, *6* (12), 8048–8057.

(155) Allara, D.; Stapleton, J. *Chapter 3*, *Springer Series in Surface Science* **2013**.

(156) Zhang, Z.; Hou, S.; Zhu, Z.; Liu, Z. Preparation and Characterization of a Porphyrin Self-Assembled Monolayer with a Controlled Orientation on Gold. *Langmuir* **2000**, *16* (2), 537−540.

(157) Şen, P.; Hirel, C.; Andraud, C.; Aronica, C.; Bretonnière, Y.; Mohammed, A.; Ågren, H.; Minaev, B.; Minaeva, V.; Baryshnikov, G.; Lee, H.-H.; Duboisset, J.; Lindgren, M. Fluorescence and FTIR Spectra Analysis of Trans-A_2B_2-Substituted Di- and Tetra-Phenyl Porphyrins. *Materials* **2010**, *3* (8), 4446−4475.

(158) Li, X.-Y.; Czernuszewicz, R. S.; Kincaid, J. R.; Spiro, T. G. Consistent Porphyrin Force Field. 3. Out-of-plane Modes in the Resonance Raman Spectra of Planar and Ruffled Nickel Octaethylporphyrin. *J. Am. Chem. Soc.* **1989**, *111* (18), 7012–7023.

(159) Nazeeruddin, M. K.; Humphry-Baker, R.; Officer, D. L.; Campbell, W. M.; Burrell, A. K.; Grätzel, M. Application of Metalloporphyrins in Nanocrystalline Dye-Sensitized Solar Cells for Conversion of Sunlight into Electricity. *Langmuir* **2004**, *20* (15), 6514–6517.

(160) Zhang, Y.-H.; Chen, D.-M.; He, T.; Liu, F.-C. Raman and Infrared Spectral Study of *meso*-Sulfonatophenyl Substituted Porphyrins ($TPPS_n$, n=1, 2A, 2O, 3, 4). *Spectrochimica Acta Part A* **2003**, *59* (1), 87–101.

(161) Thomas, D. W.; Martell, A. E. Metal Chelates of Tetraphenylporphine and Some p-Substituted Derivatives[1,2]. *J. Am. Chem. Soc.* **1959**, *81* (19), 5111–5119.

(162) Rush III, T. S.; Kozlowski, P. M.; Piffat, C. A.; Kumble, R.; Zgierski, M.; Spiro, T. G. Computational Modeling of Metalloporphyrin Structure and Vibrational Spectra: Porphyrin Ruffling in NiTPP. *J. Phys. Chem. B* **2000**, *104* (20), 5020–5034.

(163) Narasimham, N. A.; Nielsen, J. R.; Theimer, R. Vibrational Spectra of Fluorinated Aromatics. XIII. Benzotrifluoride. *J. Chem. Phys.* **1957**, *27*, 740−745.

(164) Panov, V. P.; Kazarin, L. A.; Dubrovin, V. I.; Gusev, V. V.; Kirsh, Y. E. Infrared Spectra of Atactic Poly(4-vinylpyridine). *Zh. Prikl. Spektrosk* **1974**, *21*, 862−869.

(165) Bar-Ilan, A.; Manassen, J. Heterogeneous and homogeneous catalysis by substituted cobalt tetraphenylporphyrins, and correlations with IR spectra. *Journal of Catalysis* **1974**, *33* (1), 68−73.

(166) Borod'Ko, Y. G.; Vetchinkin, S. I.; Zimont, S. L.; Ivleva, I. N.; Shul'Ga, Y. M. Nature of Satellites in X-ray Photoelectron Spectra XPS of Paramagnetic Cobalt (II) Compounds. *Chem. Phys. Lett.* **1976**, *42* (2), 264−267.

(167) Chuang, T. J.; Brundle, C. R.; Rice, D. W. Interpretation of the X-Ray Photoemission Spectra of Cobalt Oxides and Cobalt Oxide Surfaces. *Surf. Sci.* **1976**, *59* (2), 413–429.

(168) Dillard, J. G.; Schenck, C. V.; Koppelman., M. H. Surface Chemistry of Cobalt in Calcined Cobalt-Kaolinite Materials.". *Clays Clay Miner.* **1983**, *31* (1), 69–72.

(169) Costentin, C.; Savéant, J. M. Multielectron, Multistep Molecular Catalysis of Electrochemical Reactions: Benchmarking of Homogeneous Catalysts. *ChemElectroChem*. **2014**, *1* (7), 1226−1236.

(170) Rountree, E. S.; McCarthy, B. D.; Eisenhart, T. T. Dempsey, J. L. Evaluation of Homogeneous Electrocatalysts by Cyclic Voltammetry. *Inorg. Chem.* **2014**, *53* (19), 9983−10002.

(171) Lee, K. J.; Elgrishi, N.; Kandemir, B.; Dempsey, J. L. Electrochemical and Spectroscopic Methods for Evaluating Molecular Electrocatalysts. *Nat. Rev. Chem.* **2017**, *1*, 0039

(172) Roberts, E. M.; Koski, W. S. An Electron Spin Resonance Study of Copper Etioporphyrin II. *J. Am. Chem. Soc.* **1960**, *82* (12), 3006−3010.

(173) Blumberg, W. E.; Peisach, J. An Electron Spin Resonance Study of Copper Uroporphyrin III and Other Touraco Feather components. *J. Biol. Chem*. **1965**, *240* (2), 870−876.

(174) Assour, J. M. Electron Spin Resonance of Tetraphenylporphine Chelates. *J. Chem. Phys.* **1965**, *43* (7), 2477−2489.

(175) Gurd, F. R. N.; Falk, K. E.; Malmström, B. G.; Vänngård, T. A Magnetic Resonance Study of Sperm Whale Ferrimyoglobin and its Complex with 1 Cupric Ion. *J. Biol. Chem*. **1967**, *242* (24), 5724−5730.

(176) Bemski, G.; Arends, T.; Blanc, G. Electron Spin Resonance of Cu (II) in Copper-Hemoglobin Complexes. *Biochem. Biophys. Res. Commun*. **1969**, *35* (5), 599−605.

(177) Hsu, Y. EPR Studies of Three Cupric Complexes with Nitrogenous Ligands. *Molec. Phys.* **1971**, *21* (6), 1087−1103.

(178) Clark, C. O.; Poole, J. C. P.; Farach, H. A. An Electron Spin Resonance Study of Copper (II) Tetraphenyl Porphyrins. *J. Phys. C: Solid State Phys*. **1978**, *11* (4), 769−774.

(179) Solomon, E. I.; Heppner, D. E.; Johnston, E. M.; Ginsbach, J. W.; Cirera, J.; Qayyum, M.; Kieber-Emmons, M. T.; Kjaergaard, C. H.; Hadt, R. G.; Tian, L. Copper Active Sites in Biology. *Chem. Rev*. **2014**, *114* (7), 3659−3853.

(180) Peisach, J.; Blumberg, W. E. Structural Implications Derived from the Analysis of Electron Paramagnetic Resonance Spectra of Natural and Artificial Copper Proteins. *Arch. Biochem. Biophys.* **1974**, *165* (2), 691−708.

(181) Toyama, N.; Asano-Someda, M.; Kaizu, Y. EPR Spectra of Gable-type Copper (II) Porphyrin Dimers in Fluid Solution: Extraction of Exchange Interaction in Weakly Coupled Doublet Pairs. *Mol. Phys*. **2003**, *101* (6), 733−742.

(182) Wang, R.; Brugh, A. M.; Rawson, J.; Therien, M. J.; Forbes, M. D. E. Alkyne-Bridged Multi [Copper (II) Porphyrin] Structures: Nuances of Orbital Symmetry in Long-Range, Through-Bond Mediated, Isotropic Spin Exchange Interactions. *J. Am. Chem. Soc*. **2017**, *139* (29), 9759−9762.

(183) Tsuda, A.; Osuka, A. Discrete Conjugated Porphyrin Tapes with an Exceptionally Small Bandgap. *Adv. Mater.* **2002**, *14* (1), 75−79.

(184) Cho, H. S.; Jeong, D. H.; Cho, S.; Kim, D.; Matsuzaki, Y.; Tanaka, K.; Tsuda, A.; Osuka, A. Photophysical Properties of Porphyrin Tapes. *J. Am. Chem. Soc.* **2002**, *124* (49), 14642−14654.

(185) Ouyang, Q.; Zhu, Y-Z.; Zhang, C-H.; Yan, K-Q.; Li, Y-C.; Zheng, J-Y. An Efficient PIFA-Mediated Synthesis of Fused Diporphyrin and Triply-Singly Interlacedly Linked Porphyrin Array. *Org. Lett.* **2009**, *22* (11), 5266−5269.

(186) Bonifazi, D.; Accorsi, G.; Armaroli, N.; Song, F.; Palkar, A.; Echegoyen, L.; Scholl, M.; Seiler, P.; Jaun, B.; Diederich, F. Oligoporphyrin Arrays Conjugated to [60]Fullerene: Preparation, NMR Analysis, and Photophysical and Electrochemical Properties. *Helvetica Chimica Acta*, **2005**, *88* (7), 1839−1884.

(187) Fendt, L-A.; Fang, H.; Plonska-Brzezinska, M. E.; Zhang, S.; Cheng, F.; Braun, C.; Echegoyen, L.; Diederich, F. *meso*, *meso*-Linked and Triply Fused Diporphyrins with Mixed-Metal Ions: Synthesis and Electrochemical Investigations. *Eur. J. Org. Chem.* **2007**, *2007* (28), 4659−4673.

(188) Wu, Y.; Jiang, J.; Weng, Z.; Wang, M.; Broere, D. L.; Zhong, Y.; Brudvig, G. W.; Feng, Z.; Wang, H. Electroreduction of CO_2 Catalyzed by a Heterogenized Zn–Porphyrin Complex with a Redox-Innocent Metal Center. *ACS Cent. Sci.* **2017**, *3* (8), 847−852.

(189) Azcarate, I.; Costentin, C.; Robert, M.; Savéant, J. M. Through-Space Charge Interaction Substituent Effects in Molecular Catalysis Leading to the Design of the Most Efficient Catalyst of CO_2-to-CO Electrochemical Conversion. *J. Am. Chem. Soc.* **2016**, *138* (51), 16639−16644.

(190) Lee, C. H.; Dogutan, D. K.; Nocera, D. G. Hydrogen Generation by Hangman Metalloporphyrins. *J. Am. Chem. Soc.* **2011**, *133* (23), 8775−8777.

(191) Khusnutdinova, D.; Beiler, A. M.; Wadsworth, B. L.; Nanyangwe, S. K.; Moore, G. F. Vibrational Structure Analysis of Cobalt Fluoro-Porphyrin Surface Coatings on Gallium Phosphide. *J. Porphyrins Phthalocyanines* **2018**, *22* (6), 461−466.

(192) Roberts, J. A.; Bullock, R. M. Direct Determination of Equilibrium Potentials for Hydrogen Oxidation/Production by Open Circuit Potential Measurements in Acetonitrile. *Inorg. Chem.* **2013**, *52* (7), 3823−3835.

(193) Crabtree, R. H. Resolving Heterogeneity Problems and Impurity Artifacts in Operationally Homogeneous Transition Metal Catalysts. *Chem. Rev.* **2011**, *112* (3), 1536−1554.

(194) Artero, V.; Fontecave, M. Solar Fuels Generation and Molecular Systems: is it Homogeneous or Heterogeneous Catalysis? *Chem. Soc. Rev.* **2013**, *42* (6), 2338−2356.

(195) Widegren, J. A.; Finke, R. G. A Review of the Problem of Distinguishing True Homogeneous Catalysis from Soluble or Other Metal-Particle Heterogeneous Catalysis Under Reducing Conditions. *J. Mol. Catal. A: Chem.* **2003**, *198* (1-2), 317−341.

(196) Chen, J. G.; Jones, C. W.; Linic, S; Stamenkovic, V. R. Best Practices in Pursuit of Topics in Heterogeneous Electrocatalysis. *ACS Catal.* **2017**, *7* (9), 6392−6393.

(197) Costentin, C.; Dridi, H.; Savéant, J. M. Molecular Catalysis of H_2 Evolution: Diagnosing Heterolytic versus Homolytic Pathways. *J. Am. Chem. Soc.* **2014**, *136* (39), 13727−13734.

(198) McCrory, C. C.; Jung, S.; Peters, J. C.; Jaramillo, T. F. Benchmarking Heterogeneous Electrocatalysts for the Oxygen Evolution Reaction. *J. Am. Chem. Soc.* **2013**, *135* (45), 16977−16987.

(199) Lee, C. H; Lindsey, J. S. One-Flask Synthesis of Meso-Substituted Dipyrromethanes Their Application in the Synthesis of Trans-Substituted Porphyrin Building Blocks. *Tetrahedron* **1994**, *50* (39), 11427–11440.

(200) Gao, G. Y.; Ruppel, J. V.; Allen, D. B.; Chen, Y.; Zhang, X. P. Synthesis of β-Functionalized Porphyrins via Palladium- Catalyzed Carbon - Heteroatom Bond Formations : Expedient Entry into β -Chiral Porphyrins. *JOC Artic*. **2007**, *7 2*(6), 906–9066.

(201) Chizhova, N. V.; Kumeev, R. S.; Mamardashvili, N. Zh. Synthesis and Spectral Properties of Cobalt (II) and Cobalt (III) Tetraarylporphyrinates. *Russ. J. Inorg. Chem*. **2013**, *58* (6), 740–743.

(202) Gobi, K. V.; Tokuda, K.; Ohsaka, T. Electrochemical and Spectroscopic Studies on Nickel(II/III) Complexes with Novel 14-membered Hexaaza Macrocycle Functionalized with Propenyl Groups. *Electrochim. Acta* **1998***, 43* (9), 1013–1022.

(203) Flores, M.; Isaacson, R.; Abresch, E.; Calvo, R.; Lubitz, W.; Feher, G. Protein-Cofactor Interactions in Bacterial Reaction Centers from *Rhodobacter sphaeroides* R-26: II. Geometry of the Hydrogen Bonds to the Primary Quinone Q_A^- by ^1H and ^2H ENDOR Spectroscopy. *Biophys. J.* **2007**, *92* (2), 671–682.

(204) Hariprasad, G.; Dahal, S.; Maiya, B. G. *Meso*-Substituted Octabromoporphyrins: Synthesis, Spectroscopy, Electrochemistry and Electronic Structure. *J. Chem. Soc., Dalton Trans.* **1996**, *16*, 3429–3436.

(205) Gervaldo, M.; Fungo, F.; Durantini, E. N.; Silber, J. J.; Sereno, L.; Otero, L. Carboxyphenyl Metalloporphyrins as Photosensitizers of Semiconductor Film Electrodes. A Study of the Effect of Different Central Metals. *J. Phys. Chem. B* **2005**, *109* (44), 20953–20962.

(206) Ye, L.; Ou, Z.; Fang, Y.; Xue, S.; Song, Y.; Wang, L.; Wang, M; Kadish, K. M. Electrochemistry of Nonplanar Copper(II) Tetrabutano- and Tetrabenzotetraarylporphyrins in Nonaqueous Media. *RSC Adv.* **2015**, *5* (94), 77088–77096.

(207) Weil, J. A.; Bolton, J. R. Electron Paramagnetic Resonance: Elementary Theory and Practical Applications. *John Wiley & Sons*. **2007**.

(208) Stoll, S.; Schweiger, A. J. EasySpin, a Comprehensive Software Package for Spectral Simulation and Analysis in EPR. *Magn. Reson*. **2006**, *178* (1), 42–55.

APPENDIX A

ACKNOWLEDGEMENTS FOR PERMISSION

Khusnutdinova, D.; Wadsworth, B. L.; Flores, M.; Beiler, A. M.; Reyes, E. A.; Zenkov, Y.; Moore, G. F. *ACS Catal.* **2018**, *8* (10), 9888–9898.

Khusnutdinova, D.; Beiler, A. M.; Wadsworth, B. L.; Nanyangwe, S. K.; Moore, G. F. *J. Porphyr. Phthalocyanines* **2018**, *22* (6), 461–466.

Khusnutdinova, D.; Flores, M.; Beiler, A. M.; Moore, G. F. *Photosynthetica* **2018**, *56* (1), 67–74.

Khusnutdinova, D.; Beiler, A. M.; Wadsworth B. L.; Jacob S. I.; Moore G. F. *Chem. Sci.* **2017**, *8* (1), 253–259.